

MICROLOCAL ANALYSIS AND APPLICATIONS TO MEDICAL IMAGING

A Dissertation

Submitted to the Faculty

of

Purdue University

by

Chase O. Mathison

In Partial Fulfillment of the

Requirements for the Degree

of

Doctor of Philosophy

August 2020

Purdue University

West Lafayette, Indiana

THE PURDUE UNIVERSITY GRADUATE SCHOOL
STATEMENT OF DISSERTATION APPROVAL

Dr. Plamen Stefanov, Chair
Department of Mathematics

Dr. Antônio Sà Barreto
Department of Mathematics

Dr. Kiril Datchev
Department of Mathematics

Dr. Isaac Harris
Department of Mathematics

Approved by:

Dr. Plamen Stefanov
Head of the School Graduate Program

To Emily.

ACKNOWLEDGMENTS

First and foremost, I am deeply grateful to my advisor Plamen Stefanov for his patient guidance through my time at Purdue. I would not have made it through graduate school if it weren't for his help and understanding.

I'd also like to thank my family, in particular my parents, for their support in my life and especially in the last several years.

I'd like to thank my church family for their support as well.

Lastly, I am forever indebted to my wonderful wife Emily. Without your help at home, I would not be where I am today.

TABLE OF CONTENTS

	Page
LIST OF FIGURES	vii
ABSTRACT	xi
1 INTRODUCTION	1
1.1 An Overview of Microlocal Analysis	1
1.1.1 The Fourier Transform	1
1.1.2 Solving a PDE	2
1.1.3 Finding a Parametrix	3
1.1.4 The calculus of pseudodifferential operators	5
1.1.5 Transposition, Composition of Ψ DOs	8
1.1.6 The wave front set of a distribution	10
1.1.7 Geometrical optics	11
1.1.8 Local theory of Fourier integral operators (FIOs)	12
1.1.9 The canonical relation associated with an FIO	13
1.1.10 The effect of FIOs on wave front sets	13
2 THERMOACOUSTIC TOMOGRAPHY WITH CIRCULAR INTEGRATING DETECTORS AND VARIABLE WAVE SPEED	14
2.1 Setup	15
2.2 Construction	17
2.2.1 Case 1: Small Radius	21
2.2.2 Case 2: Large Radius	25
2.3 Injectivity	26
2.3.1 Case 1: Small Radius	26
2.3.2 Case 2: Large Radius	29
2.4 Stability	34
2.4.1 Visible Singularities	35
2.5 Numerical Results	37
2.6 Conclusion and Future Work	39
3 SAMPLING IN THERMOACOUSTIC TOMOGRAPHY	41
3.1 Introduction	41
3.1.1 M as an FIO	42
3.2 Preliminary definitions and theorems	43
3.2.1 Semiclassical analysis	43
3.2.2 Sampling	46
3.3 Resolution limit of f given sampling rate of Mf	47

	Page
3.3.1	The effect of s_t on resolution 48
3.3.2	The effect of s_{y^j} on resolution 50
3.3.3	CFL condition 53
3.4	Aliasing and artifacts 54
3.4.1	Under sampling in t 55
3.4.2	Under sampling in y 56
3.5	Averaged data 59
3.6	Anti-aliasing 62
4	NON-UNIQUENESS IN THE REGION OF INTEREST PROBLEM FOR THE RADON TRANSFORM 66
4.1	Introduction 66
4.2	Background and definitions 67
4.2.1	Special functions 67
4.2.2	The Radon transform 70
4.3	Main Results 73
4.3.1	Application: Non-uniqueness in the interior problem 76
4.4	Conclusion and future work 82
	REFERENCES 86
	VITA 89

LIST OF FIGURES

Figure	Page
2.1 Two different experimental setups shown depending on the radius of the integrating detector. On the left is the small radius case, and on the right is the large radius case.	23
2.2 Singularities that may be visible from $\theta_0 \in \Gamma$ in both the cases (left) $R - r > 1$ and (right) $R = 1, r > 2$ will lie on the geodesics issued from the integrating detectors.	36
2.3 Variable wave speed of $1 + 0.3 \sin(8x) \cos(5y) \eta(x, y)$, where $\eta(x, y) \in C_0^\infty(B_1(0))$.	38
2.4 Results of reconstruction using $R = 1$ and $r = 2$ model (Large radius detector model). This reconstruction was made using full data.	38
2.5 Result of reconstruction with partial data using $R = 2$, and $r = 0.8$ (Small radius detector model). This reconstruction was for $\theta \in (-\pi/2, 0)$. Shown in the figure are the set on which data is collected as well as some representative circular integrating detectors.	39
2.6 Result of reconstruction with partial data using $R = 1$, and $r = 2$ (Large radius detector model). This reconstruction was for $\theta \in (-\pi/2, 0)$. Shown in the figure are the set on which data is collected as well as some representative circular integrating detectors.	39
3.1 Resolution of f given a fixed sampling rate s_t of $Mf(t, y)$. The wave speed here $c(x, y) = 1 + 0.5 \exp(-((x + 1)^2 + y^2)^2/0.25)$ has a fast spot centered at $x = -1$. We can see that this is precisely where the reconstruction of f has poor resolution when under sampled in the t variable, as explained above. Undersampling is simulated by taking every 7 th time sample, and then resizing the image of the data to its original size.	51
3.2 Resolution of f given a fixed sampling rate s_t of $Mf(t, y)$. The wave speed here $c(x, y) = 1 - 0.5 \exp(-((x + 1)^2 + y^2)^2/0.25)$ has a slow spot centered at $x = -1$. We can see that this is precisely where the reconstruction of f has the best resolution when under sampled in the t variable, as explained above. Undersampling is simulated by taking every 7 th time sample.	52

Figure	Page
3.3 Resolution of f given a fixed sampling rate s_{y^j} of the space variables on the boundary $\partial\Omega$. We can see that the blurring effect is roughly uniform for points near the fast spot in the wave speed $c(x, y) = 1 + 0.5 \exp(-((x - 1)^2 + (y + 0.5)^2)/0.25)$, but that there are singularities in the region where $c \approx 1$ far from the fast spot that are also highly affected. These singularities hit the boundary with a larger angle to the outward pointing normal vector, and so we expect lower resolution there. Undersampling is simulated by taking every 12 th space sample.	54
3.4 The characteristic cone in which $\Sigma_h(Mf)$ must lie. The cone on the left shows the possible range of the covector (η, τ) which is determined by the canonical relation associated with M . The image on the right shows the possible range of covectors (η, τ) after under sampling (in t). Note that the red regions have been shifted up and down from the original frequency set by translation due to under sampling.	55
3.5 Tracing the aliasing artifacts by using geodesics. We have used the constant wave speed $c \equiv 1$ for this example. Here we have under sampled in t and show the image of the singularity (x, ξ) under the canonical relations given by $C_{\pm}^{-1} \circ S_1 \circ C_{\pm}$. Note that the low frequency singularity does not cause artifact, but the high frequency singularity vanishes in the reconstruction and causes aliasing artifacts. Undersampling is simulated by taking every 12 th time sample.	57
3.6 Artifacts in a reconstructed image with Mf under sampled in time variable and a variable wave speed of $c(x, y) = 1 - 0.5 \exp(-\frac{((x+1)^2+y^2)^2}{0.25})$. We trace the geodesics to find the image of (x, ξ) under the map $C_{\pm} \circ S_k \circ C_{\pm}$ as explained above. Undersampling is simulated by taking every 12 th time sample.	58
3.7 Artifacts in a reconstructed image with Mf under sampled in space variables. Here we take $c \equiv 1$. Specifically, Mf here was under sampled on the left and right edges of the square. We simulate undersampling by taking every 15 th space sample. Note that there is no artifact in the reconstructed image coming from the pattern in the upper right corner of the square, because singularities from this pattern hit the boundary of the square perpendicularly. Note also that the original singularity still remains with half its amplitude because we did not under sample along the bottom edge of the square.	59

Figure	Page	
3.8	Artifacts in a reconstructed image with Mf under sampled in space variables and a variable wave speed of $c(x, y) = 1 - 0.5 \exp(-\frac{((x+1)^2+y^2)^2}{0.25})$. Specifically, Mf here was under sampled on the top and bottom edges of the square. The artifacts in the reconstruction have the same frequency as the original, but with a space shift due to under sampling. We simulate heavy undersampling by taking only every 30 th space sample.	60
3.9	Reconstructed image from data that has been averaged in time variable by applying a 1D gaussian image filter to the t data. We can see that the reconstructed image is most blurred at the points where the speed $c(x)$ is fast, and there is less blurring where $c(x) = 1$	61
3.10	Reconstructed image from data that has been averaged in space variable by applying a 1D gaussian image filter to the y data. We can see from the drawn in geodesics, that singularities that hit the boundary at a larger angle to the normal vector to the boundary are blurred more in the reconstructed image after averaging the collected data. Meanwhile, those singularities that hit the boundary nearly perpendicularly are largely unaffected by the averaging of the data, at least on one side.	62
3.11	Example showing anti-aliasing scheme in which we first average the data $Mf(t, y)$ in the y variable and then sample this blurred version given by $Q_h Mf(t, y)$ in the above notation. We can see that some of the aliasing artifacts have been removed at the cost of some loss of resolution.	63
3.12	Image of a zebra along with reconstruction from under sampled (in t) data. The wave speed here is constant. High frequencies are lost due to this under sampling and the result is a heavily blurred image with aliasing artifacts.	64
3.13	Collected data and under sampled data in t along with the associated Fourier transform data for the zebra image above. Note that the high frequencies in $\mathcal{F}(Mf)$ have be shifted so that they are approximately in the band $-\pi/s_t < \tau < \pi/s_t$, which is what results in the blurring in the reconstruction.	64
3.14	Image of a zebra along with reconstruction from under sampled (in y) data. The wave speed here is constant. Note that the singularities that hit the boundary of the square nearly perpendicularly are preserved, but there are also a lot of high frequency artifacts in the reconstructed image.	65

Figure	Page
3.15 Collected data and under sampled data in y along with the associated Fourier transform data for the zebra image above. Under sampling has resulted in the shifting of frequencies in $\mathcal{F}(Mf)$ so that $-\pi/s_{y^j} < \eta < \pi/s_{y^j}$. This moves high frequencies but does not destroy them, which is what causes the high frequency artifacts in the reconstructed image above.	65
4.1 (Top left) Function $g(\omega, p) = \sum_{l=0}^{10} a_l g_l(p) e^{il\omega}$ constructed so that $g = Rf$ for some $f \in \mathcal{S}(\mathbb{R}^2)$. This function was constructed so that $\mu_m g_k = 0$ for $0 \leq m < k$ in the Fourier series expansion of g , as is required by Theorem 4.3.1. (Top right) Inverse Radon transform of g . (Bottom left) $R^{-1}(g)$ for $ (x, y) < 0.3$. Note that $R^{-1}(g)(x, y)$ is not identically 0 here. (Bottom right) $R \circ R^{-1}(g)$, which we can see is the same as in the top left.	83
4.2 Error in $R \circ R^{-1}g$ for the function shown in Figure 4.1	84
4.3 Simple examples of non-uniqueness for the region of interest problem. Both f_0 and f_1 are nonzero in the region of interest $ (x, y) < 0.3$, but Rf_0 and Rf_1 are zero for $ p < 0.3$	85

ABSTRACT

Mathison, Chase O. Ph.D., Purdue University, August 2020. Microlocal Analysis and Applications to Medical Imaging. Major Professor: Plamen Stefanov.

This thesis is a collection of the three projects I have worked on at Purdue. The first is a paper on thermoacoustic tomography involving circular integrating detectors that was published in *Inverse Problems and Imaging* [21]. Results from this paper include demonstrating that the measurement operators involved are Fourier integral operators, as well as proving microlocal uniqueness in certain cases, and also stability. The second paper, submitted to the *Journal of Inverse and Ill-Posed Problems*, is much more of an application of sampling theory in [27] to the specific case of thermoacoustic tomography. Results from this paper include demonstrating resolution limits imposed by sampling rates, and showing that aliasing artifacts appear in predictable locations in an image when the measurement operator is under sampled in either the time variable or space variables. We also show an application of a basic anti aliasing scheme based on averaging of data. The last project moves slightly away from microlocal analysis and considers the uniqueness in medical imaging of the restricted Radon transform in even dimensions. This is the classical interior problem, and we show a characterization of the range of the Radon transform, and from this are able to obtain a characterization of the kernel of the restricted Radon transform. We include figures throughout to illustrate results.

1. Introduction

1.1 An Overview of Microlocal Analysis

Classical analysis, or local analysis, is the study of functions defined in a neighborhood of a point $x \in \mathbb{R}^n$. The usual tools of classical analysis are in general ineffective when studying singularities of a function. Microlocal analysis attempts to extend the ideas of classical analysis to gain more information about a function in the phase space. This is accomplished by first looking at the Fourier transform of a function, and the properties of this transform. In this way, we can learn about singularities of a function near a point (the "local" of microlocal analysis) and near a certain direction (the "micro" of microlocal analysis). We present some of the basic ideas of microlocal analysis which largely follows Chapter I of [34].

1.1.1 The Fourier Transform

The Fourier transform is defined for functions in $L^1(\mathbb{R}^n)$ as follows

$$\mathcal{F}(f(\cdot))(\xi) := \int_{\mathbb{R}^n} e^{-ix \cdot \xi} f(x) dx. \quad (1.1)$$

The inverse Fourier transform is defined in a similar way for functions in $L^1(\mathbb{R}^n)$

$$\mathcal{F}^{-1}(g(\cdot))(x) := \frac{1}{(2\pi)^n} \int_{\mathbb{R}^n} e^{ix \cdot \xi} g(\xi) d\xi. \quad (1.2)$$

If a function has more regularity than simply being in the class $L^1(\mathbb{R}^n)$, then this will manifest in decay at infinity of Fourier transform of the function. The converse is also true, and is the basis for microlocalization and studying functions and their singularities in the phase space. As an example of a function with certain smoothness

exhibiting decay in its Fourier transform, if $f \in L^1(\mathbb{R}) \cap C^1(\mathbb{R})$ and $f' \in L^1(\mathbb{R})$ then we have (formally, using integration by parts)

$$\begin{aligned}\mathcal{F}(f)(\xi) &= \int_{\mathbb{R}} e^{-ix\xi} f(x) dx \\ &= -\frac{-1}{i\xi} \int_{\mathbb{R}} e^{-ix\xi} f'(x) dx,\end{aligned}$$

from which we see that $|\mathcal{F}(f)(\xi)| = O(|\xi|^{-1})$. For convenience, we will denote $\hat{f}(\xi) := \mathcal{F}(f)(\xi)$. Continuing this process, we can see that if $f \in L^1(\mathbb{R}) \cap C^k(\mathbb{R})$ and $f^{(j)} \in L^1(\mathbb{R})$ for each $0 \leq j \leq k$, then

$$|\mathcal{F}(f)(\xi)| = O(|\xi|^{-k}),$$

where we've used the traditional "Big- O " notation which has the following meaning: $f(x) = O(g(x))$ means $\exists r > 0$ and $M > 0$ such that for $x > r$, we have $|f(x)| \leq M|g(x)|$.

1.1.2 Solving a PDE

Microlocal analysis extends the usual ideas of classical analysis to the phase space, or more generally, to the cotangent bundle of a smooth manifold. We begin with a simple motivating example. Suppose we wish to solve the PDE in \mathbb{R}^n :

$$(1 - \Delta)u = f.$$

Here $\Delta u = \sum_{i=1}^n \partial_{x_i}^2 u$. One method that might first come to mind is to try to solve this PDE using the Fourier transform as so:

$$(1 - \Delta)u = f \implies (1 + |\xi|^2)\hat{u} = \hat{f},$$

and from this we see that because $1 + |\xi|^2 \neq 0$ for any $\xi \in \mathbb{R}^n$, we may take as a solution for u

$$u(x) = \frac{1}{(2\pi)^n} \int_{\mathbb{R}^n} e^{ix \cdot \xi} \frac{\hat{f}(\xi)}{1 + |\xi|^2} d\xi.$$

This was obtained by applying the inverse Fourier transform to \hat{u} . In doing this, we have implicitly assumed that u and f are members of the space of tempered distributions $\mathcal{S}'(\mathbb{R}^n)$, which is the dual space to the Schwartz class of functions $\mathcal{S}(\mathbb{R}^n)$ which is defined as

$$\mathcal{S}(\mathbb{R}^n) = \{g \in C^\infty(\mathbb{R}^n) \mid \sup_x |x^\alpha \partial^\beta g(x)| < \infty \text{ for all multi indices } \alpha \text{ and } \beta\} \quad (1.3)$$

1.1.3 Finding a Parametrix

In the previous example, we divided by a quantity that was always positive. If we change the PDE slightly, then we'll run into trouble when we try to solve it using the Fourier transform. Let's examine solutions to the PDE, this time in \mathbb{R}^2

$$-\Delta u = f$$

where again we will assume that u and f are in $\mathcal{S}(\mathbb{R}^2)$. Using the same method as before, we arrive at the following "solution" for u ,

$$u(x) = \frac{1}{(2\pi)^2} \int_{\mathbb{R}^2} e^{ix \cdot \xi} \frac{\hat{f}(\xi)}{|\xi|^2} d\xi.$$

But here we have an issue: $1/|\xi|^2$ is not integrable at the origin in \mathbb{R}^2 . To remedy this, we'll find a solution that's accurate up to a smooth error. Let $\chi(\xi)$ be a smooth function with support contained in a small ball centered at the origin $B_\delta(0)$ of radius $\delta > 0$. Further, suppose $\chi \equiv 1$ for $|\xi| < \delta/2$. Then, because $\hat{f} = \chi \hat{f} + (1 - \chi) \hat{f}$, if we set

$$v(x) = \frac{1}{(2\pi)^2} \int_{\mathbb{R}^2} e^{ix \cdot \xi} \frac{(1 - \chi(\xi)) \hat{f}(\xi)}{|\xi|^2} d\xi,$$

then we can show that v solves not the PDE in question, but the PDE $-\Delta v = f - R(x)$, where R is a smooth function. To see this, note that

$$\partial_{x_i} v(x) = \frac{1}{(2\pi)^2} \int_{\mathbb{R}^2} i\xi_i e^{ix \cdot \xi} \frac{(1 - \chi(\xi)) \hat{f}(\xi)}{|\xi|^2} d\xi$$

and from this it is clear that

$$\partial_{x_i}^2 v(x) = -\frac{1}{(2\pi)^2} \int_{\mathbb{R}^2} \xi_i^2 e^{ix \cdot \xi} \frac{(1 - \chi(\xi)) \hat{f}(\xi)}{|\xi|^2} d\xi$$

which gives

$$\begin{aligned} -\Delta v(x) &= \frac{1}{(2\pi)^2} \int_{\mathbb{R}^2} |\xi|^2 e^{ix \cdot \xi} \frac{(1 - \chi(\xi)) \hat{f}(\xi)}{|\xi|^2} d\xi \\ &= \frac{1}{(2\pi)^2} \int_{\mathbb{R}^2} e^{ix \cdot \xi} (1 - \chi(\xi)) \hat{f}(\xi) d\xi \\ &= f - Rf(x) \end{aligned}$$

where $Rf(x) = \frac{1}{(2\pi)^2} \int_{\mathbb{R}^2} e^{ix \cdot \xi} \chi(\xi) \hat{f}(\xi) d\xi$. This is the inverse Fourier transform of a compactly supported function (so also, a function that decays at infinity faster than any polynomial in ξ), which means that $Rf(x) \in C^\infty(\mathbb{R}^2)$. But why do we care that $v(x)$ solves the PDE $-\Delta v = f - Rf(x)$ when we were interested in the PDE $-\Delta u = f$? If $-\Delta v = f + Rf$ and Rf is smooth, then we know that f and $f + Rf$ have the same singularities, for Rf cannot contribute to singularities of $f + Rf$, as $Rf \in C^\infty(\mathbb{R}^2)$. This makes this calculus very useful in situations such as medical imaging, where we might not care about an exact reconstruction of the interior of a patient, but we do care about the ‘‘singularities’’, which might represent the presence of a tumor, or the interface between tissues of different types.

Note that if we define the operator

$$Kf = \frac{1}{(2\pi)^2} \int_{\mathbb{R}^2} e^{ix \cdot \xi} \frac{(1 - \chi(\xi)) \hat{f}(\xi)}{|\xi|^2} d\xi$$

then what we calculated above shows that $-\Delta(Kf) = (I + R)f$, where R is a smoothing operator. In other words $-\Delta \circ K = I + R$, which is what we will take as the definition of a right parametrix for the operator $-\Delta$, and in general, for any operator P , we define a right parametrix K as an operator such that $P \circ K = I + R$ where R is a smoothing operator. We may define a left parametrix in a similar way.

We can generalize the above method to find a parametrix for a linear partial differential operator

$$P(x, D) = \sum_{|\alpha| \leq m} a_\alpha(x) D^\alpha,$$

where $a_\alpha \in C^\infty(\mathbb{R}^n)$, provided the principal symbol

$$P_m(x, \xi) = \sum_{|\alpha|=m} a_\alpha(x) \xi^\alpha,$$

satisfies the condition

$$P_m(x, \xi) \neq 0 \text{ if } \xi \neq 0.$$

A linear partial differential operator that satisfies this condition is called elliptic.

1.1.4 The calculus of pseudodifferential operators

The symbol class $S_{1,0}^m(\Omega, \mathbb{R}^N)$

In the above discussion, we were able to “invert” up to a smooth error some operators of the form

$$Au(x) = \frac{1}{(2\pi)^n} \int_{\mathbb{R}^n} e^{ix \cdot \xi} a(x, \xi) \hat{u}(\xi) d\xi$$

where $X \subset \mathbb{R}^n$ and \cdot is the standard inner product on \mathbb{R}^n . The symbol $a(x, \xi)$ in the above problems has some key defining features that we will mention now so that we may deal with operators of the above form in a less ad hoc way.

Definition 1.1.1 (Symbol of order m) *Let $\Omega \subset \mathbb{R}^n$. A smooth function $a \in C^\infty(\Omega \times \mathbb{R}^n)$ will be called a symbol of order $m \in \mathbb{R}$ if given a compact set $K \subset \Omega$ and multiindexes α and β , there exists $C_{\alpha,\beta,K} > 0$ such that*

$$|\partial_x^\alpha \partial_\xi^\beta a(x, \xi)| \leq C_{\alpha,\beta,K} (1 + |\xi|)^{m-|\beta|}$$

for all $(x, \xi) \in K \times \mathbb{R}^n$. The space of symbols of order m will be denoted

$$S_{1,0}^m(\Omega, \mathbb{R}^n)$$

or when it's clear from context, simply

$$S^m(\Omega)$$

We note that there is a more general symbol class $S_{\rho,\delta}^m(\Omega, \mathbb{R}^n)$, with $0 < \rho \leq 1$ and $0 \leq \delta < 1$, but the standard symbol class defined above will be sufficient for our purposes. For later, we denote the spaces $S^{-\infty}(\Omega) = \bigcap_{m \in \mathbb{R}} S^m(\Omega)$ and $S(\Omega) = \bigcup_{m \in \mathbb{R}} S^m(\Omega)$.

Symbols are important because they allow us to define pseudodifferential operators (Ψ DOs for short)

Definition 1.1.2 (Pseudodifferential Operator of order m) Let $\Omega \subset \mathbb{R}^n$ be an open set and let $a(x, \xi) \in S_{1,0}^m(\Omega, \mathbb{R}^n)$. Let $u \in C_0^\infty(\Omega)$, then the operator $\text{Op}(a)$ defined by

$$\text{Op}(a)u = \frac{1}{(2\pi)^n} \int_{\mathbb{R}^n} e^{ix \cdot \xi} a(x, \xi) \hat{u}(\xi) d\xi \quad (1.4)$$

is called a (standard) pseudodifferential operator of order m on Ω . We denote the space of pseudodifferential operators of order m on Ω by $\Psi^m(\Omega)$.

A priori, because $a(x, \xi) \in C^\infty(\Omega \times \mathbb{R}^n)$, we know that $\text{Op}(a) : C_0^\infty(\Omega) \rightarrow C^\infty(\Omega)$. Using standard functional analysis arguments and the transpose operator, it can be shown that $\text{Op}(a)$ may be extended to a continuous linear operator $\text{Op}(a) : \mathcal{E}'(\Omega) \rightarrow \mathcal{D}'(\Omega)$. And in fact, it can be shown (see Theorem 2.1 in [34]) that if $a \in S^m(\Omega)$, then $\text{Op}(a) : H_c^s(\Omega) \rightarrow H^{s-m}(\Omega)$, for any real number s . We denote the spaces $\Psi^{-\infty}(\Omega) = \bigcap_{m \in \mathbb{R}} \Psi^m(\Omega)$ and $\Psi(\Omega) = \bigcup_{m \in \mathbb{R}} \Psi^m(\Omega)$. It is a fact that if $P \in \Psi^{-\infty}(\Omega)$ then $P : \mathcal{E}'(\Omega) \rightarrow C^\infty(\Omega)$, or in other words $\Psi^{-\infty}(\Omega)$ is the space of regularizing operators. In the microlocal calculus, we consider two Ψ DOs A and B equivalent if $A - B \in \Psi^\infty(\Omega)$.

One question one might ask about the definition of a Ψ DO is: is this even well defined? In other words, does the integral in question even converge? This is clear because by assuming $u \in C_0^\infty(\mathbb{R}^n)$, it is a fact [30] that given any $N \in \mathbb{N}$, we have

$$\lim_{|\xi| \rightarrow \infty} |\xi|^N |\hat{u}(\xi)| = 0.$$

So then, for any $N \in \mathbb{N}$, there is some $R_N > 0$ such that for $|\xi| > \max\{1, R_N\}$, we have $|\hat{u}(\xi)| \leq |\xi|^{-N} \leq \frac{C}{(1+|\xi|)^N}$, where $C \geq 2^N$. We also know $|a(x, \xi)| \leq (1 + |\xi|)^m$. So, taking N large enough so that $m - N < -(n+1)$, we see that the integral defining $\text{Op}(a)$ is absolutely convergent.

Very often we will work with so called classical symbols. These are symbols written as an asymptotic expansion

$$a(x, \xi) \sim \sum_{j=0}^{\infty} a_{m-j}(x, \xi),$$

where $a_{m-j}(x, \xi) \in C^\infty(\mathbb{R}^{2n})$ with $a_{m-j}(x, \xi)$ positively homogeneous of order $m - j$ in the ξ variable for $|\xi| > 1$. The sum is asymptotic in the sense that

$$a(x, \xi) - \sum_{j=0}^N a_{m-j}(x, \xi) \in S^{m-N-1}(\Omega),$$

for each $N \geq 0$.

A more general way to define Ψ DOs is to make use of the Fourier transform to write

$$\text{Op}(a)(u(\cdot))(x) = \frac{1}{(2\pi)^n} \int_{\mathbb{R}^n \times \Omega} e^{i(x-y)\cdot\xi} a(x, \xi) u(y) dy d\xi$$

where we either require that the integration be performed as noted, or the integral to be interpreted in the oscillatory sense. From this representation, it's clear that we could also allow a to depend on y as long as it satisfies a similar semi-norm estimate as above, i.e., given compact $K \subset \Omega \times \Omega$ and α, β, γ multiindexes, there exists $C(\alpha, \beta, \gamma, K) > 0$ such that

$$|\partial_x^\alpha \partial_y^\beta \partial_\xi^\gamma a(x, y, \xi)| \leq C(1 + |\xi|)^{m-|\gamma|},$$

for all $(x, y) \in K$ and $\xi \in \mathbb{R}^n$. We then call those $a(x, y, \xi) \in C^\infty(\Omega \times \Omega \times \mathbb{R}^n)$ satisfying these semi-norm estimates *amplitudes* of order m , but we will mostly only be interested in symbols, and use amplitudes only when their use simplifies proofs. By Theorem 4.1 in [34], there is no loss in using either symbols or amplitudes, as symbols are simply amplitudes independent of y , and given an amplitude $a(x, y, \xi)$, there exists a symbol $\tilde{a}(x, \xi)$ such that $\text{Op}(a) = \text{Op}(\tilde{a}) + R$ where R is a smoothing operator, which is considered negligible in the microlocal calculus.

Note that a differential operator is of the form

$$P(x, D) = \sum_{|\alpha| \leq m} a_\alpha(x) D^\alpha$$

and by virtue of the inverse Fourier transform, we may write (formally)

$$\begin{aligned} P(x, D)u(x) &= \sum_{|\alpha| \leq m} \frac{1}{(2\pi)^n} a_\alpha(x) D_x^\alpha \left(\int_{\mathbb{R}^n} e^{ix\cdot\xi} \hat{u}(\xi) d\xi \right) \\ &= \sum_{|\alpha| \leq m} \frac{1}{(2\pi)^n} \int_{\mathbb{R}^n} e^{ix\cdot\xi} a_\alpha(x) \xi^\alpha \hat{u}(\xi) d\xi. \end{aligned}$$

From this, it's clear (as long as $a_\alpha(x) \in C^\infty(\mathbb{R}^n)$) that $P(x, D)$ is a pseudodifferential operator of integer order $m \geq 0$, and so Ψ DOs are generalizations of (linear) differential operators. We also saw that the parametrix above for the operator $-\Delta$ is a Ψ DO of order -2 , and the fact that the order of this parametrix is negative indicates that it is not a partial differential operator.

1.1.5 Transposition, Composition of Ψ DOs

Given inner product spaces X, Y , and a linear operator $L : X \rightarrow Y$, the transpose $L^t : Y^* \rightarrow X^*$ is defined so that the following equation holds for all $u \in X, v \in Y^*$,

$$\langle Lu, v \rangle = \langle u, L^t v \rangle.$$

In particular, if $a \in S^m(\Omega, \Omega, \mathbb{R}^n)$ and $u, v \in C_0^\infty(\Omega)$, then

$$\begin{aligned} \langle \text{Op}(a)u, v \rangle &= \frac{1}{(2\pi)^n} \iiint_{\mathbb{R}^{3n}} e^{i(x-y)\cdot\xi} a(x, y, \xi) u(y) v(x) dx dy d\xi \\ &= \iiint_{\mathbb{R}^{3n}} e^{i(y-x)\cdot\xi} a(y, x, \xi) u(x) v(y) dy dx d\xi \\ &= \iiint_{\mathbb{R}^{3n}} e^{i(x-y)\cdot(-\xi)} a(y, x, \xi) v(y) u(x) dy dx d\xi \\ &= \iiint_{\mathbb{R}^{3n}} e^{i(x-y)\cdot\xi} a(y, x, -\xi) v(y) u(x) dy dx d\xi \\ &= \langle u, \text{Op}(a)^t v \rangle \end{aligned}$$

which shows that the transpose of a Ψ DO of order m is again a Ψ DO of order m . Its amplitude is clearly given by $b(x, y, \xi) = a(y, x, -\xi)$. In order to compose two Ψ DOs, we notice

$$\begin{aligned} A \circ Bu(x) &= \int_{\mathbb{R}^n} e^{i(x-y)\cdot\xi} a(x, y, \xi) Bu(y) dy d\xi \\ &= \int e^{i(x-y)\cdot\xi} a(x, y, \xi) \int e^{i(y-z)\cdot\eta} b(y, z, \eta) u(z) dz d\eta dy d\xi \\ &= \iint e^{i(x-y)\cdot\xi + i(y-z)\cdot\eta} a(x, y, \xi) b(y, z, \eta) u(z) dz d\eta dy d\xi \end{aligned}$$

From this we see immediately from the first line that in order for ABu to be defined, we need for Bu to be compactly supported. This leads to the following definition:

Definition 1.1.3 *The Ψ DO B is called properly supported if Bu and $B^t u$ have compact support.*

Given a Ψ DO $P \in \Psi^m(\Omega)$, it is always possible to find a properly supported Ψ DO $\tilde{P} \in \Psi^m(\Omega)$ such that $P - \tilde{P} \in \Psi^{-\infty}(\Omega)$, so we assume throughout that all Ψ DO's are properly supported. We then wish to write ABu in the following form

$$ABu = \int e^{i(x-y)\cdot\xi} c(x, y, \xi) u(y) dy d\xi$$

with c an amplitude of order to be determined. We note that

$$\begin{aligned} ABu &= \iint e^{i(x-y)\cdot\xi + i(y-z)\cdot\eta} a(x, y, \xi) b(y, z, \eta) u(z) dz d\eta dy d\xi \\ &= \iint e^{i(x-z)\cdot\xi + i(z-y)\cdot\eta} a(x, z, \xi) b(z, y, \eta) u(y) dy d\eta dz d\xi \\ &= \iint e^{i(x-y)\cdot\xi} k(x, y, \xi) u(y) dy d\xi \end{aligned}$$

where

$$k(x, y, \xi) = \iint e^{i(y-z)\cdot(\xi-\eta)} a(x, z, \xi) b(z, y, \eta) dz d\eta.$$

In the second line we swapped y and z in the integral. The integration in the formula for $k(x, y, \xi)$ is understood as an oscillatory integral. By differentiating $k(x, y, \xi)$ it's possible to show that $k(x, y, \xi) \in S^{m+m'}(\Omega, \Omega)$ where $a \in S^m(\Omega, \Omega)$ and $b \in S^{m'}(\Omega, \Omega)$.

Composition allows us to define a parametrix for a Ψ DO, and in turn elliptic Ψ DOs:

Definition 1.1.4 (Elliptic Ψ DO) *A Ψ DO $P \in \Psi^m(\Omega)$ will be called elliptic if there exists $Q \in \Psi^{-m}(\Omega)$ such that $PQ \equiv QP \equiv I \pmod{\Psi^{-\infty}}$. The operator Q will be called a parametrix of P .*

There is an equivalent way to defined elliptic Ψ DO's in terms of symbols, similar to the definition of an elliptic partial differential operator, but we'll make use of the definition above.

1.1.6 The wave front set of a distribution

Definition 1.1.5 (Conic subset of \mathbb{R}^n) A conic set $\Gamma \subset \mathbb{R}^n$ is any set that is closed under dilations, i.e. for all $\lambda > 0$,

$$y \in \Gamma \implies \lambda y \in \Gamma$$

Definition 1.1.6 (Wave front set of a distribution) Let $u \in \mathcal{D}'(\Omega)$ with $\Omega \subset \mathbb{R}^n$. We say that the point $(x_0, \xi_0) \in \Omega \times \mathbb{R}^n$ is not in the wave front set of the distribution u , denoted $\text{WF}(u)$, if there exists a $\phi \in C_0^\infty(\Omega)$ with $\phi(x_0) = 1$ and an open cone $\Gamma \subset \mathbb{R}^n \ni \xi_0$ such that for every N there exists some $C_N > 0$ with

$$|\mathcal{F}(\phi u)(\xi)| \leq C_N(1 + |\xi|)^{-N}$$

for all $\xi \in \Gamma$. Elements $(x, \xi) \in \text{WF}(u)$ are called singularities of u .

The wave front set of a distribution is a refinement of the singular support of a distribution, which is the complement of the largest open set on which u is smooth. One of the key features of Ψ DOs is how they affect the wave front sets of distributions.

Lemma 1.1.1 Properly supported Pseudodifferential operators do not increase wave front sets of distributions, i.e. if $A \in \Psi^m(\Omega)$ and $u \in \mathcal{E}'(\Omega)$, then

$$\text{WF}(Au) \subset \text{WF}(u)$$

This is a generalization of the pseudolocal property for pseudodifferential operators, which states that $\text{sing supp}(Au) \subset \text{sing supp}(u)$, where $\text{sing supp}(u)$ is the singular support of u . If A is an elliptic Ψ DO, then because we can find a parametrix B such that $AB - I \in \Psi^{-\infty}(\Omega)$, this implies that $\text{WF}(Au) = \text{WF}(u)$, and similarly $\text{sing supp}(Au) = \text{sing supp}(u)$.

All of these definitions and concepts have natural generalizations to pseudodifferential operators on smooth manifolds. We refer the reader to Chapter I, section 5 of [34] for more information.

1.1.7 Geometrical optics

Ψ DOs are useful when dealing with elliptic operators, but in some cases we wish to deal with hyperbolic operators, such as the wave operator $\square_c = \partial_t^2 - c^2(x)\Delta$, where $c \in C^\infty(\mathbb{R}^n)$, $c > 0$ and $c \equiv 1$ outside of some compact set $K \subset \mathbb{R}^n$. Note that when $c \equiv 1$, it is easy to see that the initial value problem given by

$$\begin{cases} \square u(x, t) = 0 & (x, t) \in \mathbb{R}^n \times \mathbb{R}^+, \\ u(x, t) |_{t=0} = f & x \in \mathbb{R}^n, \\ \partial_t u(x, t) |_{t=0} = g & x \in \mathbb{R}^n \end{cases}$$

has the solution (for appropriate f and g)

$$u(x, t) = \frac{1}{(2\pi)^n} \left(\int_{\mathbb{R}^n} e^{ix \cdot \xi - t|\xi|} \left(\hat{f} + \frac{\hat{g}}{i|\xi|} \right) d\xi + \int_{\mathbb{R}^n} e^{ix \cdot \xi + t|\xi|} \left(\hat{f} - \frac{\hat{g}}{i|\xi|} \right) d\xi \right).$$

It is from this representation for the solution to the constant speed wave equation that we get the geometric optics ansatz [32]. Suppose we wish to solve the variable speed wave equation:

$$\begin{cases} \square_c u(x, t) = 0 & (x, t) \in \mathbb{R}^n \times \mathbb{R}^+, \\ u(x, t) |_{t=0} = f & x \in \mathbb{R}^n, \\ \partial_t u(x, t) |_{t=0} = g & x \in \mathbb{R}^n. \end{cases} \quad (1.5)$$

The geometric optics ansatz states that the solution to this PDE will be of the following form:

$$u(x, t) = \sum_{\sigma=\pm} \frac{1}{(2\pi)^n} \int_{\mathbb{R}^n} e^{i\phi_\sigma(x, t, \xi)} \left(a_{1, \sigma}(x, t, \xi) \hat{f}(\xi) + a_{2, \sigma}(x, t, \xi) \frac{\hat{g}(\xi)}{|\xi|} \right) d\xi \quad (1.6)$$

where ϕ is assumed to be positive homogeneous of order 1 as in the constant speed case and $a_{j, \sigma}$ are each classical symbols of order 0, again as in the constant speed case. We actually seek $a_{j, \sigma} \sim \sum_{k=0}^{\infty} a_{j, \sigma}^k(x, t, \xi)$ where each $a_{j, \sigma}^k$ is positive homogeneous of order $-j$ in ξ for $|\xi|$ large. In other words, we take $a_{j, \sigma}$ to be classical symbols of order 0. Now the idea is to substitute this ansatz into the wave equation and

cancel terms of the same homogeneity degree. Doing this gives special information about ϕ_σ , namely that ϕ_σ solves the eikonal equation $(\partial_t \phi_\sigma)^2 = c^2(x)|\nabla_x \phi_\sigma|^2$ with initial conditions $\phi_\sigma(0, x, \xi) = x \cdot \xi$. This process also gives information about each $a_{j,\sigma}^k$, namely that they solve specific transport equations that only depend on $a_{j,\sigma}^l$ for $0 \leq l \leq k$. Because of this, we are able to solve for each $a_{j,\sigma}^k$ recursively. We use this process explicitly in Chapter 2, and implicitly in Chapter 3.

1.1.8 Local theory of Fourier integral operators (FIOs)

The form of the solution in (1.6) is an example of what is known as a Fourier integral operator. In general, Fourier integral operators have the form

$$Au(x) = \int e^{i\phi(x,y,\xi)} a(x,y,\xi) f(y) dy d\xi$$

where a is an amplitude (or symbol) and $\phi(x,y,\xi)$ must satisfy the following three conditions:

1. $\phi(x,y,\xi)$ is real valued
2. $\phi(x,y,\xi)$ is positive homogeneous of order 1 in ξ
3. $\phi_{x,\xi} \neq 0$ and $\phi_{y,\xi} \neq 0$ for $\xi \neq 0$

Any $C^\infty(X \times Y \times (\mathbb{R}^N \setminus 0))$ function satisfying the above conditions is called a phase function. It is clear that Ψ DOs are special instances of FIOs with phase function $\phi(x,y,\xi) = (x-y) \cdot \xi$. In fact, some authors, such as [7], first define Fourier integral operators, and then define pseudodifferential operators as special cases of FIOs.

We require ϕ to satisfy the conditions above so that we may apply the method of stationary phase to show that the kernel $I(\phi; a) = \int e^{i\phi(x,y,\xi)} a(x,y,\xi) d\xi$ is C^∞ away from the characteristic manifold associated with A defined by

$$\Sigma_\phi = \{(x,y,\xi) \in X \times Y \times \mathbb{R}^N \setminus 0 \mid \phi_\xi = 0\}. \quad (1.7)$$

In other words, the integral above must be interpreted in the oscillatory integral sense.

1.1.9 The canonical relation associated with an FIO

Assuming ϕ satisfies the above conditions and $a(x, y, \xi)$ is an amplitude with conic support contained in Σ_ϕ , there is a natural relation associated with the operator A called the canonical relation. The conditions on ϕ imply that the map

$$\Sigma_\phi \ni (x, y, \xi) \mapsto (x, \phi_x(x, y, \xi), y, -\phi_y(x, y, \xi)) \in T^*(X \times Y) \setminus 0 \quad (1.8)$$

is an immersion, whose image we'll call C_ϕ . This image is a conic Lagrangian submanifold of $T^*(X \times Y) \setminus 0$ and is called the canonical relation associated with A .

1.1.10 The effect of FIOs on wave front sets

In general, given an FIO, call it A , with canonical relation C , and a distribution u , we have the following inclusion:

$$\text{WF}(Au) \subset C \circ \text{WF}(u),$$

which is analogous to the statement on Ψ DOs and wave front sets. Really, this is a generalization of the statement for Ψ DOs, because viewing a Ψ DO as a special instance as an *FIO*, it is the case that the canonical relation associated with a Ψ DO is the identity relation. In [14], it is shown that if A is an elliptic FIO (that is, if A can be inverted up to a smooth error), then, denoting C as the canonical relation associated with A , given any distribution $u \in \mathcal{E}'$, it is the case that

$$\text{WF}(Au) = C \circ \text{WF}(u). \quad (1.9)$$

In other words, singularities of u are moved by the canonical relation in a predictable way. This makes the microlocal calculus very useful in solving inverse problems related to the recovery of singularities, such as in medical and geological imaging.

2. Thermoacoustic tomography with circular integrating detectors and variable wave speed¹

Thermoacoustic Tomography is a medical imaging method in which a short pulse of electromagnetic radiation is used to excite cells in some object we wish to image, typically the organs of a patient. Upon absorbing the EM radiation, the cells in the patient in turn vibrate, creating ultrasonic waves that then propagate out of the patient and are measured by any number of methods. Using this measured data, we then try to reconstruct, in some sense, an image of the inside of the patient. This is a hybrid imaging method which uses high contrast, low resolution EM radiation to excite the cells, and low contrast, high resolution ultrasound waves as measurement [23]. The hope is to be able to get an image with good contrast and resolution by combining these two types of waves. The case of point-wise measurements with constant and variable wave speed in the region of interest has been studied extensively [18, 28, 35]. Other methods of measurement of the ultrasonic waves include measurements with linear integrating detectors [17], planar integrating detectors [10, 29] and circular integrating detectors or cylindrical stacks of circular integrating detectors [36, 37]. Circular integrating detectors have a few advantages over linear integrating detectors and planar integrating detectors, including compactness of the experimental setup [36]. The case of planar integrating detectors was studied in [29], and that work focused on the problem with a smooth, variable wave speed. The case of circular (and cylindrical) integrating detectors with constant wave speed has been studied in [36, 37]. In those works, explicit formulae are given for reconstruction of an initial pressure density using full measurements, i.e. measurements for every circular integrating detector of a fixed radius with center on the unit circle, for all time. That reconstruction is stable

¹This chapter was submitted to and published in the journal *Inverse Problems and Imaging* [21]

in the case that the object being imaged is contained in the interior of the circular integrating detectors, but is unstable for the case that the object lies entirely outside of the circular integrating detector. The present work focuses on the case of circular integrating detectors in the plane with a 2 dimensional region of interest, i.e. we are focusing on the 2 dimensional problem. Further, we do not make a constant wave speed assumption, we only assume that the wave speed $c(x) > 0$ is smooth in all of \mathbb{R}^2 and is 1 outside of a compact subset of \mathbb{R}^2 . We show that the measurement operator in this case is a Fourier Integral Operator and compute its canonical relation, which happens to be a local diffeomorphism, thus allowing us to determine how singularities in initial data propagate to the measurement data. We also show that this operator is injective and prove stability of the measurement operator, and in addition we prove what singularities in the initial data are visible from a fixed open subset of the set of points on the circle where the measurements are taken in a given time interval. Lastly, we provide numerical results obtained through simulation in Matlab using both full and partial data that support our findings.

2.1 Setup

We begin by defining the space of distributions that our initial pressure distribution must be in. Let

$$H_D(\Omega) = \left\{ f \in \mathcal{E}'(\Omega) \mid \int_{\Omega} |\nabla f|^2 dx < \infty \right\},$$

where $\Omega \subset \mathbb{R}^2$ is open and $\mathcal{E}'(\Omega)$ is the space of distributions compactly supported in Ω . This is the natural space in which to take f when the energy of the system is taken into consideration. Let $\|f\|_{H_D(\Omega)}^2 = \int_{\Omega} |\nabla f|^2 dx$. The space $H_D(\Omega)$ is the completion of $C_0^\infty(\Omega)$ under the given norm. We know $C_0^\infty(\Omega)$ is a normed space taken with this norm for any open Ω so that $H_D(\Omega)$ is indeed a normed space with this norm for any Ω open, and we only work with Ω open and bounded. We further suppose that $\bar{\Omega} \subset B_1(0)$ where $B_1(0)$ is the unit ball in \mathbb{R}^2 centered at the origin. We view f as an initial pressure distribution of some object to be imaged represented by

Ω . Then, after exposing Ω to microwave radiation, the ultrasonic waves created solve the acoustic wave equation given by

$$\begin{cases} \partial_t^2 u(t, x) = c^2(x) \Delta u(t, x), & (t, x) \in \mathbb{R} \times \mathbb{R}^2 \\ u(0, x) = f(x), & f(x) \in H_D(\Omega) \\ \partial_t u(t, x) |_{t=0} = 0, & x \in \mathbb{R}^2 \end{cases} \quad (2.1)$$

where $0 < c(x) \in C^\infty(\mathbb{R}^2)$ is the smooth wave speed, assumed to be known. Outside of Ω , $c \equiv 1$. The problem of interest is to detect these waves, solutions $u(t, x)$ to the above wave equation, with detectors located outside of $B_R(0)$, and then using these measurements, reconstruct the initial pressure distribution f . As mentioned in the introduction, extensive research has been done in the constant speed case ($c(x) \equiv 1$ for all $x \in \mathbb{R}^2$) and variable speed case with point detectors in which we assume access to $u|_{U \times \Gamma}$ where $\Gamma \subset S^1$ is open and $U \subset \mathbb{R}$ is some time interval. Research has also been done for linear and planar integrating detectors in both the constant and variable speed case, and also circular and cylindrical integrating detectors in the constant wave speed case. When imaging with these integrating detectors, instead of assuming direct access to u on some open subset of the boundary of Ω , the measured data is an average of u over a circular detector of radius r centered on the boundary of the ball of radius R (which we will choose later), and data is assumed to be collected on an open subset of of this boundary, not necessarily the entirety of the boundary. The present work considers the problem with variable speed in Ω , and circular integrating detectors. We will have two cases to consider, which we will call the large radius detector case and the small radius detector case, which are depicted in Figure 2.1. The large radius detector case is the experimental setup in which Ω is on the “inside” of the circular integrating detectors, and the small radius detector case is the setup in which Ω is on the “outside” of the circular integrating detector. We note as in [36] that since it is possible to fabricate optical fibers out of materials which have nearly the same acoustical density as the surrounding fluid in which they are contained, there should be little refraction effects expected, and so we will neglect

any interference in ultrasonic waves caused by interaction with the circular integrating detectors.

2.2 Construction

We are interested in seeing what singularities we can recover from rotating a circular integrating detector around some object that has been heated via microwaves. To start, we recall that solving the wave equation (as above) up to a smooth error, for $x \in \mathbb{R}^2$, can be accomplished by use of the geometric optics construction (see Section 3 of [32] or Example 2.1 of chapter VI in [34]). The geometric optics ansatz is that the solution to (2.1) is of the form

$$u(t, x) = \frac{1}{(2\pi)^2} \sum_{\sigma=\pm} \int e^{i\phi_\sigma(t, x, \xi)} a_\sigma(t, x, \xi) \hat{f}(\xi) d\xi,$$

where each $a_\sigma(t, x, \xi)$ is a classical symbol of order 0, and each ϕ_σ is positive homogeneous of order 1 in ξ , i.e. $\phi(t, x, \lambda\xi) = \lambda\phi(t, x, \xi)$ for $\lambda > 0$. The motivation behind this ansatz comes from looking at solutions to (2.1) for the case $c \equiv 1$, in which case the solution to (2.1) is of the form

$$u(t, x) = \frac{1}{(2\pi)^2} \left(\int e^{i(x \cdot \xi + t|\xi|)} \frac{\hat{f}(\xi)}{2} d\xi + \int e^{i(x \cdot \xi - t|\xi|)} \frac{\hat{f}(\xi)}{2} d\xi \right).$$

After substituting our ansatz into (2.1), we obtain the following condition: ϕ_σ solves the *eikonal equation*: $((\phi_\sigma)_t)^2 = c^2(x)|\nabla_x \phi_\sigma|^2$ with initial condition $\phi_\sigma(0, x, \xi) = x \cdot \xi$. The eikonal equation is only solvable locally in time, which results in our solution $u(t, x)$ being only a local solution in time. This will not actually be an issue however, as we can follow a procedure outlined in the proof of Proposition 3 in [28] to construct an Fourier integral operator that is defined for all time. The Fourier Integral Operator that results from this construction is then actually a composition of Fourier Integral Operators. Because of this, we may assume that the eikonal equation is solvable until geodesics intersect circular integrating detectors.

We assumed that a_σ was a classical symbol of order 0, so we may write

$$a_\sigma(t, x, \xi) \sim \sum_{j \geq 0} a_\sigma^{(j)}(t, x, \xi),$$

where $a_\sigma^{(j)}(t, x, \xi)$ is positively homogeneous of order $-j$ for $|\xi|$ large. Because of this, after substituting the geometric ansatz solution for u into 2.1, we find $a_\sigma^{(0)}(t, x, \xi)$ solves the transport equation

$$\left((\partial_t \phi_\sigma) \partial_t - c^2(x) (\nabla_x \phi_\sigma) \cdot \nabla_x + \frac{1}{2} (\partial_t^2 - c^2(x) \Delta_x) \phi_\sigma \right) a_\sigma^{(0)} = 0$$

with initial conditions $a_\sigma^{(0)}(0, x, \xi) = 1/2$. The last term on the left hand side of this equation acts on $a_\sigma^{(0)}$ by multiplication. The lower order terms can be calculated recursively in a similar way.

Note that we may assume that $a_\sigma = 0$ for $|\xi| < R$ for some $R > 0$, as this only affects our solution for $u(t, x)$ by a smooth error [34]. To see this, let $\chi(\xi) \in C_0^\infty(\mathbb{R}^2)$ with $\chi \geq 0$, and $\chi = 1$ for $|\xi| < R$ and $\chi = 0$ for $|\xi| \geq R + \epsilon$ for some R and ϵ positive. Then the operator M' defined by

$$M'_\sigma f(t, x) = \int e^{i\phi_\sigma(t, x, \xi)} a_\sigma(t, x, \xi) \chi(\xi) f(\xi) d\xi,$$

is smooth in (t, x) , because for $m \in \mathbb{N}$ and α a multi-index,

$$\partial_t^m \partial_x^\alpha (e^{i\phi_\sigma(t, x, \xi)} a_\sigma(t, x, \xi) \chi(\xi))$$

is smooth by assumption on ϕ , a and χ , and compactly supported in ξ , so that the integral defining M' is well defined for any m and α . We then note that

$$u(t, x) = \sum_\sigma \frac{1}{(2\pi)^2} \left(\int e^{i\phi_\sigma(t, x, \xi)} (1 - \chi(\xi)) a(t, x, \xi) \hat{f}(\xi) d\xi + M'_\sigma f(t, x) \right)$$

And $(1 - \chi(\xi)) a(t, x, \xi) \equiv 0$ in a neighborhood of $\xi = 0$. So, modulo a smooth function, we may assume that $a(t, x, \xi) \equiv 0$ in a neighborhood of $\xi = 0$.

Now in the situation of Thermoacoustic Tomography using circular integrating detectors around the object we wish to image, the measurements at the detector are given by the circular Radon transform:

$$Mf(t, \theta) = \frac{1}{2\pi} \int_0^{2\pi} u(t, C(\theta, \alpha)) d\alpha,$$

where $C(\theta, \alpha) = R(\cos \theta, \sin \theta) + r(\cos \alpha, \sin \alpha)$ is a parametrization of the circular detector, R is the distance from the origin to the center of the circle, r is the radius of the circular detector, θ is the angle made between the positive horizontal axis and the ray from the origin to the center of the circle, and $u(t, x)$ is the solution to the IVP (2.1). The radius of the circular integrating detector, r , must be chosen so that the detector does not intersect Ω . To accomplish this, we must have either r small enough so that $R-r \geq 1$, guaranteeing the detector does not intersect $\Omega \subset B_1(0)$, or, we could fix $R = 1$ and choose $r \geq 2$, in which case Ω is contained in the interior of the disc defined by the detector (see Figure 2.1). For convenience, we define $\boldsymbol{\theta} = (\cos \theta, \sin \theta)$. We can rewrite Mf by using the δ distribution:

$$Mf(t, \theta) = \frac{1}{\pi} \int_{\mathbb{R}^2} u(t, x) \delta(|x - R\boldsymbol{\theta}|^2 - r^2) dx.$$

We now plug in our solution for u obtained via the geometric optics construction and denote by M_+ and M_- the operators taking $\sigma = +$ and $\sigma = -$ respectively after substituting the geometric optics solution in $Mf(t, \theta)$. Then $Mf = M_+f + M_-f$, where

$$\begin{aligned} M_+f(t, \theta) &= \frac{1}{4\pi^3} \iint_{\mathbb{R}^2 \times \mathbb{R}^2} e^{i\phi_+(t, x, \xi)} a_+(t, x, \xi) \hat{f}(\xi) d\xi \delta(|x - R\boldsymbol{\theta}|^2 - r^2) dx \\ M_-f(t, \theta) &= \frac{1}{4\pi^3} \iint_{\mathbb{R}^2 \times \mathbb{R}^2} e^{i\phi_-(t, x, \xi)} a_-(t, x, \xi) \hat{f}(\xi) d\xi \delta(|x - R\boldsymbol{\theta}|^2 - r^2) dx. \end{aligned}$$

We drop subscripts in the integral for now and consider only M_+ ,

$$M_+f(t, \theta) = \frac{1}{4\pi^3} \iint_{\mathbb{R}^2 \times \mathbb{R}^2} e^{i\phi(t, x, \xi)} a(t, x, \xi) \hat{f}(\xi) d\xi \delta(|x - R\boldsymbol{\theta}|^2 - r^2) dx.$$

We make use of the fact that $\frac{1}{2\pi} \int e^{i\lambda(|x - R\boldsymbol{\theta}|^2 - r^2)} d\lambda = \delta(|x - R\boldsymbol{\theta}|^2 - r^2)$ to say

$$M_+f(t, \theta) = \frac{1}{8\pi^4} \iiint_{\mathbb{R}^2 \times \mathbb{R} \times \mathbb{R}^2} e^{i\phi(t, x, \xi) + i\lambda(|x - R\boldsymbol{\theta}|^2 - r^2)} a(t, x, \xi) \hat{f}(\xi) d\xi d\lambda dx.$$

Lastly, we unpack the Fourier transform of f to get

$$M_+ f(t, \theta) = \frac{1}{8\pi^4} \iiint_{\mathbb{R}^7} e^{i\phi(t,x,\xi) + i\lambda(|x - R\theta|^2 - r^2) - iy \cdot \xi} a(t, x, \xi) f(y) dy d\xi d\lambda dx,$$

where we have identified $\mathbb{R}^2 \times \mathbb{R}^2 \times \mathbb{R} \times \mathbb{R}^2$ with \mathbb{R}^7 . This is an indication that the measurement operator M_+ is a Fourier Integral Operator with phase function

$$\Phi(t, \theta, y; \lambda, x, \xi) = \phi(t, x, \xi) + \lambda(|x - R\theta|^2 - r^2) - y \cdot \xi.$$

One issue with the phase function is that Φ is not homogeneous of degree one in the fiber variables (λ, x, ξ) , but this can be fixed by making a change of variable. Let $\tilde{x} := x |(\xi, \lambda)|$, where $|(\lambda, \xi)| = \sqrt{\lambda^2 + \xi_1^2 + \xi_2^2}$, and define $\tilde{\Phi}(t, \theta, y; \lambda, \tilde{x}, \xi) := \Phi(t, \theta, y; \lambda, \frac{\tilde{x}}{|(\xi, \lambda)|}, \xi)$. This makes $\tilde{\Phi}$ homogeneous of degree one in the variables $(\lambda, \tilde{x}, \xi)$. Further, the derivatives $\tilde{\Phi}_{t, \theta, \lambda, \tilde{x}, \xi}$ and $\tilde{\Phi}_{y, \lambda, \tilde{x}, \xi}$ are nonzero for $(\lambda, \tilde{x}, \xi) \neq 0$, and so this is a true phase function and we can proceed. After making this change of variable, we now write M_+ as

$$M_+ f(t, \theta) = \frac{1}{8\pi^4} \iiint_{\mathbb{R}^7} e^{\tilde{\Phi}(t, \theta, y; \lambda, \tilde{x}, \xi)} \tilde{a}(t, \tilde{x}, \xi, \lambda) f(y) dy d\xi d\lambda d\tilde{x}$$

where

$$\tilde{a}(t, \tilde{x}, \xi, \lambda) = a\left(t, \frac{\tilde{x}}{|(\xi, \lambda)|}, \xi\right) |(\xi, \lambda)|^{-2}.$$

Note that because we assume $a(t, x, \xi) \equiv 0$ near $\xi = 0$, there is no singularity caused by the factor of $|(\lambda, \xi)|^2$ in $\tilde{a}(t, \tilde{x}, \xi, \lambda)$. Also, because a is an amplitude of order 0, we can see that $\tilde{a}(t, \tilde{x}, \lambda, \xi)$ is an amplitude of order -2 , and by [13], M_+ is a Fourier integral operator of order $-1/2$. Note that this change of variable does not affect the characteristic manifold for Φ , which is defined as the variety

$$\Sigma = \{(t, \theta, y; \lambda, x, \xi) \mid \Phi_{\lambda, x, \xi} = 0\}.$$

To see that this set is unaffected, note that

$$\begin{aligned}\tilde{\Phi}_\lambda &= \Phi_\lambda + \Phi_x \cdot \left(\frac{\tilde{x}}{|(\xi, \lambda)|} \right)_\lambda, \\ \tilde{\Phi}_{\tilde{x}} &= \Phi_x \frac{1}{|(\xi, \lambda)|}, \\ \tilde{\Phi}_\xi &= \Phi_\xi + \Phi_x \cdot \left(\frac{\tilde{x}}{|(\xi, \lambda)|} \right)_\xi,\end{aligned}$$

so that $\tilde{\Phi}_{\tilde{x}} = 0$ if and only if $\Phi_x = 0$, from which it is clear that $\tilde{\Phi}_{\lambda, \tilde{x}, \xi} = 0$ if and only if $\Phi_{\lambda, x, \xi} = 0$.

We wish to find the characteristic manifold and canonical relation associated with the measurement operator M_+ . Taking the derivative of Φ with respect to (λ, x, ξ) , we see that this gives the system of equations

$$\begin{aligned}|x - R\boldsymbol{\theta}|^2 - r^2 &= 0 \\ \phi_x + 2\lambda(x - R\boldsymbol{\theta}) &= 0 \\ \phi_\xi - y &= 0\end{aligned}$$

We've made no assumption on which experimental setup we've chosen to examine so far. There are two different cases, as mentioned above: (1) $R - r \geq 1$, which we will call the small radius case, and (2) $R = 1$ with $r \geq 2$, which we will call the large radius case. The analysis of these two cases are largely the same, but with a few key differences. We examine both cases.

2.2.1 Case 1: Small Radius

From the system of equations obtained by looking at the characteristic manifold of the FIO, we see that $\phi_\xi = y$, and by the geometric optics construction, x lies on the geodesic $\gamma_{y, \hat{\xi}}(t)$ issued from $(y, \hat{\xi})$ where $\hat{\xi} = \xi/(c|\xi|)$ is the unit covector in the metric identified with a unit vector, and $(\gamma_{y, \hat{\xi}}(t), c|\xi|\dot{\gamma}_{y, \hat{\xi}}(t)) = (x, \phi_x)$. Now from the

first equation, we know that $x = (x_1, x_2)$ must lie on the circular integrating detector of radius r with center $R\boldsymbol{\theta}$. So x is the intersection of the geodesic $\gamma_{y,\xi}$ with the circle defined by $|x - R\boldsymbol{\theta}|^2 = r^2$. There are two of these points of intersection in general (we will show that the geodesic does not intersect the circular integrating detector tangentially if the singularity is to be detected), which we label $x_{+,1}(y, \xi)$ and $x_{+,2}(y, \xi)$. Also denote the times at which these intersections occur $t_{+,1}(y, \xi) > 0$ and $t_{+,2}(y, \xi) > 0$ respectively.

Finally, we have from the second equation $\phi_x = 2\lambda(R\boldsymbol{\theta} - x)$. This tells us that $\dot{\gamma}_{y,\xi}(t)$ is parallel to $x - R\boldsymbol{\theta}$, provided that $\lambda \neq 0$ (in which case $\gamma_{y,\xi}(t)$ intersects the circular integrating detector tangentially). Supposing for a moment that $\lambda = 0$, then taking magnitudes on both sides of the equation $\phi_x(t, x, \xi) = 2\lambda(R\boldsymbol{\theta} - x)$, we obtain $|\phi_x(t, x, \xi)| = 0 \implies c(y)|\xi||\dot{\gamma}_{y,\xi}(t)| = 0$. This in turn means $|\dot{\gamma}_{y,\xi}(t)| = 0$ as $c(y) \neq 0$ for any $y \in \mathbb{R}^2$ and ξ is a non zero vector. But we know near the integrating detectors, that $|\dot{\gamma}_{y,\xi}(t)| = 1$, a contradiction, so $\lambda \neq 0$ on the characteristic manifold. And so the geodesic intersects the circular detector perpendicularly. We know that $\phi_x = c|\xi|\dot{\gamma}_{y,\xi}(t)$, And $c \equiv 1$ outside of the region of interest, so that

$$|\lambda_{+,i}| := c(y)/(2r)|\xi||(\dot{\gamma}_{y,\xi}(t_{+,i}))| = c(y)/(2r)|\xi|.$$

Note that $\lambda_{+,1} > 0$ and $\lambda_{+,2} < 0$, so that $\lambda_{+,1} = c(y)/(2r)|\xi|$ and $\lambda_{+,2} = -\lambda_{+,1}$. We'll simply denote $\lambda_+ := \lambda_{+,1}$. Because $\gamma_{y,\xi}(t)$ intersects the circular integrating detector perpendicularly, it must go through the center of the circular integrating detector, as outside of Ω , we know that $c \equiv 1$ implies that $\gamma_{y,\xi}$ is a straight line near the integrating detectors, and so we see that $\boldsymbol{\theta} = \gamma_{y,\xi}(t_{+,1}(y, \xi) + r)/R = \gamma_{y,\xi}(t_{+,2}(y, \xi) - r)/R$, where r is the fixed radius of the circular integrating detector. This gives then the entire characteristic manifold parameterize by (y, ξ) , giving a smooth manifold of dimension 4 consisting of 2 connected parts. Define

$$\Sigma_{+,1} = \{(t_{+,1}(y, \xi), \boldsymbol{\theta}(y, \xi), y; \lambda_+(y, \xi), x_{+,1}(y, \xi), \xi) \mid (y, \xi) \in T^*(\Omega) \setminus \{0\}\},$$

and

$$\Sigma_{+,2} = \{(t_{+,2}(y, \xi), \boldsymbol{\theta}(y, \xi), y; -\lambda_+(y, \xi), x_{+,2}(y, \xi), \xi) \mid (y, \xi) \in T^*(\Omega) \setminus \{0\}\}.$$

Then $\Sigma_+ = \Sigma_{+,1} \cup \Sigma_{+,2}$ as a disjoint union.

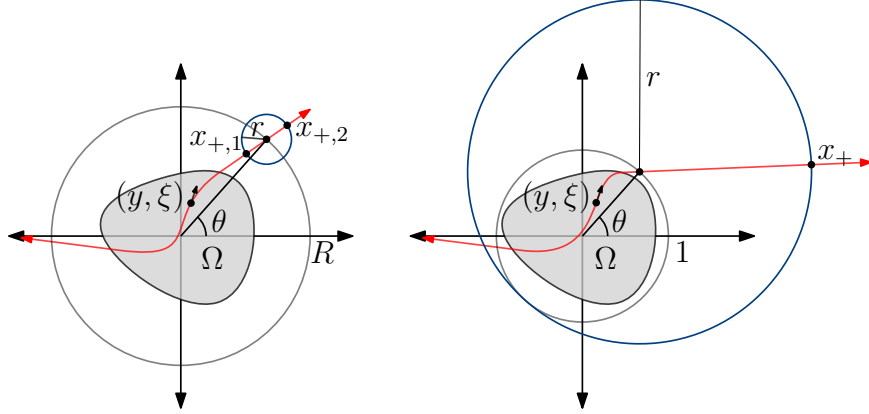


Figure 2.1. Two different experimental setups shown depending on the radius of the integrating detector. On the left is the small radius case, and on the right is the large radius case.

The maps given by

$$\Sigma_+ \ni (t, \boldsymbol{\theta}, y; \lambda, x, \xi) \mapsto (t, \boldsymbol{\theta}, y; \Phi_t, \Phi_\theta, \Phi_y)$$

are calculated as

$$\Sigma_+ \ni (t, \boldsymbol{\theta}, y; \lambda, x, \xi) \mapsto (t, \boldsymbol{\theta}, y; -c(y)|\xi|, -\frac{R}{r}c(y)|\xi|(x - (x \cdot \boldsymbol{\theta})\boldsymbol{\theta}), -\xi)$$

The analysis for $\sigma = -$ is the same giving us $t_{-,i}(y, \xi) < 0, x_{-,i}(y, \xi)$ for $i = 1, 2$ and $\boldsymbol{\theta}_-$. We also see that $\lambda_{-,1} < 0$ and $\lambda_{-,2} > 0$. Denote $\lambda_- := \lambda_{-,1}$. We see that the maps

$$\Sigma_\pm \ni (t, \boldsymbol{\theta}, y; \lambda, x, \xi) \mapsto (t, \boldsymbol{\theta}, y; \mp c(y)|\xi|, \mp \frac{R}{r}c(y)|\xi|(x - (x \cdot \boldsymbol{\theta})\boldsymbol{\theta}), -\xi)$$

are smooth and of rank 4 making M a non-degenerate FIO (see [34] chapter VIII).

This means the canonical relations associated to the operators M_+ and M_- are local graphs given by

$$\begin{aligned}
C_{\pm} &:= \{(t, \boldsymbol{\theta}, \Phi_t, \Phi_{\boldsymbol{\theta}}; y, -\Phi_y) \mid (t, \boldsymbol{\theta}, y; \lambda, x, \xi) \in \Sigma_{\pm}\} \\
&= \left\{ \left(t_{\pm, i}, \boldsymbol{\theta}_{\pm}, \mp c(y)|\xi|, \mp \frac{R}{r} c(y)|\xi| (\gamma_{y, \hat{\xi}}(t_{\pm, i}) - (x_{\pm, i} \cdot \boldsymbol{\theta}_{\pm}) \boldsymbol{\theta}_{\pm}); y, \xi \right) \right\}
\end{aligned}$$

such that $(y, \xi) \in T^*(\Omega) \setminus 0$, where $i = 1, 2$. Here, $\boldsymbol{\theta}_+ = \gamma_{y, \hat{\xi}}(t_{+, 1}(y, \xi) + r)/R$ and $\boldsymbol{\theta}_- = \gamma_{y, \hat{\xi}}(t_{-, 1}(y, \xi) - r)/R$. Writing this as a mapping, we have

$$\begin{aligned}
C_{\pm} : (y, \xi) &\mapsto \\
&\left\{ \begin{aligned} &\left(t_{\pm, 1}, \boldsymbol{\theta}_{\pm}, \mp c(y)|\xi|, \pm \frac{R}{r} c(y)|\xi| \left((x_{\pm, 1} \cdot \boldsymbol{\theta}_{\pm}) \gamma_{y, \hat{\xi}}(t_{\pm, 1} \pm r) - \gamma_{y, \hat{\xi}}(t_{\pm, 1}) \right) \right) \\ &\left(t_{\pm, 2}, \boldsymbol{\theta}_{\pm}, \mp c(y)|\xi|, \mp \frac{R}{r} c(y)|\xi| \left((x_{\pm, 2} \cdot \boldsymbol{\theta}_{\pm}) \gamma_{y, \hat{\xi}}(t_{\pm, 2} \mp r) - \gamma_{y, \hat{\xi}}(t_{\pm, 2}) \right) \right) \end{aligned} \right\}
\end{aligned}$$

Where $x_{\pm, i} = x_{\pm, i}(y, \xi)$, $\boldsymbol{\theta}_{\pm} = \boldsymbol{\theta}_{\pm}(y, \xi)$, and $t_{\pm, 1} = t_{\pm, 1}(y, \xi)$ and similarly, $t_{\pm, 2} = t_{\pm, 2}(y, \xi)$. The canonical relations for the operators M_+ and M_- are each one to two and of the above form. The above has shown the following:

Theorem 2.2.1 *For $R - r \geq 1$, the operator $Mf = M_+f + M_-f$ defined above is a Fourier Integral Operator of order $-1/2$ associated with the graphs of canonical relation given by*

$$C = C_+ \cup C_-,$$

where

$$C_{\pm} = \left\{ \left(t_{\pm, i}, \boldsymbol{\theta}_{\pm}, \mp c(y)|\xi|, \pm (-1)^i \frac{R}{r} c(y)|\xi| \left(\gamma_{y, \hat{\xi}}(t_{\pm, i}) - (x_{\pm, i}(y, \xi) \cdot \boldsymbol{\theta}_{\pm}) \boldsymbol{\theta}_{\pm} \right); y, \xi \right) \right\},$$

$(t_{\pm, i} = t_{\pm, i}(y, \xi) \text{ and } \boldsymbol{\theta}_{\pm} = \boldsymbol{\theta}_{\pm}(y, \xi)) \text{ with } (y, \xi) \in T^*(\Omega) \setminus 0 \text{ and } i = 1, 2.$

Note that this canonical relation is locally one to four.

2.2.2 Case 2: Large Radius

In this case, the analysis is almost entirely the same, except there is only one point of intersection of the geodesic $\gamma_{y,\xi}(t)$ with the circular integrating detector defined by $|x-\boldsymbol{\theta}| = r$ (see Figure 2.1). We then have $\Sigma_{\pm} = \{(t_{\pm}(y, \xi), \boldsymbol{\theta}_{\pm}(y, \xi), y; \pm\lambda(y, \xi), x_{\pm}(y, \xi), \xi) \mid (y, \xi) \in T^*(\Omega) \setminus \{0\}\}$, and the canonical relations are given by

$$C_{\pm} = \left\{ \left((t_{\pm}, \boldsymbol{\theta}_{\pm}, \mp c(y)|\xi|, \mp \frac{1}{r}c(y)|\xi|(\gamma_{y,\xi}(t_{\pm}) - (x_{\pm} \cdot \boldsymbol{\theta}_{\pm})\boldsymbol{\theta}_{\pm}); y, \xi) \mid (y, \xi) \in T^*(\Omega) \setminus 0 \right) \right\}.$$

Here $t_{\pm} = t_{\pm}(y, \xi)$, $\boldsymbol{\theta}_{\pm} = \boldsymbol{\theta}_{\pm}(y, \xi)$ and $x_{\pm} = x_{\pm}(y, \xi)$. The canonical relations are each (local) graphs in this case, and we have an analogous result as in the first case:

Theorem 2.2.2 *For $R = 1$ and $r \geq 2$, the operator $Mf = M_+f + M_-f$ defined above is a Fourier Integral Operator of order $-1/2$ associated with the graph of the canonical relation given by*

$$C = C_+ \cup C_-,$$

where

$$C_{\pm} = \left\{ \left((t_{\pm}, \boldsymbol{\theta}_{\pm}, \mp c(y)|\xi|, \mp \frac{1}{r}c(y)|\xi|(\gamma_{y,\xi}(t_{\pm}) - (x_{\pm} \cdot \boldsymbol{\theta}_{\pm})\boldsymbol{\theta}_{\pm}); y, \xi) \mid (y, \xi) \in T^*(\Omega) \setminus 0 \right) \right\},$$

with $t_{\pm} = t_{\pm}(y, \xi)$, $\boldsymbol{\theta}_{\pm} = \boldsymbol{\theta}_{\pm}(y, \xi)$ and $x_{\pm} = x_{\pm}(y, \xi)$.

This canonical relation is locally one to two, as each individual canonical map is locally one to one.

Note that the maps C_+ and C_- are not globally one to one, although each are locally one to one, for suppose (looking only at C_+ for a moment)

$$(t(y_1, \xi_1), \boldsymbol{\theta}(y_1, \xi_1), \tau(y_1, \xi_1), \omega(y_1, \xi_1)) = (t(y_2, \xi_2), \boldsymbol{\theta}(y_2, \xi_2), \tau(y_2, \xi_2), \omega(y_2, \xi_2))$$

where $\tau(y, \xi) = -c(y)|\xi|$ and $\omega(y, \xi) = -\frac{1}{r}c(y)|\xi|(x - (x \cdot \boldsymbol{\theta})\boldsymbol{\theta}(y, \xi))$ and $x = \gamma_{y,\xi}(t(y, \xi))$.

We'll call $x_i = x(y_i, \xi_i)$ for $i = 1, 2$. Then clearly we have $t(y_1, \xi_1) = t(y_2, \xi_2)$ and

$\boldsymbol{\theta}(y_1, \xi_1) = \boldsymbol{\theta}(y_2, \xi_2)$, which we'll just label t and $\boldsymbol{\theta}$ respectively. We also clearly have $c(y_1)|\xi_1| = c(y_2)|\xi_2|$. Suppose for a moment that $(x_1 - x_2) \cdot \boldsymbol{\theta}^\perp = 0$ where $\boldsymbol{\theta}^\perp = (-\sin(\theta), \cos(\theta))$ is the unit vector perpendicular to $\boldsymbol{\theta}$. Then note that

$$\begin{aligned}\omega(y_1, \xi_1) - \omega(y_2, \xi_2) &= x_1 - (x_1 \cdot \boldsymbol{\theta})\boldsymbol{\theta} - (x_2 - (x_2 \cdot \boldsymbol{\theta})\boldsymbol{\theta}) \\ &= (x_1 - x_2) - [(x_1 - x_2) \cdot \boldsymbol{\theta}]\boldsymbol{\theta}\end{aligned}$$

Now note that $(\omega(y_1, \xi_1) - \omega(y_2, \xi_2)) \cdot \boldsymbol{\theta} = 0$ and $(\omega(y_1, \xi_1) - \omega(y_2, \xi_2)) \cdot \boldsymbol{\theta}^\perp = 0$. Because $\boldsymbol{\theta}$ and $\boldsymbol{\theta}^\perp$ are linearly independent, this shows that $\omega(y_1, \xi_1) - \omega(y_2, \xi_2) = 0$ or in other words that $\omega(y_1, \xi_1) = \omega(y_2, \xi_2)$. This shows that, provided $t(y_1, \xi_1) = t(y_2, \xi_2)$, $\boldsymbol{\theta}(y_1, \xi_1) = \boldsymbol{\theta}(y_2, \xi_2)$, $c(y_1)|\xi_1| = c(y_2)|\xi_2|$ and $(x_1 - x_2) \cdot \boldsymbol{\theta}^\perp = 0$, that (y_1, ξ_1) and (y_2, ξ_2) get mapped to the same point under the canonical relation. However, for c close enough to 1, this will not happen locally.

2.3 Injectivity

2.3.1 Case 1: Small Radius

Let $u(t, x)$ be the solution to (2.1) and $\Gamma \subset S^1$ be open. In local coordinates, suppose Γ is the open interval given by $\Gamma = (\theta_1, \theta_2)$, with $0 \leq \theta_1 < \theta_2 < 2\pi$. Then, for $\boldsymbol{\theta} = (\cos(\theta), \sin(\theta)) \in \Gamma$, we have

$$Mf(t, \theta) = \frac{1}{2\pi} \int_0^{2\pi} u(t, R_0 \cos(\theta) + r \cos(\alpha), R_0 \sin(\theta) + r \sin(\alpha)) d\alpha$$

Where R_0 is the distance from the origin to the center of the circular integrating detector. For fixed $r > 0$, we may view R as variable with $R \geq R_0 \geq 1 + r$ (i.e. we may translate the circular integrating detectors away from the region of interest). We denote this by letting $Mf(t, \theta)$ vary with R and denote the operator then as

$Mf(t, \theta; R)$ and note $Mf(t, \theta) = Mf(t, \theta; R_0)$. Let $P(t, \theta, R) = Mf(t, \theta; R)$. Then we see that

$$\begin{cases} R^2 P_{tt}(t, \theta, R) - R(RP_R(t, \theta, R))_R - P_{\theta\theta}(t, \theta, R) = 0 & (t, \theta, R) \in \mathbb{R}^+ \times \tilde{\Gamma}, \\ P(t, \theta, R_0) = Mf(t, \theta) |_{\theta \in \Gamma}, & (t, \theta) \in \mathbb{R}^+ \times \Gamma, \\ P(0, \theta, R) = 0, & (\theta, R) \in \tilde{\Gamma}, \\ P_t(0, \theta, R) = 0, & (\theta, R) \in \tilde{\Gamma}, \end{cases} \quad (2.2)$$

where $\tilde{\Gamma} = \Gamma \times [R_0, \infty)$. This can be seen as follows: first note to save space, u and all of its partial derivatives are understood to be evaluated at $(t, R \cos(\theta) + r \cos(\alpha), R \sin(\theta) + r \sin(\alpha))$. We have

$$P_\theta(t, \theta, R) = \frac{1}{2\pi} \int_0^{2\pi} (-R \sin(\theta))u_x + (R \cos(\theta))u_y \, d\alpha,$$

and so we have

$$\begin{aligned} P_{\theta\theta} = & \\ & \frac{1}{2\pi} \int_0^{2\pi} R^2 \sin^2(\theta)u_{xx} - 2R^2 \sin(\theta) \cos(\theta)u_{xy} + R^2 \cos^2(\theta)u_{yy} \\ & - R \cos(\theta)u_x - R \sin(\theta)u_y \, d\alpha. \end{aligned}$$

Noting that

$$\begin{aligned} & R^2 \sin^2(\theta)u_{xx} + R^2 \cos^2(\theta)u_{yy} \\ & = R^2 \sin^2(\theta)u_{xx} + R^2 \cos^2(\theta)u_{xx} + R^2 \sin^2(\theta)u_{yy} + R^2 \cos^2(\theta)u_{yy} \\ & \quad - (R^2 \cos^2(\theta)u_{xx} + R^2 \sin^2(\theta)u_{yy}) \\ & = R^2 \Delta u - (R^2 \cos^2(\theta)u_{xx} + R^2 \sin^2(\theta)u_{yy}), \end{aligned}$$

we see that

$$\begin{aligned} P_{\theta\theta}(t, \theta, R) = & \\ & \frac{1}{2\pi} \int_0^{2\pi} R^2 \Delta u - (R^2 \cos^2(\theta)u_{xx} + R^2 \sin^2(\theta)u_{yy} + 2R^2 \sin(\theta) \cos(\theta)u_{xy} \\ & + R \cos(\theta)u_x + R \sin(\theta)u_y) \, d\alpha. \end{aligned}$$

Remembering that Δu above is evaluated at $(t, R \cos(\theta) + r \cos(\alpha), R \sin(\theta) + r \sin(\alpha))$, where $c \equiv 1$, we have

$$\begin{aligned} P_{\theta\theta}(t, \theta, R) = & \\ & \frac{1}{2\pi} \int_0^{2\pi} R^2 c^2 \Delta u - (R^2 \cos^2(\theta) u_{xx} + R^2 \sin^2(\theta) u_{yy} + 2R^2 \sin(\theta) \cos(\theta) u_{xy} \\ & + R \cos(\theta) u_x + R \sin(\theta) u_y) d\alpha, \end{aligned}$$

so that

$$\begin{aligned} P_{\theta\theta}(t, \theta, R) = & \frac{1}{2\pi} R^2 \int_0^{2\pi} u_{tt} d\alpha - \\ & \frac{1}{2\pi} \int_0^{2\pi} (R^2 \cos^2(\theta) u_{xx} + R^2 \sin^2(\theta) u_{yy} + 2R^2 \sin(\theta) \cos(\theta) u_{xy} + \\ & R \cos(\theta) u_x + R \sin(\theta) u_y) d\alpha, \end{aligned}$$

and

$$\frac{1}{2\pi} \int_0^{2\pi} u_{tt} d\alpha = \frac{1}{2\pi} \left(\int_0^{2\pi} u d\alpha \right)_{tt} = P_{tt}(t, \theta, R).$$

So we only need to show that

$$\begin{aligned} R(RP_R)_R = & \\ & \frac{1}{2\pi} \int_0^{2\pi} (R^2 \cos^2(\theta) u_{xx} + R^2 \sin^2(\theta) u_{yy} + 2R^2 \sin(\theta) \cos(\theta) u_{xy} + \\ & R \cos(\theta) u_x + R \sin(\theta) u_y) d\alpha. \end{aligned}$$

This follows from direct calculation and the chain rule.

Rewriting (2.2) in a more standard form, we have:

$$\begin{cases} P_{tt}(t, \theta, R) - \frac{1}{R}(RP(t, \theta, R)_R)_R - \frac{1}{R^2}P_{\theta\theta}(t, \theta, R) = 0, & (t, \theta, R) \in \mathbb{R}^+ \times \tilde{\Gamma}, \\ P(t, \theta, R_0) = Mf(t, \theta) |_{\theta \in \Gamma}, & (t, \theta) \in \mathbb{R}^+ \times \Gamma, \\ P(0, \theta, R) = 0, & (\theta, R) \in \tilde{\Gamma}, \\ P_t(0, \theta, R) = 0, & (\theta, R) \in \tilde{\Gamma}. \end{cases} \quad (2.3)$$

where again $\tilde{\Gamma} = \Gamma \times [R_0, \infty)$. We note that (2.3) simply says that $P(t, \theta, R)$ is a solution to the constant speed wave equation in polar coordinates with initial conditions $P(0, \theta, R) = 0$ for $R \geq R_0 > 1 + r$, $P_t(0, \theta, R) = 0$ and $P(t, \theta, R_0) = Mf(t, \theta)$

for $t \geq 0$ and $\theta \in \Gamma$. It is well known that the wave equation on an open subset of \mathbb{R}^2 has a unique solution (See Chapter 6, Section 2 of [33] or Chapter 5, Section 1(d) of [15]), and so the solution to (2.3) is unique. To show then that $Mf(t, \theta) |_{\theta \in \Gamma}$ uniquely determines f , we need to show that $Mf(t, \theta) |_{\theta \in \Gamma} = 0 \implies f(x) = 0$ by the linearity of M . So then, we assume that $Mf(t, \theta) \equiv 0$ for $t \in \mathbb{R}^+$ and $\theta \in \Gamma$. By the uniqueness of solutions to the wave equation, this tells us that $P(t, \theta, R) \equiv 0$ for any $(t, \theta, R) \in \mathbb{R}^+ \times \Gamma \times [R_0, \infty)$. Let $T \in \mathbb{R}$. We may extend $u(t, x)$ in an even way for $|t| < T$ so that u is still a solution to the wave equation, and so we may extend $P(t, \theta, R)$ in an even way such that $P(t, \theta, R) = 0$ for $|t| < T$. By finite speed of propagation, we know that $\text{supp } u(T, \cdot) \subset B_{1+T}(0)$. Let $\theta_0 \in \Gamma$. Note that the set $\mathcal{A} = \{(\theta, R) \mid \theta \in \Gamma, R > R_0\}$ is open and connected in \mathbb{R}^2 , because $\Gamma \subset S^1$ is an open interval. We know that the circular Radon transform of $u(T, \cdot)$ is 0 for any $\theta \in \Gamma$ and for any $R > R_0$. Further, because the interior of these circular integrating detectors is just $D(\theta, R) = B_r(R\theta)$, we can take $R > R_0$ large enough so that $\text{supp } u(T, \cdot) \cap D(\theta_0, R) = \emptyset$, because $\text{supp } u(T, \cdot)$ is contained in a bounded set. It follows then by Theorem 1.2 in [25] that $\text{supp } u(T, \cdot)$ is disjoint from $\cup_{(\theta, R) \in \mathcal{A}} D(\theta, R)$. So in particular, there is a neighborhood V of $x_0 = R_0\theta_0$ such that $u(T, x) = 0$ on V . T was chosen arbitrarily, so this result holds for all $|t| < T$, and so by Tataru's unique continuation, $u(t, x) \equiv 0$ in the domain of influence $|t| + \text{dist}(x, x_0) < T$. So, taking T large enough so that $\text{dist}(x, x_0) < T$ for all $x \in \Omega$, we see that $u(0, x) = f(x) \equiv 0$, and so $Mf(t, \theta) |_{[0, T] \times \Gamma}$ uniquely determines f .

2.3.2 Case 2: Large Radius

Again, we consider $u(t, x)$ a solution to (2.1). We consider only the full data case $\Gamma = S^1$. Then in this case, in which $R = 1$, we have that the measurement operator $Mf(t, \theta)$ is given by

$$Mf(t, \theta) = \frac{1}{2\pi} \int_0^{2\pi} u(t, \cos(\theta) + r_0 \cos(\alpha), \sin(\theta) + r_0 \sin(\alpha)) d\alpha$$

where $r_0 \geq 2$ is the fixed radius of the circular integrating detector. We may however view r as variable, noting the operator with variable detector radius by

$$Mf(t, \theta; r) = \frac{1}{2\pi} \int_0^{2\pi} u(t, \cos(\theta) + r \cos(\alpha), \sin(\theta) + r \sin(\alpha)) d\alpha$$

Where $r \geq r_0 \geq 2$. Let $P(t, \theta, r) = Mf(t, \theta; r)$, where $\theta \in \Gamma$ and $r \geq r_0 > 2$. Note that $P(t, \theta, r_0) = Mf(t, \theta)$ for $\theta \in \Gamma$. It follows then that $P(t, \theta, r)$ solves the following PDE:

$$\begin{cases} P_{tt}(t, \theta, r) - \frac{1}{r}(rP_r(t, \theta, r))_r = 0 & (t, \theta, r) \in \mathbb{R}^+ \times \Gamma \times [r_0, \infty) \\ P(t, \theta, r_0) = Mf(t, \theta) & (t, \theta) \in \mathbb{R}^+ \times \Gamma \\ P(0, \theta, r) = 0 & (\theta, r) \in \Gamma \times [r_0, \infty) \\ P_t(0, \theta, r) = 0 & (\theta, r) \in \Gamma \times [r_0, \infty) \end{cases} \quad (2.4)$$

We see this as follows: (Again note that u and all of its partial derivatives are understood to be evaluated at $(t, \cos(\theta) + r \cos(\alpha), \sin(\theta) + r \sin(\alpha))$.) We have

$$P_r(t, \theta, r) = \frac{1}{2\pi} \int_0^{2\pi} \cos(\alpha)u_x + \sin(\alpha)u_y d\alpha.$$

We integrate by parts to get

$$P_r(t, \theta, r) = \frac{1}{2\pi} \int_0^{2\pi} (r \sin^2 \alpha)u_{xx} - 2r \cos(\alpha) \sin(\alpha)u_{xy} + (r \cos^2(\alpha))u_{yy} d\alpha.$$

Then, we use the fact that

$$r \sin^2(\alpha)u_{xx} + r \cos^2(\alpha)u_{yy} = r\Delta u - r \cos^2(\alpha)u_{xx} - r \sin^2(\alpha)u_{yy},$$

to obtain

$$P_r(t, \theta, r) = \frac{1}{2\pi} \int_0^{2\pi} r\Delta u - r(\cos^2(\alpha)u_{xx} + 2 \cos(\alpha) \sin(\alpha)u_{xy} + \sin^2(\alpha)u_{yy}) d\alpha.$$

We recall that u and its derivatives are evaluated at $(t, \cos(\theta) + r \cos(\alpha), \sin(\theta) + r \sin(\alpha))$ where $c \equiv 1$, so that $\Delta u = u_{tt}$ there and we see that

$$\begin{aligned}
& P_r(t, \theta, r) \\
&= r \frac{1}{2\pi} \int_0^{2\pi} u_{tt} d\alpha - r \frac{1}{2\pi} \int_0^{2\pi} \cos^2(\alpha) u_{xx} + 2 \cos(\alpha) \sin(\alpha) u_{xy} + \sin^2(\alpha) u_{yy} d\alpha \\
&= r P_{tt}(t, \theta, r) - r \frac{1}{2\pi} \int_0^{2\pi} \cos^2(\alpha) u_{xx} + 2 \cos(\alpha) \sin(\alpha) u_{xy} + \sin^2(\alpha) u_{yy} d\alpha \\
&= r P_{tt}(t, \theta, r) - r P_{rr}(t, \theta, r).
\end{aligned}$$

The last line can be seen by direct calculation of $P_{rr}(t, \theta, r)$. Rearranging we see $rP_{tt} = rP_{rr} + P_r$ and (2.4) then follows. This partial differential equation is the wave equation with axial symmetry in an open subset of \mathbb{R}^2 , and so solutions to this equation are again unique by [15, 33].

To show that $Mf(t, \theta)$ determines f uniquely for $\theta \in \Gamma$, by the linearity of M , we need only show that $Mf(t, \theta) = 0$ for all $(t, \theta) = [0, T) \times \Gamma \implies f = 0$. We note that $Mf(t, \theta) = 0$ for all $(t, \theta) \in [0, T) \times \Gamma \implies P(t, \theta, r) \equiv 0$, because $P(t, \theta, r) \equiv 0$ clearly solves the PDE (2.4) in this case, and this solution is unique. For any $T \in \mathbb{R}$, we know that $\text{supp } u(T, \cdot) \subset B_{1+T}(0)$, and so for any finite T , $u(T, \cdot)$ has bounded support. Let $\theta_0 \in \Gamma$, $T \in \mathbb{R}^+$. Let $r_1 = \sup\{r \geq r_0 \mid C(\theta_0, r) \cap \text{supp } u(T, \cdot) \neq \emptyset\}$, where $C(\theta_0, r)$ is the circle centered at θ_0 with radius r . We know, because $\text{supp } u(T, \cdot) \subset B_{1+T}(0)$, that $\{r \geq r_0 \mid C(\theta_0, r) \cap \text{supp } u(T, \cdot) \neq \emptyset\}$ is bounded above by $2 + T$. Assume that this set is nonempty so that $r_1 \geq r_0$ is finite. Then we have $C(\theta_0, r_1) \cap \text{supp } u(T, \cdot) \neq \emptyset$ by the compactness of $\text{supp } u(T, \cdot)$. Let $x \in C(\theta_0, r_1) \cap \text{supp } u(T, \cdot)$, and let $(x, \xi) \in N^*(C(\theta_0, r_1))$. By construction, $\text{supp } u(T, \cdot)$ is on one side of $C(\theta_0, r_1)$ at x , so that by Theorem 8.5.6 in [14], we have that $(x, \xi) \in \text{WF}_A(u(T, \cdot))$. Note that as in the terminology of [25], it is impossible for x to be a $C(\theta_0, r_1)$ self mirror point, for tracing (x, ξ) back along the geodesic defined by (x, ξ) , we see that the geodesic never intersects the interior of $B_1(0)$, which is impossible. So then, there are two cases we must consider. First we consider the case where the $C(\theta_0, r_1)$ mirror point of x , which we will call \tilde{x} , is not in the intersection $C(\theta_0, r_1) \cap \text{supp } u(T, \cdot)$. Then, by the compactness of $\text{supp } u(T, \cdot)$, we have $u(T, \cdot) = 0$ in a neighborhood of \tilde{x} . We also have $P(T, \theta, r) = 0$ in a neighborhood of $(\theta_0, r_1) \in \Gamma \times [r_0, \infty)$. It then follows

by Proposition 2.4 of [25] that $(x, \xi) \notin \text{WF}_A(u(T, \cdot))$, a contradiction to $(x, \xi) \in \text{WF}_A(u(T, \cdot))$. It follows that $\{r \geq r_0 \mid C(\theta_0, r) \cap \text{supp } u(T, \cdot) \neq \emptyset\}$ is empty and so $\text{supp } u(T, \cdot) \subset \bar{B}_{r_0}(\theta_0)$.

The second case we consider is that \tilde{x} is in the intersection $C(\theta_0, r_1) \cap \text{supp } u(T, \cdot)$. We'll show that there then exists $\theta_1 \in S^1$ and $r_2 > r_1$, such that

$$C(\theta_1, r_2) \cap \text{supp } u(T, \cdot) = \{\tilde{x}\}.$$

Assume for now that this is the case, and let $(\tilde{x}, \tilde{\xi}) \in N^*(C(\theta_1, r_2))$. Then again, we have by construction that $\text{supp } u(T, \cdot)$ is on one side of $C(\theta_1, r_2)$ at \tilde{x} and so $(\tilde{x}, \tilde{\xi}) \in \text{WF}_A(u(T, \cdot))$. It also follows as before that $u(T, \cdot)$ is zero in a neighborhood of the $C(\theta_1, r_2)$ mirror point of \tilde{x} . We then see again from Proposition 2.4 of [25] that $(\tilde{x}, \tilde{\xi}) \notin \text{WF}_A(u(T, \cdot))$, a contradiction. It follows again that $\text{supp } u(T, \cdot) \subset \bar{B}_{r_0}(\theta_0)$. That f is zero then follows from Tataru's unique continuation as in the small radius case.

Now we show the existence of the circle $C(\theta_1, r_2)$ with property that

$$C(\theta_1, r_2) \cap \text{supp } u(T, \cdot) = \{\tilde{x}\},$$

mentioned above. We let $C(\theta_0, r_1)$, and x, \tilde{x} be as above. We define the sets $C^-(\theta_0, r_1) = \{y \in C(\theta_0, r_1) \mid (y - \theta_0) \cdot \theta_0 \leq 0\}$, and $C^+(\theta_0, r_1) = \{y \in C(\theta_0, r_1) \mid (y - \theta_0) \cdot \theta_0 \geq 0\}$. It is clear that $B_1(0)$ is contained in the interior of the region bounded by $C^-(\theta_0, r_1) \cup L(\theta_0, r_1)$, where $L(\theta_0, r_1)$ is the diameter of $C(\theta_0, r_1)$ defined by the vector θ_0^\perp . We may assume without loss of generality that $x \in C^-(\theta_0, r_1)$, for if not, we may simply swap the roles of x and \tilde{x} in what follows. Now $x \in C^-(\theta_0, r_1) \implies \tilde{x} \in C^+(\theta_0, r_1)$, because x cannot be a $C(\theta_0, r_1)$ mirror point, as we have shown. The line $\ell(t)$ defined by

$$\ell(t) = \theta_0 + t(\tilde{x} - \theta_0)$$

intersects S^1 at 2 points: θ_0 and

$$\theta_1 = \theta_0 - \frac{2\theta_0 \cdot (\tilde{x} - \theta_0)}{r_1^2}(\tilde{x} - \theta_0).$$

This implies there are two distinct circles with centers on S^1 such that $(\tilde{x}, (\tilde{x} - \boldsymbol{\theta}_0))$ is in the conormal bundle to these circles, namely $C(\boldsymbol{\theta}_0, r_1)$ and $C(\boldsymbol{\theta}_1, r_2)$, where $r_2 = |\tilde{x} - \boldsymbol{\theta}_1|$. Note that

$$\begin{aligned} r_2 &= \left| \tilde{x} - \left(\boldsymbol{\theta}_0 - \frac{2(\tilde{x} - \boldsymbol{\theta}_0) \cdot \boldsymbol{\theta}_0}{r_1^2} (\tilde{x} - \boldsymbol{\theta}_0) \right) \right| \\ &= \left| (\tilde{x} - \boldsymbol{\theta}_0) \left(1 + \frac{2(\tilde{x} - \boldsymbol{\theta}_0) \cdot \boldsymbol{\theta}_0}{r_1^2} \right) \right| \\ &= r_1 \left| 1 + \frac{2(\tilde{x} - \boldsymbol{\theta}_0) \cdot \boldsymbol{\theta}_0}{r_1^2} \right| > r_1 \end{aligned}$$

where the last inequality follows because

$$\tilde{x} \in C^+(\boldsymbol{\theta}_0, r_1) \implies \frac{2(\tilde{x} - \boldsymbol{\theta}_0) \cdot \boldsymbol{\theta}_0}{r_1^2} > 0,$$

so that

$$1 + \frac{2(\tilde{x} - \boldsymbol{\theta}_0) \cdot \boldsymbol{\theta}_0}{r_1^2} > 1.$$

From this we see then that $r_2 = r_1 + \frac{2(\tilde{x} - \boldsymbol{\theta}_0) \cdot \boldsymbol{\theta}_0}{r_1}$. Now, we need only show that $C(\boldsymbol{\theta}_1, r_2) \cap \text{supp } u(T, \cdot) = \{\tilde{x}\}$. Clearly by construction, \tilde{x} is in this intersection. Also note that by the choice of r_1 , that $C(\boldsymbol{\theta}_0, r) \cap \text{supp } u(T, \cdot) = \emptyset$ for all $r > r_1$. So let $y \in C(\boldsymbol{\theta}_1, r_2)$. Then, we have using the triangle inequality

$$\begin{aligned} |y - \boldsymbol{\theta}_0| &\geq |y - \boldsymbol{\theta}_1| - |\boldsymbol{\theta}_1 - \boldsymbol{\theta}_0| \\ &= r_2 - \left| \frac{2(\tilde{x} - \boldsymbol{\theta}_0) \cdot \boldsymbol{\theta}_0}{r_1^2} (\tilde{x} - \boldsymbol{\theta}_0) \right| \\ &= r_1, \end{aligned}$$

so that $|y - \boldsymbol{\theta}_0| \geq r_1$, and equality holds only when $y - \boldsymbol{\theta}_0 = \alpha(\boldsymbol{\theta}_1 - \boldsymbol{\theta}_0)$ for some $\alpha > 0$, but this is only the case when $y = \tilde{x}$. So, we've shown that $y \in C(\boldsymbol{\theta}_1, r_2) \implies |y - \boldsymbol{\theta}_0| > r_1$ if $y \neq \tilde{x}$. In other words, $y \neq \tilde{x} \implies y \in C(\boldsymbol{\theta}_0, r)$ for some $r > r_1$, so that so that $y \notin \text{supp } u(T, \cdot)$, and in particular, $y \notin C(\boldsymbol{\theta}_1, r_2) \cap \text{supp } u(T, \cdot)$ if $y \neq \tilde{x}$. This completes the proof in the large radius case for full data.

2.4 Stability

It is natural to take $f \in H_D(\Omega) \subset H_0^1(\Omega)$ when taking conservation of energy into consideration. By the above theorems, in both the small and large radius cases, we have that $Mf(t, \theta)$ is an elliptic FIO of order $-1/2$. We will model finite time measurements in $[0, T]$ by premultiplying $Mf(t, \theta)$ by $\chi \in C_0^\infty(\mathbb{R})$ with $\text{supp } \chi \subset [-1, T_1]$ for $T < T_1 < \infty$, and $\chi \equiv 1$ on $[0, T]$. Now because M is an FIO of order $-1/2$ associated with the graph of the canonical relation C , we have M^* is also an FIO of order $-1/2$, and it is associated with the canonical relation C^{-1} . $M^*\chi M$ then is an elliptic pseudodifferential operator of order -1 . This implies that a parametrix B , which necessarily is an elliptic Ψ DO of order 1, exists such that

$$BM^*\chi M = \text{Id} - R,$$

where R is a regularizing operator. We may assume that B is a properly supported Ψ DO, which means $B, B^t : \mathcal{E}'(\Omega) \rightarrow \mathcal{E}'(\Omega)$. From this we see that

$$\|f\|_{H^1(\Omega)} \leq \|BM^*\chi Mf\|_{H^1(\Omega)} + \|Rf\|_{L^2(\Omega)}.$$

B is a continuous linear operator, so we have

$$\|f\|_{H^1(\Omega)} \leq C\|M^*\chi Mf\|_{H^2(\Omega)} + \|Rf\|_{L^2(\Omega)},$$

for some $C > 0$, independent of f . And lastly, M^* is a continuous linear operator, so we have from [14], Cor. 25.3.2.,

$$\|f\|_{H^1(\Omega)} \leq C'\|\chi Mf\|_{H^{3/2}([0, T] \times S^1)} + \|Rf\|_{L^2(\Omega)}.$$

Note that because we've multiplied $Mf(t, \theta)$ by χ and $Mf(t, \theta)$ has θ support in S^1 , which is a compact manifold, that $\chi Mf(t, \theta)$ has compact support in $(0, T) \times S^1$, and so the norm above in $H^{3/2}([0, T] \times S^1)$ is finite. By virtue of the injectivity of $\chi Mf(t, \theta)$, we may then write (at the cost of possibly increasing C')

$$\|f\|_{H^1(\Omega)} \leq C'\|\chi Mf\|_{H^{3/2}([0, T] \times S^1)}.$$

This gives stability of the measurement operator M .

Theorem 2.4.1 *Let $f \in H_D(\Omega)$, and $Mf(t, \theta)$ be defined as the either of the measurement operators above. If $\chi \in C_0^\infty(\mathbb{R})$ with $\chi \equiv 1$ on $[0, T]$, then we have the following stability estimate:*

$$\|f\|_{H^1(\Omega)} \leq C \|\chi Mf\|_{H^{3/2}([0, T] \times S^1)}.$$

2.4.1 Visible Singularities

A singularity $(y, \xi) \in \text{WF}(f)$ is called visible on an open subset $U \times \Gamma$ of $\mathbb{R} \times S^1$ for M if it creates a singularity in the measurement data $Mf|_{U \times \Gamma}$. Now because Mf is an elliptic FIO associated with a local canonical graph C (See Theorems 2.2.1, 2.2.2), we know by [14]

$$\text{WF}(Mf) = C \circ \text{WF}(f).$$

Let $(t_0, \boldsymbol{\theta}_0) \in \mathbb{R} \times S^1$ and let $U \times \Gamma$ be an open neighborhood of $(t_0, \boldsymbol{\theta}_0)$. By the above arguments (Theorems 1 and 2), we know that singularities $(y, \xi) \in \text{WF}(f)$ split and travel along geodesics $(\gamma_{y, \hat{\xi}}(t), c(y)|\xi|\dot{\gamma}_{y, \hat{\xi}}(t))$, and that this will create a singularity at $(t_0, \boldsymbol{\theta}_0)$ if and only if the geodesic intersects the circular integrating detector with center $\boldsymbol{\theta}_0$ perpendicularly at time t_0 , with no singularity to mask it intersecting the circular integrating detector at mirror points on the circle (i.e. an antipodal point in the small radius case, and a $C(\theta, r)$ mirror point in the large radius case). Therefore, to determine those singularities of f that are visible from $U \times \Gamma$, we simply trace all geodesics that go through $R\boldsymbol{\theta}$ back to Ω and see if they have nonempty intersection with $\text{WF}(f)$, see Figure 2.2.

For each $(t, \boldsymbol{\theta}) \in U \times \Gamma$, $\lambda \in \mathbb{R} \setminus 0$, let

$$A_{t, \boldsymbol{\theta}, \lambda}^+ = \left\{ \left(\gamma_{(x, \frac{x-R\boldsymbol{\theta}}{r})}(t), \lambda \hat{\gamma}_{(x, \frac{x-R\boldsymbol{\theta}}{r})}(t) \right) \mid |x - R\boldsymbol{\theta}| = r, (x - R\boldsymbol{\theta}) \cdot \boldsymbol{\theta} > 0 \right\}$$

and

$$A_{t, \boldsymbol{\theta}, \lambda}^- = \left\{ \left(\gamma_{(x, \frac{x-R\boldsymbol{\theta}}{r})}(t), \lambda \hat{\gamma}_{(x, \frac{x-R\boldsymbol{\theta}}{r})}(t) \right) \mid |x - R\boldsymbol{\theta}| = r, (x - R\boldsymbol{\theta}) \cdot \boldsymbol{\theta} < 0 \right\}.$$

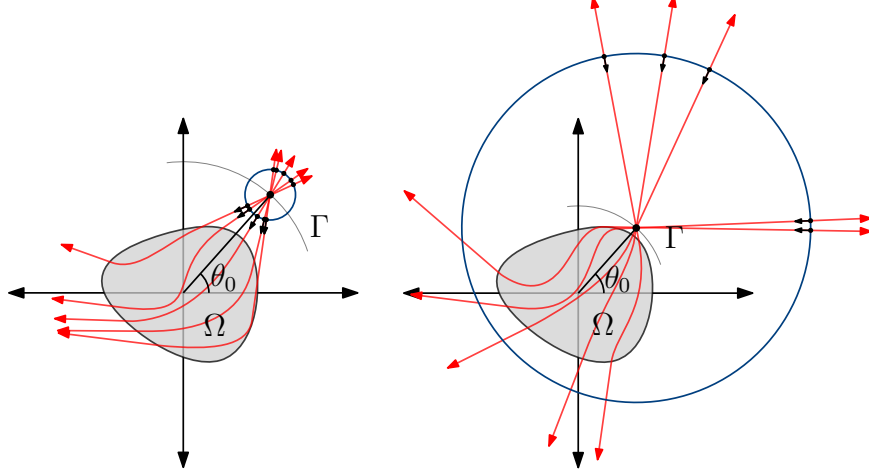


Figure 2.2. Singularities that may be visible from $\theta_0 \in \Gamma$ in both the cases (left) $R - r > 1$ and (right) $R = 1, r > 2$ will lie on the geodesics issued from the integrating detectors.

These are the sets of all points on geodesics intersecting the half circle $C^+(\theta, r)$ (respectively, $C^-(\theta, r)$) perpendicularly at time t , with tangent vector of magnitude λ . For

$$\left(\gamma_{(x, \frac{x-R\theta}{r})}(t), \lambda \hat{\gamma}_{(x, \frac{x-R\theta}{r})}(t) \right) \in A_{t,\theta,\lambda}^{\pm},$$

define

$$\sim \left(\gamma_{(x, \frac{x-R\theta}{r})}(t), \lambda \hat{\gamma}_{(x, \frac{x-R\theta}{r})}(t) \right) = \left(\gamma_{(\tilde{x}, \frac{\tilde{x}-R\theta}{r})}(t), \lambda \hat{\gamma}_{(\tilde{x}, \frac{\tilde{x}-R\theta}{r})}(t) \right) \in A_{t,\theta,\lambda}^{\mp},$$

where \tilde{x} is the appropriate mirror point on the circular integrating detector, depending on the experimental setup. Now, $(y, \xi) \in \text{WF}(f)$ is visible from $(t, \theta) \in U \times \Gamma$ if and only if $(y, \xi) \in A_{t,\theta,\lambda}^{\pm}$ for some $(t, \theta, \lambda) \in U \times \Gamma \times (\mathbb{R} \setminus 0)$ and $\sim (y, \xi) \notin \text{WF}(f)$. Let

$$B_{t,\theta,\lambda}^{\pm} = \left\{ (y, \xi) \mid (y, \xi) \in A_{t,\theta,\lambda}^{\pm} \cap \text{WF}(f) \text{ and } \sim (y, \xi) \notin \text{WF}(f) \right\}.$$

It then follows from the above arguments that the set of visible singularities is given by

$$\bigcup_{(t,\theta,\lambda) \in U \times \Gamma \times (\mathbb{R} \setminus 0)} B_{t,\theta,\lambda}^+ \cup B_{t,\theta,\lambda}^-.$$

We have shown the following:

Theorem 2.4.2 *Let $U \times \Gamma \subset \mathbb{R} \times S^1$ be an open subset, and for each $(t, \theta, \lambda) \in U \times \Gamma \times (\mathbb{R} \setminus 0)$ let $A_{t,\theta,\lambda}^\pm$ and $B_{t,\theta,\lambda}^\pm$ be defined as above. Then in both the small radius detector case and the large radius detector case, the singularities of f that are visible from $U \times \Gamma$ in the restricted data $Mf|_{U \times \Gamma}$ are given by*

$$\bigcup_{(t,\theta,\lambda) \in U \times \Gamma \times (\mathbb{R} \setminus 0)} B_{t,\theta,\lambda}^+ \cup B_{t,\theta,\lambda}^-.$$

From this we see that if $\Gamma = S^1$ and $(0, T] \subset U$, where

$$T = \sup_{x \in \Omega} \inf_{\theta \in [0, 2\pi)} \text{dist}(x, C(\theta, r)),$$

(where the distance is the geodesic distance), then all singularities of f are visible assuming $T < \infty$.

2.5 Numerical Results

To simulate the collection of forward data, we numerically solve the wave equation with variable wave speed using the implementation of Perfectly Matched Layers (PML) found in [8] for a number of different smooth initial conditions. This ensures that measured data will only come from signals inside the region of interest, and not from reflections at the boundary of the window of computation. Then, we collect simulated measurement data on the unit circle $Mf(t, \theta)$ for $0 \leq \theta < 2\pi$ and $0 \leq t < 5$, for a specific initial condition. In general, the amount of time that we collect data should depend on the wave speed inside the medium we are imaging, and for the wave speed we have chosen of $1 + 0.3 \sin(8x) \cos(5y)\eta(x, y)$ with $\eta(x, y) \in C_0^\infty(B_1(0))$, $t=5s$ suffices as an appropriate time range. We've shown the graph of the wave speed in Figure 2.3. We then use an iterative solver to reconstruct the smooth initial condition using the simulated data over the given time interval. The reconstruction shown in Figure 2.4 was made using the model $R = 1$ and $r = 2$ (the large radius detector model), with data taken on the full unit circle. An almost identical reconstruction is obtained if we use the small radius integrating detector model with full data.

We also run numerical simulations with data taken on an open subset of the unit circle. Here we take data for $\theta \in (-\pi/2, 0)$, with the same wave speed interior to the object. We then multiply by a smooth cutoff function so as to not introduce new singularities into the reconstruction. Results for the partial data case are shown in Figures 2.5 and 2.6.

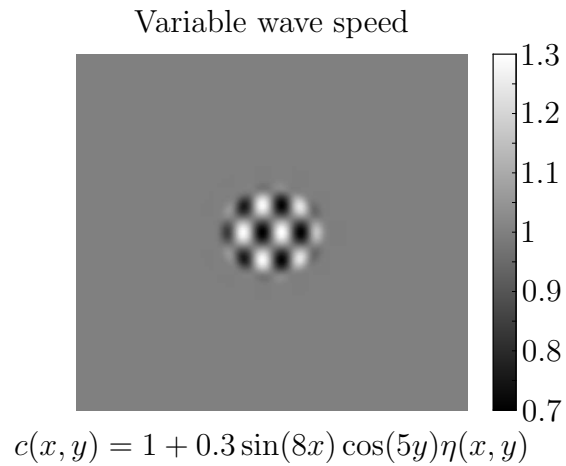


Figure 2.3. Variable wave speed of $1 + 0.3 \sin(8x) \cos(5y) \eta(x, y)$, where $\eta(x, y) \in C_0^\infty(B_1(0))$.

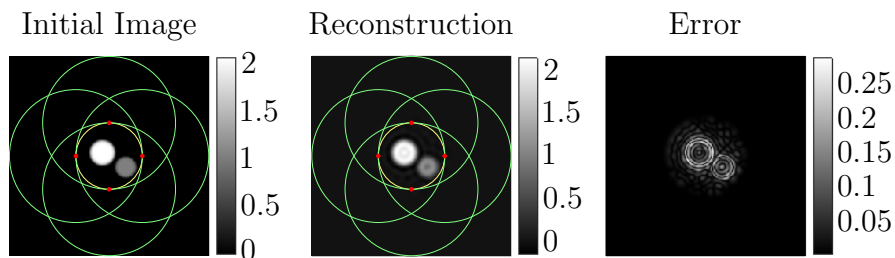


Figure 2.4. Results of reconstruction using $R = 1$ and $r = 2$ model (Large radius detector model). This reconstruction was made using full data.

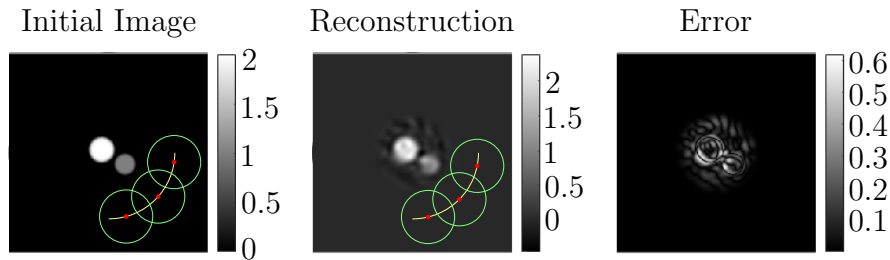


Figure 2.5. Result of reconstruction with partial data using $R = 2$, and $r = 0.8$ (Small radius detector model). This reconstruction was for $\theta \in (-\pi/2, 0)$. Shown in the figure are the set on which data is collected as well as some representative circular integrating detectors.

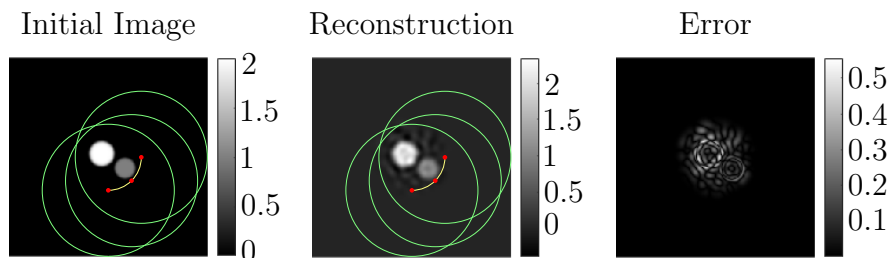


Figure 2.6. Result of reconstruction with partial data using $R = 1$, and $r = 2$ (Large radius detector model). This reconstruction was for $\theta \in (-\pi/2, 0)$. Shown in the figure are the set on which data is collected as well as some representative circular integrating detectors.

2.6 Conclusion and Future Work

We've shown in the 2D case that measured data

$$Mf(t, \theta) = \frac{1}{2\pi} \int_0^{2\pi} u(t, r \cos(\alpha) + R \cos(\theta), r \sin(\alpha) + R \sin(\theta)) d\alpha$$

can be used to reconstruct f uniquely, up to a smooth error. We showed this for partial data in the small radius detector case, and for full data in the large radius detector case. We've also shown stability of the measurement operator for both the large and small radius case and provided numerical evidence of these findings in both the large and small radius detector cases. In [36], the 3D case of circular integrating

detectors in a cylindrical stack (in both the large and small radius cases) is considered. Microlocally, this problem will be fundamentally different from the 2D analysis a few ways. For one, it is clear that not all microlocal singularities will be detected, even if the cylinder has infinite height and the wave speed is constant. This is because singularities leaving Ω vertically will never intersect a detector. Second, in the more practical case of a cylindrical stack of finite height, singularities may leave Ω that do not intersect the cylinder, even if they do not leave Ω vertically. These challenges will be addressed in further work.

3. Sampling in Thermoacoustic Tomography¹

3.1 Introduction

This work builds on the theory laid out in [27] on sampling Fourier Integral Operators (FIOs). We discuss the specific application of Thermoacoustic Tomography, in which case the measurement operator M is an FIO under suitable conditions. We discuss the theoretical resolution of f given the sampling rate of Mf and then discuss aliasing and averaged data. Lastly we will show empirical evidence of our findings using numerical simulations.

The experimental set up with regards to thermoacoustic tomography will be largely the same as in 2, with the exception that the measurement operator $M : C_0^\infty(\Omega) \rightarrow C_{(0)}^\infty((0, T) \times \Gamma)$ will simply be defined by

$$Mf(t, y) = u(t, y), (t, y) \in (0, T) \times \Gamma,$$

where $u(t, x)$ solves the acoustic wave equation (2.1). Note that the measurements are simply the solution to the wave equation at the boundary instead of the circular integrating detector set up from the previous chapter. We note that the space $C_{(0)}^\infty((0, T) \times \Gamma)$ is the space of smooth functions ϕ on $(0, T) \times \Gamma$ such that $\phi(t, y) = 0$ near $t = 0$.

¹This chapter has been submitted to appear in the Journal of Inverse and Ill-Posed Problems

3.1.1 M as an FIO

To obtain an oscillatory integral representation of M , we may use the geometric optics construction to solve for $u(t, x)$ in $(0, T) \times \mathbb{R}^n$ up to a smooth error (see [28, 32] for more details). This construction leads to the representation

$$u(t, x) = \frac{1}{(2\pi)^n} \sum_{\sigma=\pm} \int e^{i\phi_\sigma(t, x, \xi)} a_\sigma(t, x, \xi) \hat{f}(\xi) d\xi,$$

where ϕ_σ are solutions to the eikonal equation $(\partial_t \phi_\sigma)^2 = c^2(x) |\nabla_x \phi_\sigma|_{g_0}^2$ with initial conditions $\phi_\sigma(0, x, \xi) = x \cdot \xi$. Note that solutions to the eikonal equation are local in nature, and so this representation of $u(t, x)$ is only valid until some time T_1 . However, we may then solve (2.1) with “initial” conditions $\tilde{u}(0, x) = u(T_1, x)$ and $\partial_t \tilde{u}(t, x) |_{t=0} = \partial_t u(t, x) |_{t=T_1}$ using the same geometric optics construction. In this way, we can obtain an “approximate” solution to (2.1) for all (t, x) . Note by approximate, we mean up to a smooth error term. This error term could be quite large in the L^∞ sense, but because it is a smooth term, it is negligible in the calculus of FIOs. It can be shown that $M = M_+ + M_-$ is a sum of elliptic FIOs of order 0 associated with locally diffeomorphic canonical relations that are each (locally) one-to-one mappings (see i.e. [27, 28]). We record the canonical relations C_+ and C_- here for later use:

$$C_\pm : (x, \xi) \mapsto (s_\pm(x, \xi), \gamma_{x, \xi}(s_\pm(x, \xi)), \mp |\xi|_g, \dot{\gamma}'_{x, \xi}(s_\pm(x, \xi))). \quad (3.1)$$

Here, we have $s_\pm(x, \xi)$ is the exit time of the geodesic starting at x in the direction $\pm g^{-1}\xi$, $\gamma_{x, \xi}(t)$ is the point on the geodesic issued from (x, ξ) at time t and $\dot{\gamma}'_{x, \xi}(t)$ is the orthogonal (in the metric) projection of $\dot{\gamma}_{x, \xi}(t)$ onto $T\partial\Omega$ (the tangent bundle of the boundary of Ω , so implicitly, we assume that $\partial\Omega$ is at least a C^1 manifold). We assume that the metric induced by $g := c^{-2}(x)g_0$ is non trapping, so that $|s_\pm(x, \xi)| < \infty$ for all $(x, \xi) \in T^*\Omega$. Note that because each of the canonical relations C_+ and C_- are one-to-one, the full canonical relation of the FIO M given by $C = C_+ \cup C_-$ is one-to-two, which makes intuitive sense as singularities split and travel along geodesics according to propagation of singularities theory.

3.2 Preliminary definitions and theorems

3.2.1 Semiclassical analysis

The main definitions and theorems of semiclassical analysis and sampling that we use come from [27, 38]. For a more complete background on semiclassical analysis, see [38]. Also, for sampling theory relating the thermoacoustic tomography in the case of a constant speed, we refer the reader to [11]. In sampling the measurement operator Mf , we are interested in how the sampling rates affect our ability to resolve singularities with high frequency. To model this, we will rescale co-vectors ξ by a factor of $1/h$ where h is a small parameter. We then examine families of functions (or distributions) f_h that satisfy certain growth conditions as h becomes small. Because of this, instead of considering the classical wave front set of a distribution, we consider the semiclassical wave front set, denoted $\text{WF}_h(f)$. Note that f is understood here to be a family of functions f_h depending on the parameter h , but we will drop this subscript when it will not cause confusion. A key tool in analyzing the behavior of the measurement operator M will be the semiclassical Fourier Transform, defined below.

Definition 3.2.1 (Semiclassical Fourier Transform) *The semiclassical Fourier transform of an h -dependent family of distributions is defined as*

$$\mathcal{F}_h f_h(\xi) = \int e^{-ix \cdot \xi/h} f_h(x) dx.$$

If we denote the classical Fourier Transform by \mathcal{F} , then we have

$$\mathcal{F}_h f_h(\xi) = \mathcal{F} f_h \left(\frac{\xi}{h} \right).$$

Much like in classical analysis, we can use the semiclassical Fourier transform to define Sobolev norms on certain classes of functions or distributions.

Definition 3.2.2 (h -Tempered family of distributions) *The h -dependent family f_h of distributions in \mathcal{S}' is said to be h -tempered if*

$$\|f_h\|_{H_h^s}^2 := (2\pi h)^{-n} \int \langle \xi \rangle^{2s} |\mathcal{F}_h f_h(\xi)|^2 d\xi$$

is such that $\|f_h\|_{H_h^s} = O(h^{-N})$ for some s and N . Here, we have $\langle \xi \rangle = \sqrt{1 + |\xi|^2}$.

Another key tool we will use is the idea of the semiclassical wave front set of an h -dependent family of distributions.

Definition 3.2.3 (Semiclassical Wave Front Set) *The semiclassical wave front set $\text{WF}_h(f_h)$ of the h -tempered family f_h is defined to be the complement of the set of $(x_0, \xi_0) \in \mathbb{R}^{2n}$ such that there exists $\phi \in C_0^\infty(\mathbb{R}^n)$ with $\phi(x_0) \neq 0$ so that*

$$\mathcal{F}_h(\phi f_h) = O(h^\infty) \quad (\text{in } L^\infty)$$

for ξ in a neighborhood of ξ_0 .

This set plays a similar role as the classical wave front set from microlocal analysis, however in general there is no sort of inclusion between these two sets. As an example [38], the coherent state

$$f_h(x) = e^{-|x-x_0|^2/(2h)} e^{ix \cdot \xi_0/h},$$

has an empty wave front set in the classical sense, as it is a smooth function in both x and ξ , however its semiclassical wave front set is $\text{WF}_h(f_h) = \{(x_0, \xi_0)\}$. Note also that the zero section is allowed to be a part of the semiclassical wave front set, unlike in the classical case. Also, we do not require the semiclassical wave front set to be a conic set, which is another way that this set differs from the classical wave front set. We call elements of $\text{WF}_h(f_h)$ singularities.

Definition 3.2.4 (h - Ψ DO) *We will use the standard quantization to define semiclassical pseudodifferential operators. Fix m and $k \in \mathbb{R}$ and let $a(x, \xi) \in C^\infty(\mathbb{R}^{2n})$ satisfy the following: For every α and β multi-indices and every compact set $K \subset \mathbb{R}^n$ there exists some $C_{\alpha, \beta, K} > 0$ such that*

$$|D_x^\alpha D_\xi^\beta a(x, \xi)| \leq C_{\alpha, \beta, K} h^k \langle \xi \rangle^m$$

for all $x \in K$ and $\xi \in \mathbb{R}^n$. We then say $a(x, \xi)$ is a semiclassical symbol of order $\leq m$. Then we define the semiclassical pseudodifferential operator $a(x, hD)$ by

$$a(x, hD)f(x) := (2\pi h)^{-n} \iint_{\mathbb{R}^{2n}} e^{i(x-y) \cdot \xi/h} a(x, \xi) f(y) dy d\xi.$$

Definition 3.2.5 (Localization in phase space) *The h -tempered family f_h is said to be localized in phase space if for every $N \in \mathbb{N}$, there exists some $\psi \in C_0^\infty(\mathbb{R}^{2n})$ and some $h_0 > 0$ and $C_N > 0$, such that for $0 < h \leq h_0$*

$$\sup_{x \in \mathbb{R}^n} |x^\alpha \partial_x^\beta (Id - \psi(x, hD)) f_h| \leq C_N h^N$$

for all multi-indices α and β . In other words,

$$p_{\alpha, \beta}((Id - \phi(x, hD)) f_h) \leq C_N h^N$$

for every seminorm $p_{\alpha, \beta}$ on $\mathcal{S}(\mathbb{R}^n)$. We then say $(Id - \phi(x, hD)) f_h = O_{\mathcal{S}}(h^\infty)$.

Note that because the functions we work with are semiclassically band limited (see definition 3.2.7), that all functions we work with can be assumed to be localized in phase space unless otherwise stated.

Definition 3.2.6 (Semiclassical Frequency Set) *For each tempered h -dependent distribution f_h localized in phase space, set*

$$\Sigma_h(f_h) = \{\xi \mid (x, \xi) \in \text{WF}_h(f_h) \text{ for some } x \in \mathbb{R}^n\}.$$

This is simply the projection of $\text{WF}_h(f_h)$ onto the second variable.

Definition 3.2.7 (Semiclassically Band Limited Functions) *We say that $f_h \in C_0^\infty(\mathbb{R}^n)$ is semiclassically band limited (in \mathcal{B}) if*

1. $\text{supp } f_h$ is contained in an h -independent set,
2. f_h is tempered,
3. there exists a compact set $\mathcal{B} \subset \mathbb{R}^n$ such that for every open $U \supset \mathcal{B}$, we have for every N there exists C_N such that

$$|\mathcal{F}_h f_h(\xi)| \leq C_N h^N \langle \xi \rangle^{-N} \text{ for } \xi \notin U.$$

Semiclassically band limited functions are those functions that can be reconstructed up to a smooth error from their samples, much like the band limited functions are those that can be perfectly reconstructed from their samples in the classical Nyquist Sampling theorem given a small enough sampling rate [19].

3.2.2 Sampling

The main theorem used in [27] is the following:

Theorem 3.2.1 *Assume that $\Omega \subset \mathbb{R}^n$, $\mathcal{B} \subset \mathbb{R}^n$ are open and bounded. Let $f_h \in C_0^\infty(\Omega)$ satisfy*

$$\|(\text{Id} - \psi(x, hD))f_h\|_{H_h^m} = O(h^\infty)\|f_h\|_{H_h^m}, \quad \forall m \gg 0, \quad (3.2)$$

for some $\psi \in C_0^\infty(\mathbb{R}^{2n})$ such that $\text{supp}_\xi \psi \subset \mathcal{B}$. Let $\hat{\chi} \in L^\infty(\mathbb{R}^n)$ be such that $\text{supp } \hat{\chi} \subset \mathcal{B}$ and $\hat{\chi} = 1$ near $\text{supp}_\xi \psi$.

Assume that W is an invertible matrix so that the images of \mathcal{B} under the translations $\xi \mapsto \xi + 2\pi(W^*)^{-1}k$, $k \in \mathbb{Z}^n$, are mutually disjoint. Then for every $s \in (0, 1]$,

$$f_h(x) = |\det W| \sum_{k \in \mathbb{Z}^n} f_h(shWk) \chi\left(\frac{\pi}{sh}(x - shWk)\right) + O_{H_h^m}(h^\infty)\|f_h\|_{H_h^m}, \quad (3.3)$$

for every $m \geq 0$, and

$$\|f_h\|_{H_h^m}^2 = |\det W|(sh)^n \sum_{k \in \mathbb{Z}^n} |f_h(shWk)|^2 + O(h^\infty)\|f_h\|_{H_h^m}^2. \quad (3.4)$$

The proof of this theorem essentially follows from the classical Nyquist sampling theorem and can be found in [24, 27]. For all applications in this paper, we take the matrix W above to be the identity matrix.

We also make use of the following corollary, found in [27]:

Corollary 3.2.2 *Let f_h be semiclassically band limited with $\Sigma_h(f) \subset \prod(-B_j, B_j)$ for some $B_j > 0$. Let $\hat{\chi}_j \in L^\infty(\mathbb{R})$ be supported in $[-1, 1]^n$ and $\hat{\chi}_j(\xi_j/B_j) = \pi$ for $\xi \in \Sigma_h(f)$. If $0 < s_j \leq \pi/B_j$, then*

$$f_h(x) = \sum_{k \in \mathbb{Z}^n} f_h(s_1 h k_1, \dots, s_n h k_n) \prod_j \chi_j\left(\frac{\pi}{s_j h}(x - s_j h k)\right) + O_S(h^\infty).$$

The key take away of this corollary is that if $s_j \leq \pi/B_j$, then f_h will be accurately reconstructed from samples up to a small error. Finally, we make heavy use of the following theorem which relates how classical FIOs effect semiclassical wavefront sets from [27], where the reader can find the proof.

Theorem 3.2.3 *Let A be an FIO in the class $I^m(\mathbb{R}^{n_2}, \mathbb{R}^{n_1}, \Lambda)$ where $\Lambda \subset T^*(\mathbb{R}^{n_1} \times \mathbb{R}^{n_2}) \setminus 0$ is a Lagrangian manifold and $m \in \mathbb{R}$. Then for every f_h localized in phase space,*

$$\mathrm{WF}_h(Af) \setminus 0 \subset C \circ \mathrm{WF}_h(f) \setminus 0, \quad (3.5)$$

where $C = \Lambda'$ is the canonical relation of A .

This theorem shows how classical FIOs affect the semiclassical wavefront set away from the zero section. In particular, the semiclassical wavefront set of Af away from the zero section transforms in the same way the classical wavefront set does: it is transformed by the canonical relation associated with A . The main assertion in [27] is that the sampling requirements of Mf given $\mathrm{WF}(f)$ are determined by C , the canonical relation associated with Mf .

3.3 Resolution limit of f given sampling rate of Mf

Suppose we wish to sample the Mf at some fixed sampling rates s_t and s_{y^j} . Here we don't assume that we know any information about $\Sigma_h(f)$, we only wish to see how fixing a sampling rate on Mf affects our ability to resolve singularities of f . Avoiding aliasing of Mf is equivalent to (by Corollary 3.2.2)

$$(\tau, \eta) \in \Sigma_h(Mf) \implies |\tau| \leq \frac{\pi}{s_t}, \quad |\eta_j| \leq \frac{\pi}{s_{y^j}},$$

where τ is the dual variable to t , and η is the dual variable to y , with η_j the j th component of η . Note that the norms $|\tau|$ and $|\eta|$ are taken in the corresponding metric. In particular, $|\eta|$ is taken in the induced norm on the tangent space to the boundary, which we'll call $g_{0, \partial\Omega}$. We may use the canonical relation (3.1) C associated with M to write the inequalities above as

$$|\xi|_g = \sqrt{c^2 g_0^{ij} \xi_i \xi_j} \leq \frac{\pi}{s_t}, \quad |\dot{\gamma}'_{x, \xi}(s_{\pm}(x, \xi))_j|_{g_{0, \partial\Omega}} \leq \frac{\pi}{s_{y^j}}.$$

From this we can see that we have that avoiding aliasing is equivalent to

$$c(x)|\xi|_{g_0} \leq \frac{\pi}{s_t}, \quad |\dot{\gamma}'_{x, \xi}(s_{\pm}(x, \xi))_j|_{g_{0, \partial\Omega}} \leq \frac{\pi}{s_{y^j}} \quad (3.6)$$

For most of the paper, we will assume that g_0 is Euclidean, although more general results hold.

3.3.1 The effect of s_t on resolution

Consider the first inequality in (3.6) and assume that s_{y^j} is taken small enough so as to not effect resolution of singularities of f . The first inequality indicates that the sampling rate s_t imposes a limit on the resolution of f such that for fixed x , there will be higher resolution of singularities of f at points (x, ξ) where the wave speed $c(x)$ is slower, and likewise the resolution will be worse at those points (x, ξ) where the wave speed is faster. In particular, given the relative sampling rate s_t , we cannot resolve singularities at x with frequency greater than

$$|\xi| = \frac{\pi}{c(x)s_t}.$$

This is a local result. A global estimate for the maximum frequency of a singularity that is guaranteed to be resolved anywhere given the sampling rate s_t is given by

$$|\xi| = \frac{\pi}{c_{\max}s_t}. \quad (3.7)$$

This is illustrated in Figures 3.1 and 3.2 below.

A note on figures

All numerical examples before Figure 3.11 were constructed with an initial image on a 800×800 grid in a computational window representing the square $[-4, 4]^2$. This gives a value of $\Delta x = 8/800 = 0.01$ before any sort of undersampling occurs. Additionally, the initial image in most figures is composed of either sums of coherent

states, or simply cosine functions multiplied by a smooth cutoff function. The wave speed is taken to be one of the following:

$$\begin{aligned}
 c(x, y) &\equiv 1 && \text{(Constant speed case)} \\
 c(x, y) &= 1 - 0.5e^{-\frac{((x+1)^2+y^2)^2}{0.25}} && \text{(Slow speed case)} \\
 c(x, y) &= 1 + 0.5e^{-\frac{((x+1)^2+y^2)^2}{0.25}} && \text{(Fast speed case),}
 \end{aligned}$$

with the exception of Figure 3.3, where the speed is $c(x, y) = 1 + 0.5 \exp(-((x-1)^2 + (y+0.5)^2)/0.25)$. In the first and second cases, we take $\Delta t = \Delta x/\sqrt{2} \approx 0.0071$, which ensures when we solve the wave equation, the CFL condition is satisfied for the finite difference scheme we are using, which is the leap frog scheme, in combination with the PML scheme found in [8]. In the third case, we take $\Delta t = \Delta x/(1.5\sqrt{2}) \approx 0.00629$, again to make sure that the CFL condition is satisfied. We take $h = 0.02$ in Figures 3.1 through 3.10. Also in all of the images before Figure 3.11, the maximum (euclidean) length covector in the image is $|\xi| = 1$. We then solve the forward wave equation in these examples collecting data on the boundary of the square $[-2, 2]^2$ until $T = 6$ seconds in the constant and fast speed cases, and until $T = 12$ seconds in the slow speed case. The values of Δt and Δx have been chosen so that there is guaranteed to be no aliasing in the collected data before we simulate undersampling. We then simulate undersampling by taking every m^{th} sample either in the space or time variable, where m depends on the specific figure we look at and is specified in the caption of the image. After simulating undersampling in this way, we resize the image of the data to its original size using the `lanczos3` option in the `imresize` function of Matlab. We then use a time reversal reconstruction to arrive at our reconstructed image with aliasing. Depending on the particular image, we may calculate s_y and s_t explicitly, which then allows us to compute where the aliasing artifacts will be in the image by using the canonical relations. For example, in Figure 3.6, we undersample by taking every 6th time sample and then resize the image back to its original size. This gives $s_t \approx 4.7059$ and $\pi/s_t \approx 0.6676$. Using this, we can calculate where a pair

(x, ξ) will be mapped under the canonical relation associated with the measurement operator composed with the shift operator.

For Figures 3.11 through 3.15, photo credit for the zebra image used in these figures is given by: “Mountain Zebra (*Equus zebra*)” by berniedup is licensed under CC BY-SA 2.0. We first cropped the original image (which was 1023×616) to a size of 500×500 . We sample on a finer grid in these examples, 1200×1200 . From there we resized the image so that in our 1200×1200 grid, the image would lie in the square $[-1.9, 1.9]^2$. Lastly, we multiplied by a smooth cutoff function to smooth the edges of the image. This is to avoid aliasing artifacts that come from the image edge instead of the image itself when we collect and undersample data. We solve the wave equation using constant speed $c(x, y) = 1$, and collect data on the boundary of the square $[-2, 2]^2$ as in all other examples. We then simulate undersampling by taking either every 20th space sample or every 12th time sample, and then resize the image back to its original size, again using the `lanczos3` option in the `imresize` function of Matlab. In Figure 15, we then average the data in the space variable using a gaussian image filter to mitigate the effects of undersampling. We then use time reversal to arrive at an image reconstruction of the original image, having aliasing artifacts that are described by the theory in this paper.

3.3.2 The effect of s_{y^j} on resolution

Assume now that s_t is chosen small enough so as to not effect resolution of singularities of f . The second inequality in (3.6)

$$|\dot{\gamma}'_{x,\xi}(s_{\pm}(x, \xi))_j|_{g_0, \partial\Omega} \leq \frac{\pi}{s_{y^j}},$$

tells us that the sampling rate s_{y^j} imposes a limit on the resolution of f such that singularities (x, ξ) that intersect the boundary $\partial\Omega$ nearly perpendicularly will have higher resolution than those that hit the boundary nearly tangentially (at a large angle to the normal vector to $\partial\Omega$ at the point of intersection). Also, because $|\dot{\gamma}_{x,\xi}(t)|_g$ is constant along the geodesic $\gamma_{x,\xi}$, we know in particular that $|\dot{\gamma}'_{x,\xi}(s_{\pm}(x, \xi))_j|_{g_0, \partial\Omega} \leq$

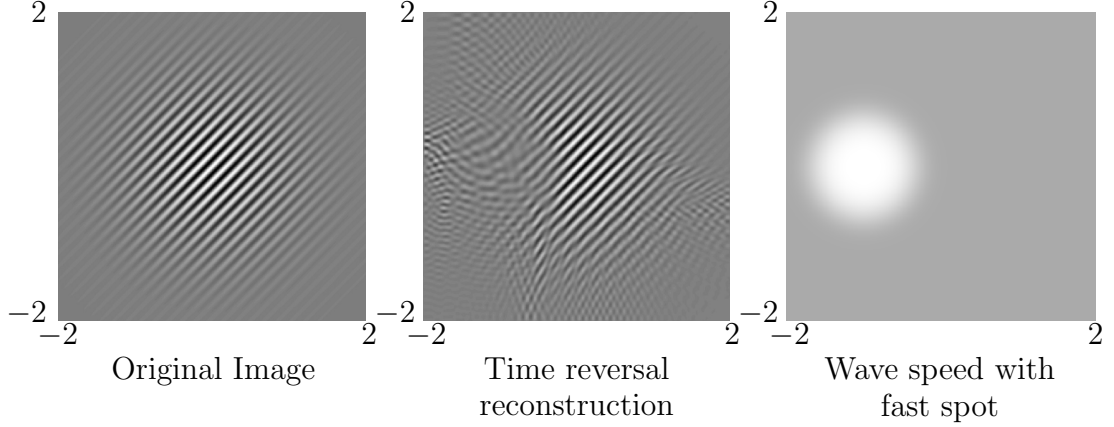


Figure 3.1. Resolution of f given a fixed sampling rate s_t of $Mf(t, y)$. The wave speed here $c(x, y) = 1 + 0.5 \exp(-((x + 1)^2 + y^2)^2/0.25)$ has a fast spot centered at $x = -1$. We can see that this is precisely where the reconstruction of f has poor resolution when under sampled in the t variable, as explained above. Undersampling is simulated by taking every 7th time sample, and then resizing the image of the data to its original size.

$|\dot{\gamma}'_{x,\xi}(s_{\pm}(x, \xi))|_{g_0, \partial\Omega} = |\xi|_g \cos(\theta)$ where θ is the angle (in the metric) between $\dot{\gamma}_{x,\xi}(s_{\pm}(x, \xi))$ and $\dot{\gamma}'_{x,\xi}(s_{\pm}(x, \xi))$. This tells us that to avoid aliasing, we must have

$$|\xi|_g \cos(\theta) \leq \frac{\pi}{s_{y^j}}.$$

We recall that $|\xi|_g^2 = c^2(x)g_0^{ij}\xi_i\xi_j$, and in the case that g_0 is Euclidean, we get

$$c(x)|\xi| \cos(\theta) \leq \frac{\pi}{s_{y^j}}.$$

For a fixed relative sampling rate s_{y^j} , we cannot resolve singularities (x, ξ) of f of frequency greater than

$$|\xi| = \frac{\pi}{s_{y^j} c(x) \cos(\theta)}.$$

Note in particular that if $\theta = \frac{\pi}{2}$ (i.e. the geodesic $\gamma_{x,\xi}$ hits the boundary $\partial\Omega$ perpendicularly), then $c(x)|\xi| \cos(\theta) = 0 < \pi/s_{y^j}$, and we will always be able to resolve the singularity at (x, ξ) . Also note that this is a local result, and as is the case for s_t “slow spots” in the speed $c(x)$ give better resolution of singularities in general.

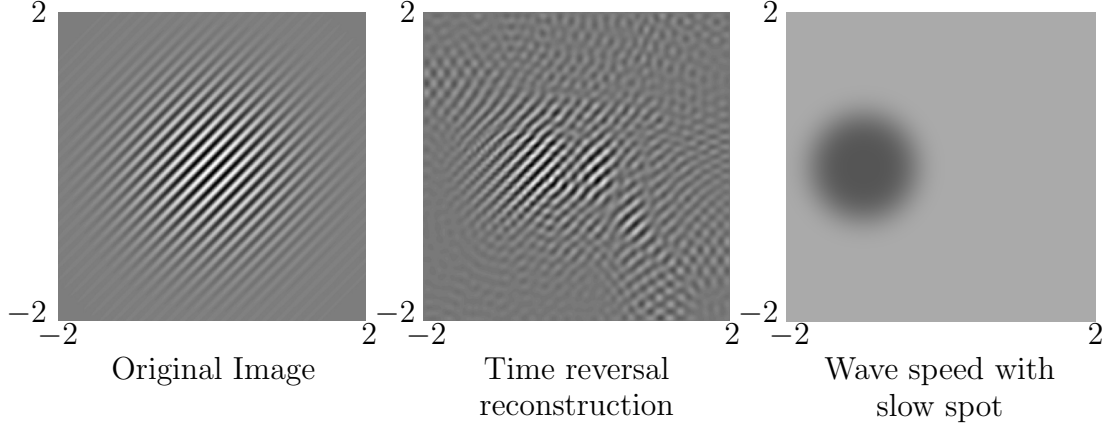


Figure 3.2. Resolution of f given a fixed sampling rate s_t of $Mf(t, y)$. The wave speed here $c(x, y) = 1 - 0.5 \exp(-((x + 1)^2 + y^2)^2/0.25)$ has a slow spot centered at $x = -1$. We can see that this is precisely where the reconstruction of f has the best resolution when under sampled in the t variable, as explained above. Undersampling is simulated by taking every 7th time sample.

Because $c(x) \leq c_{\max}$, we also get the following estimate for the maximum frequency of a resolvable singularity, regardless of location:

$$|\xi| = \frac{\pi}{c_{\max} s_{y^j} \cos(\theta)}.$$

Finally, because $0 < \theta \leq \pi/2$, we know $0 \leq \cos(\theta) < 1$, and we have the following (worst case) global estimate for the maximum frequency of a singularity of f that can be resolved:

$$|\xi| = \frac{\pi}{c_{\max} s_{y^j}}. \quad (3.8)$$

We note that if one wants to be able to resolve singularities of f with frequency K , then by considering (3.7) and (3.8), the sampling rates s_t and s_{y^j} of Mf should be taken to be at least

$$s_t = s_{y^j} \leq \frac{\pi}{K c_{\max}},$$

where c_{\max} is defined as before. In particular, we recover the result from [27] that for a semiclassically band limited f_h with essential maximum frequency B in the Euclidean case that we need to take sampling rates of Mf satisfying

$$s_t \leq \frac{\pi}{Bc_{\max}}, \quad s_{y^j} \leq \frac{\pi}{Bc_{\max}},$$

to avoid aliasing. These effects are shown in Figure 3.3.

3.3.3 CFL condition

We can relate this analysis to numerical solvers of the wave equation. When solving the wave equation numerically, a typical approach is to discretize the space and time domain, and use a finite difference scheme. Suppose we wish to simulate an experiment using a rectangular grid in the space coordinates and we collect data on the boundary of a square. Further, we assume that g_0 is Euclidean, and because the boundary is a rectangle, also the metric induced on the boundary is Euclidean. Suppose we have fixed each $s_{x^j} = \Delta x^j/h \leq \pi/(Bc_{\max})$ with a common value $s_x = \Delta x/h$, where B is the essential band limit on f , i.e. $\Sigma_h(f) \subset [-B, B]^n$. Note that by our choice of s_x , there will not be aliasing of Mf , provided s_t is chosen well, as on the boundary in this rectangular grid, we have $s_y = s_x$, where all of the s_{y^j} as above have a common fixed step size s_y . In order to choose s_t , we recall that the frequency set $\Sigma_h(Mf)$ is contained in the set $\{(\tau, \eta) \mid |\eta| \leq |\tau|\}$. Because f has a semiclassical band limit of B , we know that $\pi_2(\Sigma_h(Mf)) \subset \{|\eta| \leq \sqrt{n}Bc_{\max}\}$, where π_2 is the projection onto the second factor. We know this because each $|\eta_j| \leq Bc_{\max}$. Also, by the analysis above, we know that $|\tau| = |\xi|_g$, but $|\xi|_g \leq \max |\xi|_{c_{\max}}$. We also know that $\max |\xi| < \sqrt{n}B$, so that the largest possible size of $|\tau|$ given the band limit on f , is $\sqrt{n}Bc_{\max}$. It is then clear that we need $s_t \leq \pi/(\sqrt{n}Bc_{\max})$ to avoid aliasing. This tells us that we should take $\Delta t \leq \pi h/(\sqrt{n}Bc_{\max}) = \Delta x/\sqrt{n}$. Now, the CFL condition for the leapfrog finite difference scheme ([1, 4, 31]) tells us that given a step size Δx and wave speed $c(x)$, that we should take the time step $\Delta t \leq \Delta x/(\sqrt{n}c_{\max})$ to ensure stability of the finite difference scheme. But $\Delta x/(\sqrt{n}c_{\max}) \leq \Delta x/\sqrt{n}$, because

$c_{\max} \geq 1$. This means, that if we've chosen $\Delta x \leq \pi h / (B c_{\max})$, and we choose Δt satisfying the CFL condition for the leapfrog finite difference scheme, then there will be no aliasing in the measured data Mf at the boundary. Also, if $c_{\max} = 1$, then the CFL condition is identical to the conditions on Δx and Δt required to avoid aliasing of the measured data Mf . This only holds however when the CFL condition is as above, and this is not the case in all numerical schemes.

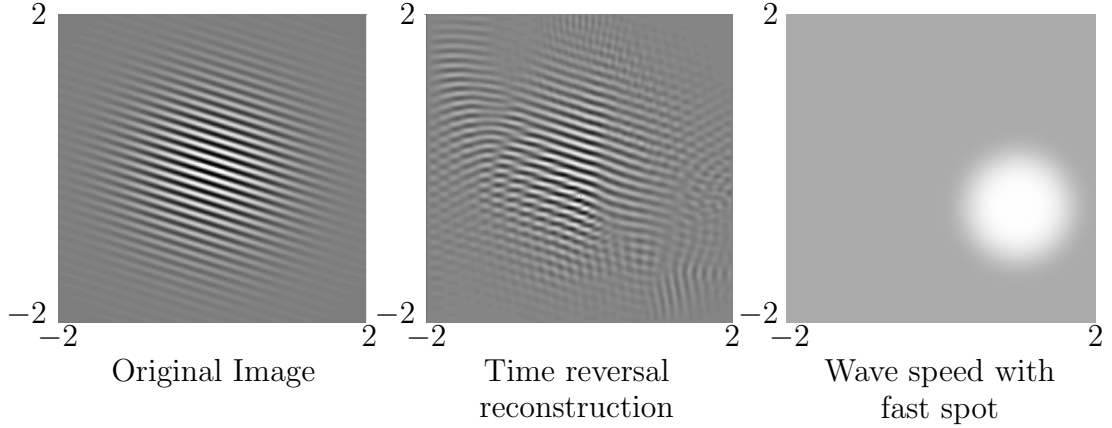


Figure 3.3. Resolution of f given a fixed sampling rate s_{y^j} of the space variables on the boundary $\partial\Omega$. We can see that the blurring effect is roughly uniform for points near the fast spot in the wave speed $c(x, y) = 1 + 0.5 \exp(-((x-1)^2 + (y+0.5)^2)/0.25)$, but that there are singularities in the region where $c \approx 1$ far from the fast spot that are also highly affected. These singularities hit the boundary with a larger angle to the outward pointing normal vector, and so we expect lower resolution there. Undersampling is simulated by taking every 12th space sample.

3.4 Aliasing and artifacts

Now suppose that we know that f_h is a semiclassically band limited function with essential band limit B , so that $\Sigma_h(f) \subset [-B, B]^n$. In order to avoid of Mf_h , as mentioned above, we need

$$c(x)|\xi|_{g_0} \leq \frac{\pi}{s_t} \quad |\dot{\gamma}'_{x,\xi}(s_{\pm}(x, \xi))_j|_{g_0, \partial\Omega} \leq \frac{\pi}{s_{y^j}}.$$

We know that $|\xi| \leq B$. We also saw above that $|\dot{\gamma}'_{x,\xi}(s_{\pm}(x,\xi))_j|_{g_0,\partial\Omega} \leq |\xi|_g \cos(\theta) \leq c(x)|\xi|_{g_0}$. Letting g_0 be Euclidean (again, more general results hold), so that $|\xi|_{g_0} = |\xi|$, we see that $c(x)|\xi| \leq c_{\max}B$, so, given the band limit B on $\Sigma_h(f)$, we are guaranteed to avoid aliasing if

$$s_t \leq \frac{\pi}{Bc_{\max}}, \quad s_{y^j} \leq \frac{\pi}{Bc_{\max}}.$$

3.4.1 Under sampling in t

Suppose that we have chosen s_t such that $s_t > \frac{\pi}{Bc_{\max}}$. Then, by [27] there will be aliasing of Mf . The error in the reconstruction can be modeled by the frequency shift operator

$$S_k : \tau \rightarrow \tau + \frac{2\pi k}{s_t}.$$

This operator is valid as long as $\tau + 2\pi k/s_t \in [-\pi/s_t, \pi/s_t]$ (see Figure 3.4 (right)).

If we have not under sampled Mf too critically in the t variable, we would expect to

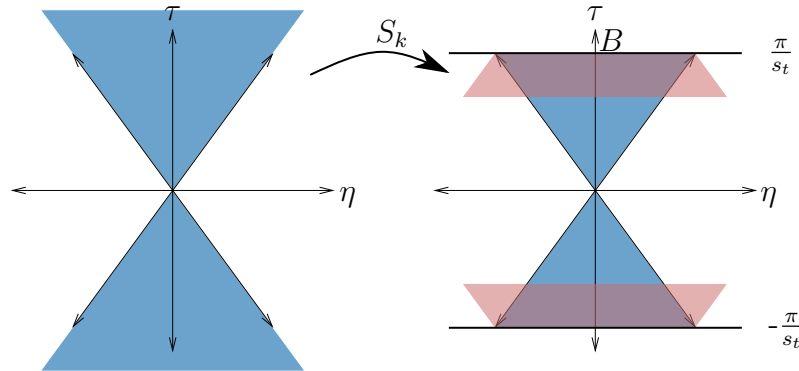


Figure 3.4. The characteristic cone in which $\Sigma_h(Mf)$ must lie. The cone on the left shows the possible range of the covector (η, τ) which is determined by the canonical relation associated with M . The image on the right shows the possible range of covectors (η, τ) after under sampling (in t). Note that the red regions have been shifted up and down from the original frequency set by translation due to under sampling.

only see this added error for $k = -1, 1$, with more terms added as the under sampling

becomes worse. As explained in [27], by Egorov's Theorem, we expect to see artifacts in a reconstruction of f that can be calculated by the canonical relation

$$C^{-1} \circ S_k \circ C : (x, \xi) \rightarrow (\tilde{x}, \tilde{\xi}),$$

where \tilde{x} and $\tilde{\xi}$ can be calculated by finding the operator on the left, and $C = C_+ \cup C_-$ as in (3.1). Note that because

$$C_{\pm}(x, \xi) = (s_{\pm}(x, \xi), \gamma_{x,\xi}(s_{\pm}(x, \xi)), \mp|\xi|_g, |\dot{\gamma}'_{x,\xi}(s_{\pm}(x, \xi))|),$$

that the sign of $\tau = \mp|\xi|_g$ plays an important role when we apply the inverse canonical transformation. We now calculate $C^{-1} \circ S_k \circ C$ for C_+ (We just write C^{-1} instead of C_+^{-1} , as the inverse canonical relation that we apply will depend on the sign of $-|\xi|_g + 2\pi k/s_t$):

$$\begin{aligned} C^{-1} \circ S_k \circ C_+(x, \xi) &= C^{-1} \circ S_k(s_+(x, \xi), \gamma_{x,\xi}(s_+(x, \xi)), -|\xi|_g, \dot{\gamma}'_{x,\xi}(s_+(x, \xi))) \\ &= C^{-1}(s_+(x, \xi), \gamma_{x,\xi}(s_+(x, \xi)), -|\xi|_g + \frac{2\pi k}{s_t}, \dot{\gamma}'_{x,\xi}(s_+(x, \xi))) \\ &= (\gamma_{y,-\zeta}(s_+(x, \xi)), -\dot{\gamma}_{y,-\zeta}(s_+(x, \xi))), \end{aligned}$$

where $y = \gamma_{x,\xi}(s_+(x, \xi))$ is the point of intersection of the geodesic issued from (x, ξ) with $\partial\Omega$, and $\zeta = \dot{\gamma}'_{x,\xi}(s_+(x, \xi)) + \beta_k \eta^{\perp}$ where $\beta_k = \pm \sqrt{(|\xi|_g - 2\pi k/s_t)^2 - |\dot{\gamma}'_{x,\xi}(s_+(x, \xi))|^2}$, where we choose the sign of β_k that matches the sign of $|\xi|_g - 2\pi k/s_t$, and

$$\eta^{\perp} = \frac{\dot{\gamma}_{x,\xi}(s_+(x, \xi)) - \dot{\gamma}'_{x,\xi}(s_+(x, \xi))}{|\dot{\gamma}_{x,\xi}(s_+(x, \xi)) - \dot{\gamma}'_{x,\xi}(s_+(x, \xi))|}.$$

Aliasing artifacts are found using this mapping in Figures 3.5 and 3.6 below. The mapping $C^{-1} \circ S_k \circ C_-$ is calculated in almost an identical fashion, however we have a change in sign in the τ variable.

We include a more complicated image reconstruction in Figure 3.12 along with the collected data in Figure 3.13.

3.4.2 Under sampling in y

Now suppose that we have under sampled the y variable, i.e. we have chosen $s_{y^j} > \frac{\pi}{B_{c_{\max}}}$ for some $j = 1, \dots, n$. Then again, we will have aliasing and the error in

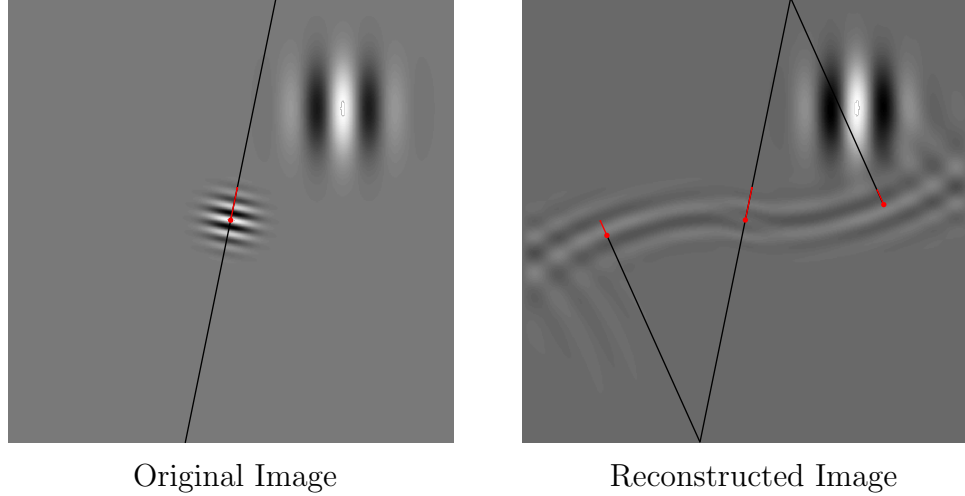


Figure 3.5. Tracing the aliasing artifacts by using geodesics. We have used the constant wave speed $c \equiv 1$ for this example. Here we have under sampled in t and show the image of the singularity (x, ξ) under the canonical relations given by $C_{\pm}^{-1} \circ S_1 \circ C_{\pm}$. Note that the low frequency singularity does not cause artifact, but the high frequency singularity vanishes in the reconstruction and causes aliasing artifacts. Undersampling is simulated by taking every 12th time sample.

the reconstruction will involve the frequency shift operator, but now S_k will act on η_j as

$$S_k : \eta_j \mapsto \eta_j + \frac{2\pi k}{s_{y^j}}.$$

This operator is valid as long as $\eta_j + \frac{2\pi k}{s_{y^j}} \in [-\pi/s_{y^j}, \pi/s_{y^j}]$. The canonical relation of the h -FIO (see [20] or [9] for details and definitions regarding h -FIOs) that operates on Mf as a reconstruction of f will then be given by (again, we only consider C_+ here)

$$C_+^{-1} \circ S_k \circ C_+(x, \xi) = C_+^{-1}(s_+(x, \xi), \gamma_{x, \xi}(s_+(x, \xi)), -|\xi|_g, \gamma'_{x, \xi}(s_+(x, \xi)) + \frac{2\pi k}{s_{y^j}} \mathbf{e}_j),$$

where \mathbf{e}_j is the unit vector in the y^j direction. Note that because the shift operator here does not affect the sign of $\tau = -|\xi|_g$, that we would not expect to see artifacts coming from the “mixed” canonical relations $C_{\mp}^{-1} \circ S_k \circ C_{\pm}$, as we do in the previous

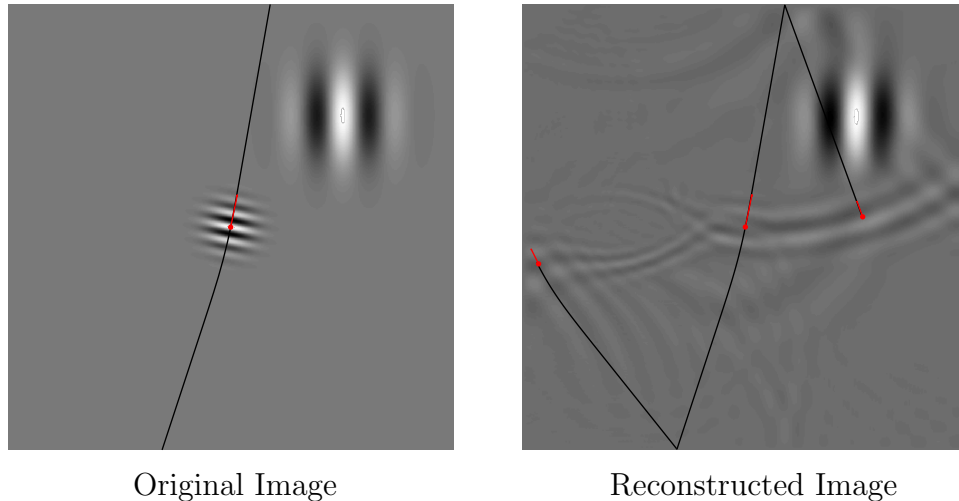


Figure 3.6. Artifacts in a reconstructed image with Mf under sampled in time variable and a variable wave speed of $c(x, y) = 1 - 0.5 \exp(-\frac{((x+1)^2+y^2)^2}{0.25})$. We trace the geodesics to find the image of (x, ξ) under the map $C_{\pm} \circ S_k \circ C_{\pm}$ as explained above. Undersampling is simulated by taking every 12th time sample.

case of undersampling in the time variable. Also note that, in particular, the form of $C_+^{-1} \circ S_k \circ C_+$ implies that the artifacts will have the same frequency as that of the original image, but perhaps with a space shift. Also, because this operator is valid as long as $\eta_j + 2\pi k/s_{y^j} \in [-\pi/s_{y^j}, \pi/s_{y^j}]$, if the geodesic emanating from (x, ξ) hits the boundary $\partial\Omega$ perpendicularly, then the point (x, ξ) will be unaffected by this shift in the reconstruction, i.e. there will be no artifacts that come from (x, ξ) . This is true because if the geodesic emanating from (x, ξ) hits $\partial\Omega$ perpendicularly, then $\eta_j = 0$ and $2\pi k/s_{y^j} \notin [-\pi/s_{y^j}, \pi/s_{y^j}]$ for any $k \neq 0$. Finding these artifacts in practice follows in much the same way as finding where artifacts occur for under sampling in the time variable. We illustrate this for the constant speed, Euclidean case in Figure 3.7 and see Figure 3.8 for the variable speed case.

We again include a more complicated image reconstruction in Figure 3.14 along with the collected data in Figure 3.15.

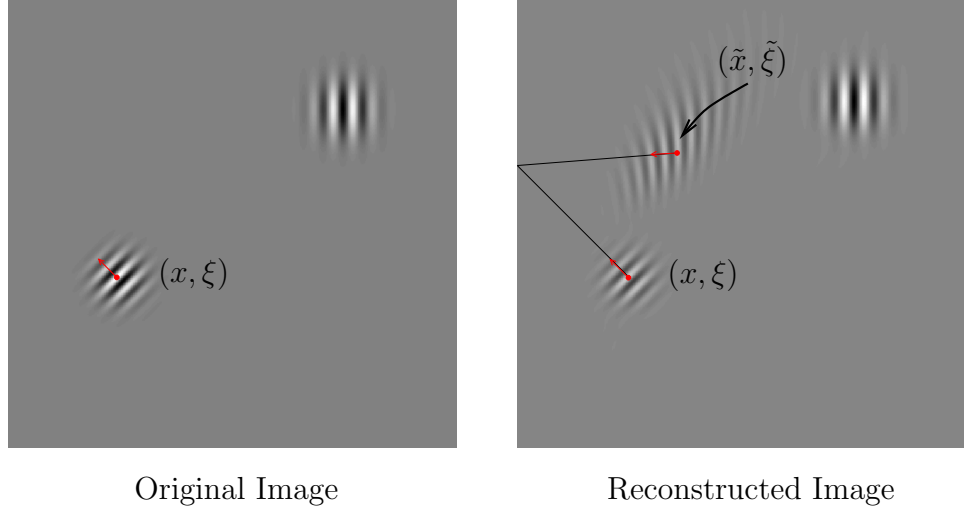


Figure 3.7. Artifacts in a reconstructed image with Mf under sampled in space variables. Here we take $c \equiv 1$. Specifically, Mf here was under sampled on the left and right edges of the square. We simulate undersampling by taking every 15th space sample. Note that there is no artifact in the reconstructed image coming from the pattern in the upper right corner of the square, because singularities from this pattern hit the boundary of the square perpendicularly. Note also that the original singularity still remains with half its amplitude because we did not under sample along the bottom edge of the square.

3.5 Averaged data

Suppose that the collected data $Mf(t, y)$ has been averaged in the t or y variables for some reason (in practice this can be done to try to avoid aliasing, or in an attempt to reduce the noise in data). This can be modeled in a few ways, including taking a convolution $\phi_h * Mf$ with a smooth function $\phi_h = h^n \phi(\cdot/h)$ that decreases away from the origin to 0. To model localized averaging however, we will consider data of the form $Q_h Mf(t, y)$, where Q_h is an h - Ψ DO with a principal symbol of the form $q_0(t, y, \tau, \eta) = \psi(a|\tau|^2 + b|\eta|^2)$ where $\psi \in C_0^\infty(\mathbb{R})$ is decreasing. The effect of Q_h is to limit $\text{WF}_h(Mf)$, which will in principle remove the high frequency singularities of Mf which will have a smoothing effect. From [27], we know that because M is a FIO

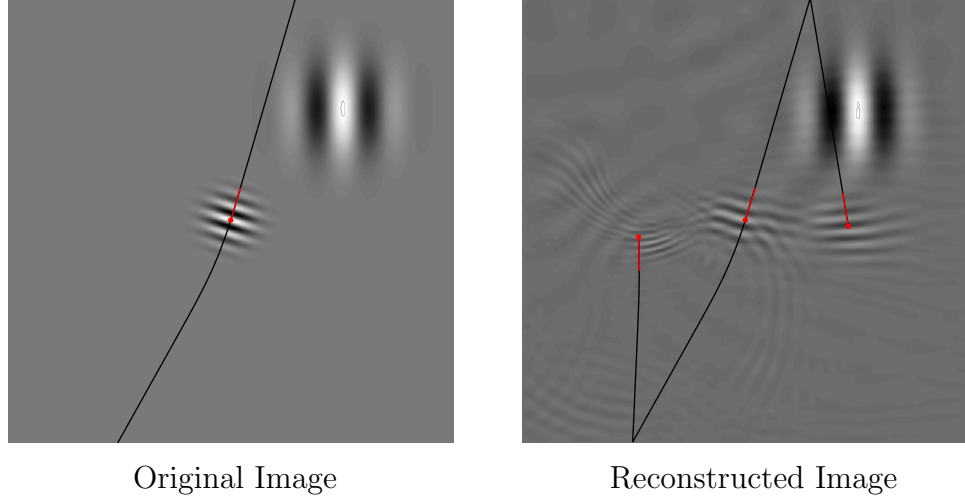


Figure 3.8. Artifacts in a reconstructed image with Mf under sampled in space variables and a variable wave speed of $c(x, y) = 1 - 0.5 \exp(-\frac{((x+1)^2+y^2)^2}{0.25})$. Specifically, Mf here was under sampled on the top and bottom edges of the square. The artifacts in the reconstruction have the same frequency as the original, but with a space shift due to under sampling. We simulate heavy undersampling by taking only every 30th space sample.

associated with the canonical map $C = C_+ \cup C_-$, that the composition $Q_h Mf$ can be written

$$Q_h Mf = MP_h f + O(h^\infty) f,$$

where P_h is a h - Ψ DO with principal symbol $p_0 = q_0 \circ C$ where q_0 is the principal symbol of Q_h . So, for Q_h, q_0 , we may calculate

$$\begin{aligned} p_0(x, \xi) &= \frac{1}{2} (q_0 \circ C_+(x, \xi) + q_0 \circ C_-(x, \xi)) \\ &= \frac{1}{2} \left(\psi(a|\xi|_g^2 + b|\dot{\gamma}'_{x,\xi}(s_+(x, \xi))|_{g_0, \partial\Omega}^2) + \psi(a|\xi|_g^2 + b|\dot{\gamma}'_{x,\xi}(s_-(x, \xi))|_{g_0, \partial\Omega}^2) \right). \end{aligned}$$

Suppose we only average the time data in $Mf(t, y)$. This corresponds to taking $b = 0$ above to give $p_0(x, \xi) = \psi(a|\xi|_g^2)$. This symbol takes its minimum values where $|\xi|_g^2 = c^2(x)g_0^{ij}\xi_i\xi_j$ is maximized. Assuming for a moment that g_0 is Euclidean, this means that we expect more blurring at points (x, ξ) where the wave speed is “fast”.

Additionally, we expect singularities (x, ξ) with large frequencies $|\xi|$ to be blurred more than smaller frequencies where the wave speed is the same. These effects can both be seen in Figure 3.9.

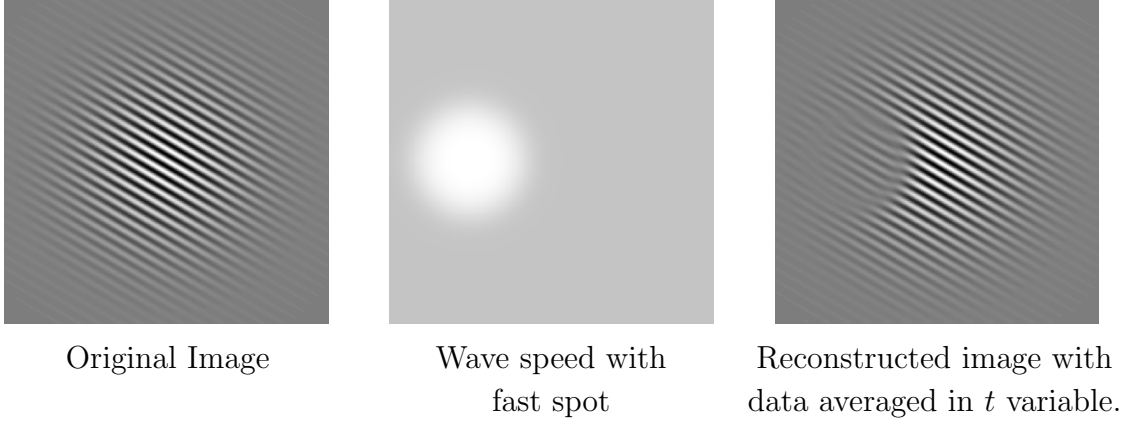


Figure 3.9. Reconstructed image from data that has been averaged in time variable by applying a 1D gaussian image filter to the t data. We can see that the reconstructed image is most blurred at the points where the speed $c(x)$ is fast, and there is less blurring where $c(x) = 1$.

Suppose now that we only average data in the spatial variable y . This corresponds to taking $a = 0$ above and we get the principle symbol of p_0 to be

$$p_0(x, \xi) = \frac{1}{2} (\psi(b|\dot{\gamma}'_{x,\xi}(s_+(x, \xi))|^2) + \psi(b|\dot{\gamma}'_{x,\xi}(s_-(x, \xi))|^2)).$$

Here the norm is the induced norm on the boundary, which we have noted in this paper as $g_{0,\partial\Omega}$. This symbol takes its smallest values when $|\dot{\gamma}'_{x,\xi}(s_{\pm}(x, \xi))|^2$ is large, i.e. when the geodesic issued from (x, ξ) intersects the boundary $\partial\Omega$ at a large angle. In addition, we expect singularities that hit the boundary $\partial\Omega$ perpendicularly to be affected far less by averaging of data in the y variable. In addition, because $|\dot{\gamma}'_{x,\xi}(s_{\pm}(x, \xi))|^2 = |\xi|_g^2 \cos^2(\theta_{\pm})$ where θ_{\pm} is the angle between $\dot{\gamma}'_{x,\xi}(s_{\pm}(x, \xi))$ and $\dot{\gamma}_{x,\xi}(s_{\pm}(x, \xi))$ we expect to see more blurring at points with faster speeds or higher frequency. For constant speeds c , the effect of averaging data in t is uniform in Ω , but the effect is local for averaging in y , due to the blurring depending on the angle

of intersection made by geodesics. In addition, with a variable speed singularities in “slow spots” of c will have higher resolution when blurring $Mf(t, y)$ in the y -data, but their resolution will still depend on how geodesics hit the boundary. The result is a roughly uniform blurring in fast spots of c , and local blurring elsewhere in the image depending on the geometry determined by $c^{-2}g_0$. This can be seen in Figure 3.10 below.

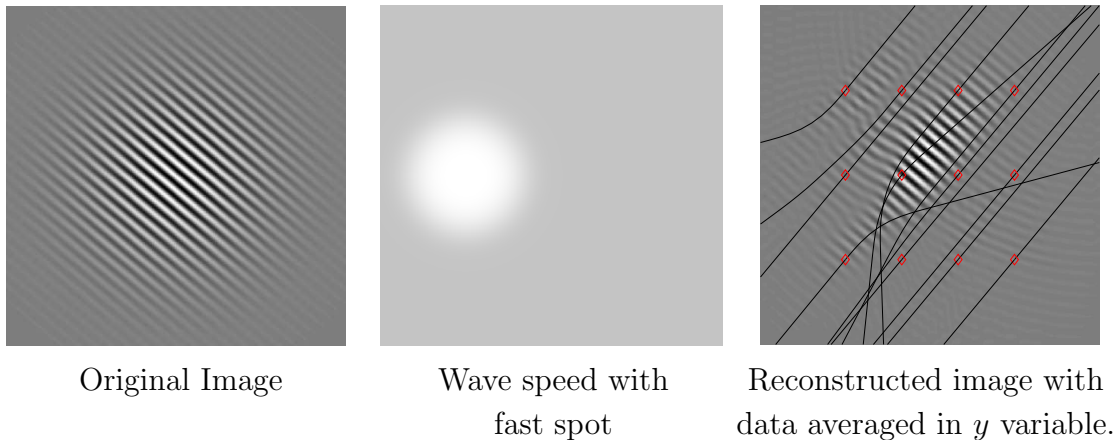


Figure 3.10. Reconstructed image from data that has been averaged in space variable by applying a 1D gaussian image filter to the y data. We can see from the drawn in geodesics, that singularities that hit the boundary at a larger angle to the normal vector to the boundary are blurred more in the reconstructed image after averaging the collected data. Meanwhile, those singularities that hit the boundary nearly perpendicularly are largely unaffected by the averaging of the data, at least on one side.

3.6 Anti-aliasing

We can use the above discussion to propose an anti-aliasing scheme. Averaging the measured data $Mf(t, y)$ in the space variable can be accomplished in practice in many ways, whether by using small averaging detectors, or by vibrating the boundary $\partial\Omega$ where we are taking pointwise measurements. We know then that this can be modeled by applying the h - Ψ DO Q_h to Mf where is as in the previous section. This

then allows us to say that $Q_h Mf(t, y) = MP_h f(t, y) + O(h^\infty)f$. In other words, by averaging the data in y , we measure $P_h f(x, \xi)$, where P_h is an h - Ψ DO with principle symbol $p_0(x, \xi) = q_0 \circ C(x, \xi)$ and C is the canonical relation of M , plus some error term with low order frequencies. We then expect that if we average $Mf(t, y)$ in the y variable before sampling, this should remove some of the shifting aliasing artifacts that appear when $Mf(t, y)$ has been under sampled in y , perhaps at the cost of some loss of resolution. See Figure 3.11 for an example of this anti-aliasing scheme in action.

As a final note, we point out that under sampling in the time variable t can cause data in $\mathcal{F}(Mf)$ to shift outside of the characteristic cone, and from this, one should be able to recover some high frequency singularities from data $Mf(t, y)$ under sampled in t by shifting these singularities back out into the characteristic cone where they necessarily originated (see Figure 3.4). However, we can only recover a small fraction of the high frequency singularities in this way uniquely in special cases, and in general we cannot recover the singularities without adding high frequency artifacts to the reconstructed image.

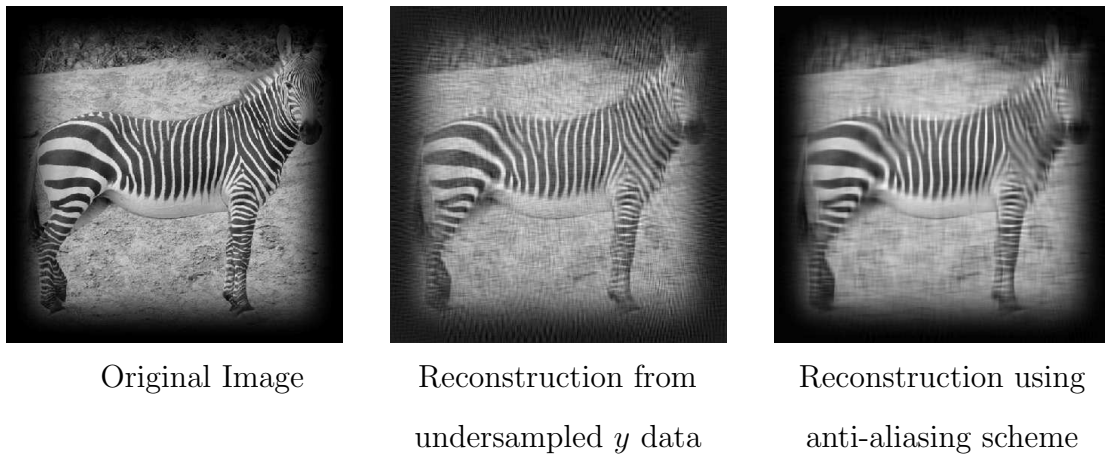


Figure 3.11. Example showing anti-aliasing scheme in which we first average the data $Mf(t, y)$ in the y variable and then sample this blurred version given by $Q_h Mf(t, y)$ in the above notation. We can see that some of the aliasing artifacts have been removed at the cost of some loss of resolution.

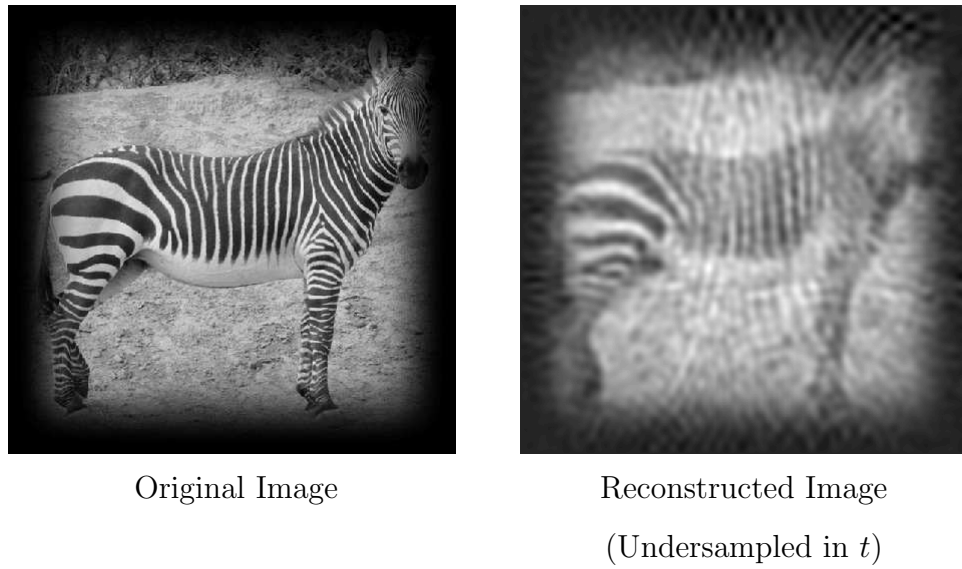


Figure 3.12. Image of a zebra along with reconstruction from under sampled (in t) data. The wave speed here is constant. High frequencies are lost due to this under sampling and the result is a heavily blurred image with aliasing artifacts.

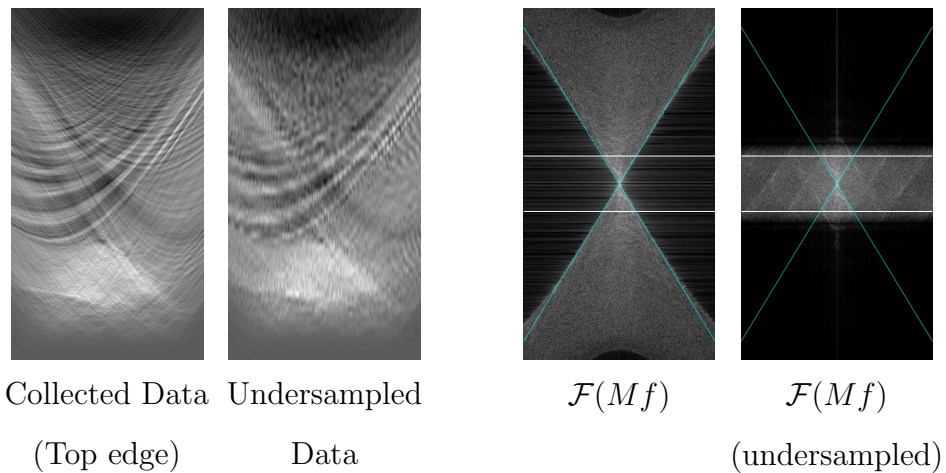


Figure 3.13. Collected data and under sampled data in t along with the associated Fourier transform data for the zebra image above. Note that the high frequencies in $\mathcal{F}(Mf)$ have been shifted so that they are approximately in the band $-\pi/s_t < \tau < \pi/s_t$, which is what results in the blurring in the reconstruction.

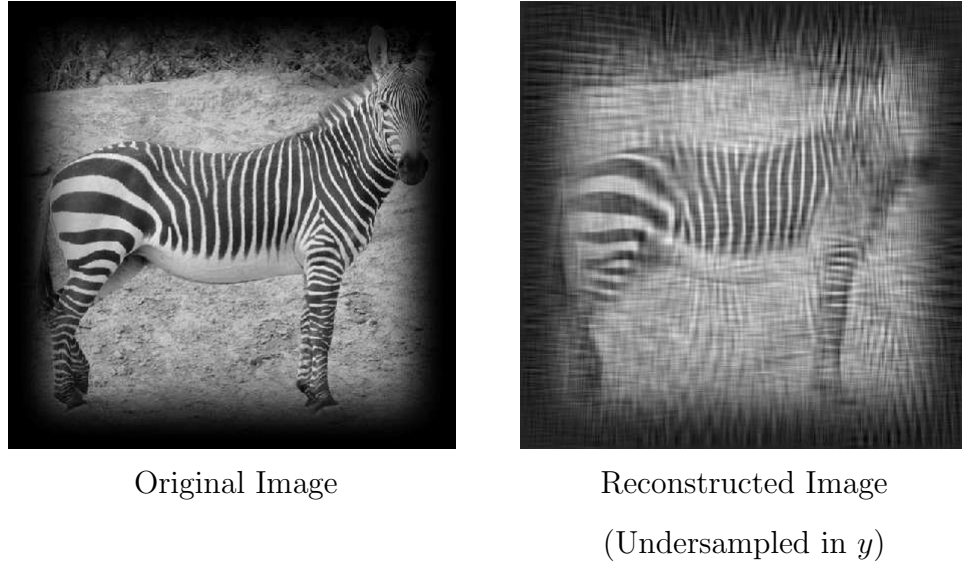


Figure 3.14. Image of a zebra along with reconstruction from under sampled (in y) data. The wave speed here is constant. Note that the singularities that hit the boundary of the square nearly perpendicularly are preserved, but there are also a lot of high frequency artifacts in the reconstructed image.

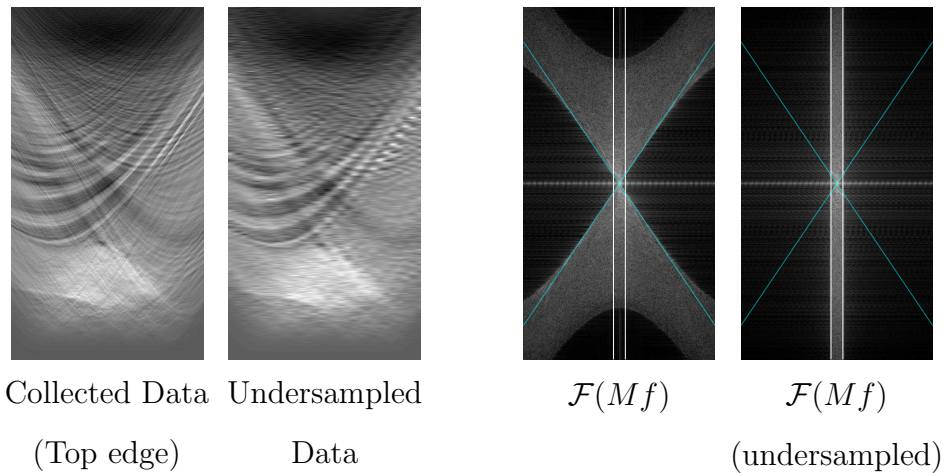


Figure 3.15. Collected data and under sampled data in y along with the associated Fourier transform data for the zebra image above. Under sampling has resulted in the shifting of frequencies in $\mathcal{F}(Mf)$ so that $-\pi/s_{y^j} < \eta < \pi/s_{y^j}$. This moves high frequencies but does not destroy them, which is what causes the high frequency artifacts in the reconstructed image above.

4. Non-uniqueness in the region of interest problem for the Radon transform

4.1 Introduction

The Radon transform is a classical integral transform that takes a function $f \in \mathcal{S}(\mathbb{R}^n)$ and maps it to integrals over all $n - 1$ dimensional hyperplanes in \mathbb{R}^n . This transform was first studied by Johann Radon in 1917 in his paper [26]. It has since then been used extensively in the applied sciences especially in medical imaging [5,22]. We can see one of these uses in the case of X-ray imaging, which uses a special instance of the Radon transform. In the case that we want to recover the X-ray attenuation $f(x) \in \mathcal{S}(\mathbb{R}^2)$ in some object, we have, by definition, X-rays travelling a small distance Δx at x suffer an intensity loss of

$$\frac{\Delta I}{I} = -f(x)\Delta x.$$

From this, it's clear that if we send X-rays through this object with an initial intensity I_0 and measure the resulting intensity I_1 (which depends on the direction that the rays are sent) on the other side of the object, we would obtain

$$\begin{aligned} \int_{I_0}^{I_1(L)} \frac{dI}{I} &= - \int_L f(x) ds \\ \Rightarrow \frac{I_1(L)}{I_0} &= \exp \left(- \int_L f(x) ds \right) \end{aligned}$$

where L is the line along which the X-rays travel. From this it's clear that the measurements involved are directly related to the Radon transform (which coincides with the X-ray transform in $n = 2$ dimensions). Recovery of $f(x)$ given the measurements $I_1(L)$ then is motivation for studying the inverse Radon (and X-ray) transform. We

are interested in determining when we can recover a local reconstruction of some function f given information only about the hyperplanes that intersect some neighborhood containing the support of f . This is the so called interior problem for the Radon transform. It is of interest in medical imaging for instance, where one may wish to obtain an image of only some region of interest inside the patient. Is it sufficient to only know the Radon transform for hyperplanes intersecting the region of interest to obtain an image of that region? We will show that in even dimensions, this is not the case, but in odd dimensions, it is indeed sufficient to obtain an image of the region of interest.

4.2 Background and definitions

4.2.1 Special functions

We will make use of a few special functions in what follows. Specifically, we will use spherical harmonics and Gegenbauer polynomials. References for both of these special functions can be found in Chapter 7 of [22].

Spherical Harmonics

Let P_l be the space of all polynomials on \mathbb{R}^n , homogeneous of degree l . That is, if $p \in P_l$, then for any $\lambda \in \mathbb{R}$, we have

$$p(\lambda x) = \lambda^l p(x).$$

Polynomials $p \in P_l$ must have the form

$$p(x) = \sum_{|\alpha|=l} c_\alpha x^\alpha,$$

where α is a multiindex. We then let $A_l \subset P_l$ be the subspace of P_l consisting of polynomials that are homogeneous of order l that are also harmonic. Recall that a

function f is called harmonic if $\Delta f = 0$, where Δ is the usual Laplacian operator on \mathbb{R}^n defined by

$$\Delta f = \sum_{j=1}^n \partial_j^2 f.$$

For $n = 1$, the only homogeneous, harmonic polynomials are $p_0(x) \equiv C$, where C is a constant, and $p_1(x) = mx$, where m is constant. For $n = 2$, the spaces A_l ($l \neq 0$) can always be spanned by 2 linearly independent functions, namely $p_{l,1}(x, y) = r^l \cos(l\theta)$ and $p_{l,2}(x, y) = r^l \sin(l\theta)$ where $x = r \cos(\theta)$ and $y = r \sin(\theta)$. That these are indeed polynomials in x and y can be seen by using trigonometric identities or basic complex analysis. In higher dimensions, there are even more homogeneous harmonic polynomials of degree l . Let H_l then be the space of functions defined on S^{n-1} that are obtained by those functions in A_l by restricting x to the unit sphere. That is,

$$H_l = \{\phi \mid \phi = p|_{S^{n-1}} \text{ where } p \in A_l\}.$$

A function in H_l will be called a surface harmonic. It's clear that H_l is a vector space over \mathbb{C} . The dimension of H_l is given by [30]

$$N(n, l) = \binom{n+l-1}{n-1} - \binom{n+l-3}{n-1}.$$

Further, H_l can be made into a Hilbert space with the usual inner product on S^{n-1} ,

$$\langle f, g \rangle = \int_{S^{n-1}} f \bar{g} d\omega.$$

So then, because we know that we can find $N(n, l)$ linearly independent surface harmonics in H_l , by the Gram-Schmidt orthogonalization procedure, we may say that

$$H_l = \text{span}\{Y_{l,k}\}_{k=1}^{N(n,l)},$$

where $\langle Y_{l,k}, Y_{l,k'} \rangle = 0$ for $k \neq k'$. By construction, $Y_{l,k}$ are eigenfunctions for the operator $\Delta_{S^{n-1}}$, the Laplacian on the unit sphere. Because of this, we also have $\langle Y_{l,k}, Y_{l',k'} \rangle = 0$ for $l \neq l'$. These $Y_{l,k}$ will be called spherical harmonics of degree l and order k .

Gegenbauer polynomials

The other special functions we use are the Gegenbauer polynomials, denoted by $C_l^{(n-2)/2}(x)$. This is the normalized Gegenbauer polynomial of degree l . In general, the Gegenbauer polynomials C_l^λ , ($\lambda > -1/2$) are defined in such a way as to be orthogonal with respect to the inner product

$$\langle f, g \rangle = \int_{-1}^1 f(x)g(x)(1-x^2)^{\lambda-1/2} dx.$$

They are normalized by requiring $C_l^\lambda(1) = 1$ (this is not a standard normalization, and is specific to [22]). Some specific cases of Gegenbauer polynomials are Chebyshev polynomials of the first kind ($\lambda = 0$), which are denoted $T_l(x)$, Chebyshev polynomials of the second kind ($\lambda = 1$), which are denoted $U_l(x)$ and Legendre polynomials ($\lambda = 1/2$), which are denoted $P_l(x)$.

Calculation of these polynomials may be accomplished by the following recurrence relations [6, Table 18.9.1] (for $\lambda \neq 0$ and $\lambda > -1/2$):

$$\begin{aligned} C_0^\lambda(x) &= 1 \\ C_1^\lambda(x) &= 2\lambda x \\ C_l^\lambda(x) &= \frac{1}{l} (2x(l + \lambda - 1)C_{l-1}^\lambda(x) - (l + 2\lambda - 2)C_{l-2}^\lambda(x)). \end{aligned}$$

From these recurrence relations, we can see that $C_l^\lambda(x)$ is a polynomial of degree l in x . It can also be shown from these relations that if l is even, then $C_l^\lambda(x)$ is an even function of x , and if l is odd, then $C_l^\lambda(x)$ is an odd function of x . Note also that these recurrence relation give the standard normalization of $C_l^\lambda(1) = (2\lambda)_n/n!$ [6, Table 18.6.1], where $(x)_n$ is the Pochhammer symbol

$$(x)_n = x(x+1)(x+2) \cdots (x+n-1),$$

and $(x)_0 = 1$ by definition. So to get the normalization of $C_l^\lambda(x)$ that we desire, we may simply use the above relations and then divide each $C_l^\lambda(x)$ by $(2\lambda)_l/l!$ to give $C_l^\lambda(1) = 1$. As mentioned above, the special case $\lambda = 0$ gives rise to the Chebyshev

polynomials of the first kind $T_l(x)$, which may be defined by the following functional equation for $|x| \leq 1$:

$$T_l(x) = \cos(l \arccos x).$$

In other words, the Chebyshev polynomials of the first kind satisfy the equation

$$T_l(\cos(x)) = \cos(lx).$$

For $|x| > 1$, we may take the alternate definition

$$T_l(\cosh(x)) = \cosh(lx).$$

4.2.2 The Radon transform

As mentioned in the introduction, the Radon transform is a transform that takes a function $f \in \mathcal{S}(\mathbb{R}^n)$ to its integrals over $n - 1$ dimensional hyperplanes:

Definition 4.2.1 (Radon transform) For $f \in \mathcal{S}(\mathbb{R}^n)$, the Radon transform R is defined as

$$Rf(\omega, p) = \int_{x \cdot \omega = p} f(x) dS$$

where dS is the Lebesgue surface measure on \mathbb{R}^n . Here, $\omega \in S^{n-1}$ and $p \in \mathbb{R}$.

Note that because $x \cdot \omega = p \iff x \cdot (-\omega) = -p$, it must be the case that $Rf(-\omega, -p) = Rf(\omega, p)$. The classical inversion formula for the Radon transform is proved in [22] and given below

Theorem 4.2.1 (Inversion of Radon transform) Let $f \in \mathcal{S}(\mathbb{R}^n)$ and $g = Rf$. Then, letting I^α be the operator defined by

$$\widehat{(I^\alpha f)} = |\xi|^{-\alpha} \hat{f}(\xi),$$

and letting $R^\#$ be the dual transform of the Radon transform defined by

$$R^\#(g)(x) = \int_{S^{n-1}} g(\theta, x \cdot \theta) d\theta,$$

then we have for any $\alpha < n$

$$f = \frac{1}{2(2\pi)^{n-1}} I^{-\alpha} R^{\#} I^{\alpha-n+1} g.$$

In particular, letting $\alpha = n - 1$, we obtain the inversion formula

$$f = \frac{1}{2(2\pi)^{n-1}} I^{1-n} R^{\#} g.$$

The operator I^{1-n} is simply another way of writing $(-\Delta)^{(n-1)/2}$, which is a local operator when n is odd, but non local when n is even. In [2,3], Cormack showed that if we expand $f(x, y)$ in a Fourier series (letting $r = |(x, y)|$ and $\theta = \arg(x + iy)$):

$$f(x, y) = \sum_{l=-\infty}^{\infty} f_l(r) e^{il\theta}, \quad (4.1)$$

and also expand $g(\omega, p) = Rf(\omega, p)$ in a Fourier series:

$$g(\omega, p) = \sum_{l=-\infty}^{\infty} g_l(p) e^{il\omega}, \quad (4.2)$$

then the Radon transform is a diagonal operator. That is, f_l only depends on g_l , and vice versa. The relations between the two are given by the following theorem

Theorem 4.2.2 (Cormack, 1963,1964) *Let $f \in \mathcal{S}(\mathbb{R}^2)$ and $g = Rf$. Letting $r = |(x, y)|$ and $\theta = \arg x + iy$, and expanding f and g as in (4.1) and (4.2) respectively, then we have the following relations:*

$$f_l(r) = -\frac{1}{\pi} \frac{d}{dr} \int_r^{\infty} \frac{r g_l(s) T_l(s/r) ds}{(s^2 - r^2)^{1/2} s},$$

$$g_l(p) = 2 \int_p^{\infty} \frac{f_l(s) T_l(p/s) s ds}{(s^2 - p^2)^{1/2}}.$$

This is generalized in [22]

Theorem 4.2.3 *Let $f \in \mathcal{S}(\mathbb{R}^n)$ and expand $f(x)$ as*

$$f(x) = \sum_{l=0}^{\infty} \sum_{k=1}^{N(n,l)} f_{l,k}(|x|) Y_{l,k}(x/|x|).$$

Further, let $g = Rf$ and expand $g(\omega, p)$ as

$$g(\omega, p) = \sum_{l=0}^{\infty} \sum_{k=1}^{N(n,l)} g_{l,k}(p) Y_{l,k}(\omega).$$

Then we have

$$f_{l,k}(r) = c(n) r^{2-n} \int_r^{\infty} (s^2 - r^2)^{(n-3)/2} C_l^{(n-2)/2} \left(\frac{s}{r} \right) g_{l,k}^{(n-1)}(s) ds, \quad (4.3)$$

$$g_{l,k}(p) = |S^{n-2}| \int_p^{\infty} C_l^{(n-2)/2} \left(\frac{p}{r} \right) \left(1 - \frac{p^2}{r^2} \right)^{(n-3)/2} f_{l,k}(r) r^{n-2} dr. \quad (4.4)$$

where

$$c(n) = \frac{(-1)^{n-1} \Gamma((n-2)/2)}{2\pi^{n/2} \Gamma(n-2)},$$

$\Gamma(z)$ is the usual Gamma function, and for $n = 2$, we take the limit

$$\lim_{n \rightarrow 2^+} c(n) = -1/\pi.$$

We will use these formulas to construct examples of nonuniqueness in the interior problem for the Radon transform.

The Radon transform is closely related to the X-ray transform, and in $n = 2$ dimensions they coincide.

Definition 4.2.2 (X-ray transform) For $f \in \mathcal{S}(\mathbb{R}^n)$, the X-ray transform X is defined as

$$Xf(\ell) = \int_{x \in \ell} f(x) ds$$

where ℓ is any line in \mathbb{R}^n .

This chapter will primarily be concerned with the Radon transform, but the results for the X-ray transform will be similar. As mentioned above, the Radon transform appears in applications such as medical imaging in which we wish to reconstruct an image of the interior of a patient given projections obtained by exposing the patient to X-rays, for instance [5]. These projections are simply the surface integral (line integral in this case) of the density function f representing the absorption coefficient of the cells of the patient.

In [12], it is shown that the Radon transform maps

$$\mathcal{S}(\mathbb{R}^n) \rightarrow \mathcal{S}_H(\mathbb{P}^n),$$

bijectionally, where

$$\mathcal{S}_H(\mathbb{P}^n) = \left\{ \phi \in \mathcal{S}(\mathbb{P}^n) \mid \int_{\mathbb{R}} p^m \phi(\omega, p) dp \text{ is a homogeneous poly-} \right. \\ \left. \text{nomial of order } m \text{ in } \omega. \right\},$$

and

$$\mathcal{S}(P^n) = \{ \phi \in \mathcal{S}(S^{n-1} \times \mathbb{R}) \mid \phi(-\omega, -p) = \phi(\omega, p) \},$$

and finally

$$\mathcal{S}(S^{n-1} \times \mathbb{R}) = \\ \left\{ \phi \in C^\infty(S^{n-1} \times \mathbb{R}) \mid \sup \left| (1 + |p|^k) \frac{d^l}{dp^l} (D\phi)(\omega, p) \right| < \infty, \forall l, k \in \mathbb{Z}^+ \right\}.$$

In other words, given $g \in \mathcal{S}_H(\mathbb{P}^n)$, there is a unique $f \in \mathcal{S}(\mathbb{R}^n)$ such that $g = Rf$. The proof of this is nontrivial, and we will use this result to prove the main result of this chapter. In practice, the condition that $\mu_m(Rf)$ be a homogeneous polynomial of order m in ω can be tricky to work with, and so we will characterize the range of the Radon transform in a more practically applicable way.

4.3 Main Results

Theorem 4.3.1 *Let $g(\omega, p) \in \mathcal{S}(S^{n-1} \times \mathbb{R})$. Further, let*

$$g(\omega, p) = \sum_{l=0}^{\infty} \sum_{k=1}^{N(n,l)} g_{l,k}(p) Y_{l,k}(\omega)$$

be the spherical harmonics expansion of g , where $Y_{l,k}(\omega)$ is the k^{th} basis spherical harmonic in H_l . Then we have $g = Rf$ for some unique $f \in \mathcal{S}(\mathbb{R}^n)$ if and only if

1. *For every $l \in \mathbb{Z}^+$, we have*

$$g_{l,k}(-p) = (-1)^l g_{l,k}(p)$$

for each $k = 1, 2, \dots, N(n, l)$, and

2. For every $l \in \mathbb{Z}^+$, we have

$$\mu_m g_{l,k} = \int_{-\infty}^{\infty} p^m g_{l,k}(p) dp = 0$$

for $0 \leq m < l$ and each $k = 1, 2, \dots, N(n, l)$.

Proof (\Leftarrow) If condition 1 holds, then because each $Y_{l,k}(\omega) = \sum_{|\alpha|=l} c_{\alpha,k} \omega^\alpha$, it's clear that

$$\begin{aligned} g(-\omega, -p) &= \sum_{l=0}^{\infty} \sum_{k=1}^{N(n,l)} g_{l,k}(-p) Y_{l,k}(-\omega) \\ &= \sum_{l=0}^{\infty} \sum_{k=1}^{N(n,l)} (-1)^l g_{l,k}(p) (-1)^l Y_{l,k}(\omega) = g(\omega, p), \end{aligned}$$

so that g is an even function of (ω, p) as is required for g to be in the range of the Radon transform. Next we need to show that $\mu_m g(\omega, p)$ is a homogeneous polynomial in ω of order m restricted to the unit sphere. By condition 2, and the fact that the spherical harmonics expansion converges uniformly to $g(\omega, p)$ [16], we have

$$\mu_m g = \sum_{l=0}^{\infty} \sum_{k=1}^{N(n,l)} \mu_m g_{l,k} Y_{l,k}(\omega) = \sum_{l=0}^m \sum_{k=1}^{N(n,l)} \mu_m g_{l,k} Y_{l,k}(\omega)$$

Assume for the moment that m is even. Then $\mu_m g_{l,k} = 0$ for every odd l , so the above sum becomes

$$\mu_m g = \sum_{j=0}^{m/2} \sum_{k=1}^{N(n,l)} \mu_m g_{2j,k} Y_{2j,k}(\omega).$$

We are interested in this when $|\omega| = 1$, so we write this sum adding factors of $|\omega|^2$ to see this as

$$\mu_m g = \sum_{l=0}^{m/2} \sum_{k=1}^{N(n,l)} \mu_m g_{2j,k} Y_{2j,k}(\omega) |\omega|^{2(m/2-j)}$$

And because $m/2$ is an integer, each term above is still a homogeneous polynomial in ω , and it's easy to see that the order of each term now is m , so that $\mu_m g$ is indeed a homogeneous polynomial of order m .

Assume now that m is odd. Then $\mu_m g_{l,k} = 0$ for l even, so we see that

$$\mu_m g = \sum_{j=0}^{(m+1)/2} \sum_{k=1}^{N(n,l)} \mu_m g_{2j-1,k} Y_{2j-1,k}(\omega).$$

Using the same idea as in the m even case, we'll rewrite this as (remembering $|\omega| = 1$)

$$\mu_m g = \sum_{j=0}^{(m+1)/2} \sum_{k=1}^{N(n,l)} \mu_m g_{2j-1,k} Y_{2j-1,k}(\omega) |\omega|^{2((m+1)/2-j)}.$$

Written this way, each term in the sum is clearly a homogeneous polynomial of order m , and so $\mu_m g$ is a homogeneous polynomial of order m in ω restricted to S^{n-1} . This then shows that conditions 1 and 2 imply that $g \in \mathcal{S}_H(\mathbb{P}^n)$ and therefore $g = Rf$ for some $f \in \mathcal{S}(\mathbb{R}^n)$.

(\Rightarrow) If $g(\omega, p) = Rf$ for some $f \in \mathcal{S}(\mathbb{R}^n)$, then $g \in \mathcal{S}_H(S^{n-1} \times \mathbb{R})$, i.e. $g(\omega, p)$ is even in (ω, p) and for each $m \geq 0$,

$$\mu_m g = \int_{-\infty}^{\infty} p^m g(\omega, p) dp$$

is a homogeneous polynomial of order m in ω restricted to the unit sphere. Note that it is a fact [30] that a homogeneous polynomial of order m , call it $P(x)$, may be written uniquely as

$$P(x) = P_m(x) + |x|^2 P_{m-2}(x) + \dots + \begin{cases} |x|^m P_0(x) & m \text{ even,} \\ |x|^{m-1} P_1(x) & m \text{ odd,} \end{cases}$$

where each $P_j(x)$ is a homogeneous polynomial of order j that is harmonic. These polynomials when restricted to the S^{n-1} are surface harmonics, and so they can be written as finite sums of spherical harmonics, say $P_{m-2k} = \sum_{j=0}^{N(n,m-2k)} \alpha_{m-2k,j} Y_{m-2k,j}$. Assume for now that m is even. Then

$$\begin{aligned} \mu_m g &= P_m(\omega) + |\omega|^2 P_{m-2}(\omega) + \dots + |\omega|^m P_0(\omega) \\ &= P_m(\omega) + P_{m-2}(\omega) + \dots + P_0(\omega) \\ &= \sum_{j=0}^{N(n,m)} \alpha_{m,j} Y_{m,j}(\omega) + \sum_{j=0}^{N(n,m-2)} \alpha_{m-2,j} Y_{m-2,j}(\omega) + \dots + \alpha_{0,1} Y_{0,1}(\omega) \end{aligned}$$

We also have, using the spherical harmonics decomposition of $g(\omega, p)$:

$$\mu_m g = \sum_{l=0}^{\infty} \sum_{k=1}^{N(n,l)} \mu_m g_{l,k} Y_{l,k}(\omega).$$

So then, using the fact that $\int_{S^{n-1}} Y_{l,k}(\omega)Y_{l',k'}(\omega) d\omega = 0$ for $l \neq l'$ and $k \neq k'$, if $l > m$, we see by integrating both sides of the previous equation against $Y_{l,k_0}(\omega)$ over S^{n-1} that

$$0 = \sum_{k=1}^{N(n,l)} \mu_m g_{l,k} \int_{S^{n-1}} Y_{l,k}(\omega)Y_{l,k_0}(\omega) d\omega$$

And then because $\{Y_{l,k}\}_{k=1}^{N(n,l)}$ is an orthonormal basis for H_l , we see that we get

$$0 = \mu_m g_{l,k_0}$$

for each $k_0 = 1, \dots, N(n, l)$. The proof that condition 2 holds is almost identical if m is odd.

Now all that's left to show is that for each l , $g_{l,k}(-p) = (-1)^l g_{l,k}(p)$ for each $k = 1, \dots, N(n, l)$. We know because $g = Rf$ for some $f \in \mathcal{S}(\mathbb{R}^n)$ that

$$g(-\omega, -p) = g(\omega, p).$$

We also know that

$$g(-\omega, -p) = \sum_{l=0}^{\infty} \sum_{k=1}^{N(n,l)} g_{l,k}(-p)Y_{l,k}(-\omega)$$

But $Y_{l,k}(-\omega) = (-1)^l Y_{l,k}(\omega)$, so by combining the previous two equations, we get

$$\sum_{l=0}^{\infty} \sum_{k=1}^{N(n,l)} g_{l,k}(-p)(-1)^l Y_{l,k}(\omega) = \sum_{l=0}^{\infty} \sum_{k=1}^{N(n,l)} g_{l,k}(p)Y_{l,k}(\omega).$$

Condition 1 then follows again by the orthogonality of the $Y_{l,k}(\omega)$ for different l and k . ■

4.3.1 Application: Non-uniqueness in the interior problem

The classical inversion formula for the Radon transform on \mathbb{R}^n involves the operator $(-\Delta)^{(n-1)/2}$, which is a local operator for n odd, but not in the case of n even. We'll look for the moment at $n = 2$. Because this operator is non local, a natural question arises: If we wish to construct an image of a specific region of interest inside

some object, is it enough to know $Rf(\omega, p)$ for only the hyperplanes (lines in this case) going through that region? This is known as the interior problem, or region of interest problem. When n is odd, the answer to this question is yes, because the inversion formula involves only local operators. In $n = 2$ however, we will be able to construct examples where this result proves false. We begin with the inversion formulas for R when f and g are given in terms of a spherical harmonics decomposition which are shown in (4.3) and (4.4).

Theorem 4.3.2 (Non-uniqueness for $n = 2$ in the interior problem) *Fix $a > 0$, and let $g_l \in \mathcal{S}(\mathbb{R})$ for each $l \in \mathbb{Z}$ be such that*

1. $g_l(-p) = (-1)^l g_l(p)$
2. $\mu_m g_l = 0$ for $0 \leq m < |l|$
3. $g_l(p) \equiv 0$ for $|p| \leq a$.

Then, letting

$$f_l(r) = -\frac{1}{\pi} \int_r^\infty (s^2 - r^2)^{-1/2} T_l\left(\frac{s}{r}\right) g'_l(s) ds$$

and $f(x) = \sum_{l=-\infty}^{\infty} f_l(|x|) e^{il \arg x}$, we have

$$Rf(\omega, p) \equiv 0$$

for $|p| \leq a$. In particular, there exists $f \in \mathcal{S}(\mathbb{R}^2)$ with $|f(x, y)| > 0$ for some (x, y) with $|(x, y)| < a$ such that $Rf(\omega, p) \equiv 0$ for $|p| < a$.

Proof Conditions 1 and 2 guarantee that there exists $f \in \mathcal{S}(\mathbb{R}^2)$ such that $Rf = g$ where $g(\omega, p) = \sum_{l=-\infty}^{\infty} g_l(p) e^{il\omega}$. Clearly by construction, $g(\omega, p) = 0$ for $|p| \leq a$. The formula for $f_l(r)$ is given by [22] and taking $f(x, y) = \sum_{l=-\infty}^{\infty} f_l(|(x, y)|) e^{il\theta}$ where $\theta = \arg(x + iy)$, we have $f \in \mathcal{S}(\mathbb{R}^2)$ and $Rf = g$. All that's left is to show that there exists a nontrivial $f \in \mathcal{S}(\mathbb{R}^2)$ such that $Rf(\omega, p) = 0$ for $|p| \leq a$. We know that

$g_0(p)$ is some even function in $\mathcal{S}(\mathbb{R})$ that is 0 in the region $|p| < a$. Then clearly $g(\omega, p) = g_0(p)$ satisfies the conditions in Theorem 4.3.1, so that $g_0 = Rf_0$ for

$$f_0(r) = -\frac{1}{\pi} \int_r^\infty (s^2 - r^2)^{-1/2} T_0\left(\frac{s}{r}\right) g_0'(s) ds.$$

Note that $T_0(x) \equiv 1$, so this becomes

$$f_0(r) = -\frac{1}{\pi} \int_r^\infty (s^2 - r^2)^{-1/2} g_0'(s) ds.$$

Now, for $0 \leq s < a$, we have $g_0'(s) \equiv 0$ by assumption, so for $0 \leq r < a$, we may write

$$f_0(r) = -\frac{1}{\pi} \int_a^\infty (s^2 - r^2)^{-1/2} g_0'(s) ds.$$

Integration by parts then yields for $0 \leq r < a$

$$f_0(r) = -\frac{1}{\pi} \int_a^\infty s(s^2 - r^2)^{-3/2} g_0(s) ds.$$

From this we see that if $g_0(p) \geq 0$ for all p , and $g_0(p) > 0$ for $a < p < R$ for some $R > a$, then $f_0(r) > 0$ for some $0 \leq r < a$. This shows that only having $Rf(\omega, p)$ for lines intersecting the region of interest $|p| < a$ is not sufficient to determine f uniquely in the region of interest. We show a more general example of non-uniqueness for $n = 2$ below in Figure 4.1. ■

In $n = 3$ dimensions, and in general in odd dimensions, the inverse Radon transform involves the operator $(-\Delta)^{(n-1)/2}$ which is local, and so we do not expect to have non-uniqueness in the interior problem for odd n . This is easy to see in for $l = 0$ in the $n = 3$ case. Suppose $g_0(p)$ satisfies the conditions of Theorem 4.3.1 for $n = 3$, and suppose $g_0(p) = 0$ for $|p| < a$. Then for $0 \leq r < a$,

$$\begin{aligned} f_0(r) &= c(3)r^{-1} \int_r^\infty g_0^{(2)}(s) ds \\ &= c(3)r^{-1} \int_a^\infty g_0^{(2)}(s) ds \\ &= -c(3)r^{-1} g_0'(a) = 0. \end{aligned}$$

For even dimensions though, we show a nontrivial example of non-uniqueness below.

Theorem 4.3.3 (Non-uniqueness for $n = 2m$) Fix $a > 0$, and let $g_{l,k} \in \mathcal{S}(\mathbb{R})$ for each $l \in \mathbb{Z}^+$ and $1 \leq k \leq N(n, l)$ be such that

1. $g_{l,k}(-p) = (-1)^l g_{l,k}(p)$
2. $\mu_m g_{l,k} = 0$ for $0 \leq m < l$ and each $1 \leq k \leq N(n, l)$
3. $g_{l,k}(p) \equiv 0$ for $|p| \leq a$ for each l and k .

Then, letting

$$f_{l,k}(r) = c(n)r^{2-n} \int_r^\infty (s^2 - r^2)^{(n-3)/2} C_l^{(n-2)/2} \left(\frac{s}{r} \right) g_{l,k}^{(n-1)}(s) ds$$

and $f(x) = \sum_{l=0}^\infty \sum_{k=1}^{N(n,l)} f_{l,k}(|x|) Y_{l,k}(x/|x|)$, we have

$$Rf(\omega, p) \equiv 0$$

for $|p| \leq a$. In particular for each $m = 2, 3, \dots$, there exists $f \in \mathcal{S}(\mathbb{R}^{2m})$ with $|f(x)| > 0$ for some x with $|x| < a$ such that $Rf(\omega, p) \equiv 0$ for $|p| < a$.

Proof That $g(\omega, p) = \sum_{l=0}^\infty \sum_{k=1}^{N(n,l)} g_{l,k}(p) Y_{l,k}(\omega)$ is in the range of the Radon transform is again clear by conditions 1 and 2 and Theorem 4.3.1. So there exists a unique $f \in \mathcal{S}(\mathbb{R}^n)$ such that $Rf = g$. Expanding $f(x)$ in a spherical harmonics expansion, we have

$$f(x) = \sum_{l=0}^\infty \sum_{k=1}^{N(n,l)} f_{l,k}(|x|) Y_{l,k}(x/|x|)$$

where the $f_{l,k}(r)$ are given by the formula in the theorem which is proved in [22]. By construction then, because each $g_{l,k}(p) = 0$ for $|p| \leq a$, it must be the case that $Rf(\omega, p) = 0$ for $|p| \leq a$.

To show that $f(x)$ could be non trivial in the region of interest in even dimensions, suppose $n = 2m$ for some integer $m \geq 2$. Then by direct calculation, we can show that

$$\frac{d^{n-1}}{ds^{n-1}} ((s^2 - r^2)^{(n-3)/2}) = (-1)^m \frac{(n-3)!!(n-1)!!r^{n-2}s}{(s^2 - r^2)^{(n+1)/2}},$$

where the double factorial $n!!$ is defined recursively by $n!! = n(n-2)!!$ with $0!! = 1!! = 1$. If we take $g_0(s) \in \mathcal{S}(\mathbb{R})$ such that $g_0(-s) = g_0(s)$ and $g_0(s) = 0$ for $|s| \leq a$, then for any $\delta > 0$, we have for $0 \leq r \leq a - \delta$

$$\begin{aligned} f_0(r) &= c(n)r^{2-n} \int_r^\infty (s^2 - r^2)^{(n-3)/2} g_0^{(n-1)}(s) ds \\ &= c(n)r^{2-n} \int_a^\infty (s^2 - r^2)^{(n-3)/2} g_0^{(n-1)}(s) ds \\ &= (-1)^{n+m-1} c(n)(n-3)!!(n-1)!! \int_a^\infty \frac{s}{(s^2 - r^2)^{(n+1)/2}} g_0(s) ds \end{aligned}$$

where the last line follows by repeated integration by parts along with the fact that $g_0^{(\beta)}(a) = 0$ for any β a non-negative integer, and $\lim_{s \rightarrow \infty} s^\alpha g_0^{(\beta)}(s) = 0$ for any α and β that are non-negative integers. It is then clear, because $s/(s^2 - r^2)^{(n+1)/2} > 0$ for $s > a$, that if we take $g_0 \geq 0$ and $g_0(s) > 0$ for some $s > a$, then $f_0(r) \neq 0$ for $0 \leq r < a - \delta$. This shows an example of non-uniqueness for the interior problem in every \mathbb{R}^n for n even.

To show general non-uniqueness, we may take any $g_{l,k}(p)$ satisfying the conditions of Theorem 4.3.1 with $g_{l,k}(p) = 0$ for $|p| < a$ for some $a > 0$ and $|g_{l,k}(p)| > 0$ for some $p > a$. Then using the formulas above for $f_{l,k}$ and $g_{l,k}$, we can show in a similar manner as we did for f_0 that $f_{l,k}(r) \neq 0$ for some $r < a$. ■

Because the Radon transform is a linear operator, we may also construct additional examples of non-uniqueness by taking linear combinations of previously constructed functions that given non-uniqueness.

A note about Figure 4.1

We make a note about how Figure 4.1 is constructed. To construct the $g(\omega, p)$ shown, we start by taking $\phi \in C_0^\infty((-1, 1))$ such that $\phi(p) = 0$ for $|p| < 0.3$ and

$\phi(p) = \phi(-p)$. We also take $\phi \geq 0$ on its support, and $\phi(s) \approx 1$ for $0.4 < |s| < 0.6$.

From there we take

$$g(\omega, p) = \sum_{l=0}^{10} g_l(p) \cos(l\omega),$$

where we have

$$g_l(p) = \operatorname{sgn}(p^l) \phi(p) \left(\cos(l\pi p) + \sum_{k=0}^{l-1} b_k \cos(k\pi p) \right).$$

We solve for the the b_k so that we are guaranteed to have $\mu_m g_l(p) = 0$ for $0 \leq m < l$ as is required by Theorem 4.3.1. Note that the linear system of equations that are obtained from the moment conditions

$$\begin{aligned} (\mu_0 g_l)(b_1, \dots, b_l) &= 0 \\ (\mu_1 g_l)(b_1, \dots, b_l) &= 0 \\ &\vdots \\ (\mu_{l-1} g_l)(b_1, \dots, b_l) &= 0 \end{aligned}$$

is under determined, because $\mu_m g_l = 0$ automatically if $m + l$ is odd, so we have some freedom in choosing the b_k . We note also that the factor of $\operatorname{sgn}(p^l)$ does not effect the differentiability of g_l , as $g_l(p) = 0$ near $p = 0$, but does ensure that $g_l(-p) = (-1)^l g_l(p)$ as is required. The top right image in Figure 4.1 was constructed by taking $R^{-1}(g(\omega, p))$. We accomplish this by using the `iradon` function from the `skimage` module in Python. The bottom left image is simply the top right image multiplied by a smooth cutoff to show that it is indeed the case that $R^{-1}(g(\omega, p)) \neq 0$ inside the region of interest $0 \leq r < 0.3$.

4.4 Conclusion and future work

We showed a more practical characterization of the Radon transform as an operator $R : \mathcal{S}(\mathbb{R}^n) \rightarrow \mathcal{S}_H(\mathbb{P}^n)$ which can be used to construct elements of the kernel of the restricted Radon transform

$$\begin{aligned} R|_{|p|<a} : \mathcal{S}(\mathbb{R}^n) &\rightarrow \mathcal{S}_H(\mathbb{P}^n) \\ f &\mapsto Rf(\omega, p)|_{|p|<a} . \end{aligned}$$

This is achieved by using classical integral formulas for f and Rf in terms of spherical harmonics, in which case the Radon transform is a diagonal operator. These formulas take the form in \mathbb{R}^n :

$$\begin{aligned} g_{l,k}(p) &= |S^{n-2}| \int_p^\infty C_l^{(n-2)/2} \left(\frac{p}{r} \right) \left(1 - \frac{p^2}{r^2} \right)^{(n-3)/2} f_{l,k}(r) r^{n-2} dr, \\ f_{l,k}(r) &= c(n) r^{2-n} \int_r^\infty (s^2 - r^2)^{(n-3)/2} C_l^{(n-2)/2} \left(\frac{s}{r} \right) g_{l,k}^{(n-1)}(s) ds, \end{aligned}$$

where $c(n)$ and $C_l^{(n-2)/2}(x)$ are defined as above, and the $g_{l,k}$ and $f_{l,k}$ are the coefficients in the spherical harmonics expansions of g and f respectively. For future work, we would like to use these integral formulas alone to show a similar result to Theorem 4.3.1. It's possible using the Funk-Hecke theorem to show that applying the formula for $f_{l,k}(r)$ to the $g_{l,k}(p)$ shown above does indeed give back $f_{l,k}(r)$. We hope in the future to use the conditions in the hypothesis of Theorem 4.3.1 to show that $f_{l,k}(r)$ given above has some regularity properties, which will give a result with weaker assumptions on $g(\omega, p)$. Experimentally, this seems to be the case.

Example of non-uniqueness for R on \mathbb{R}^2

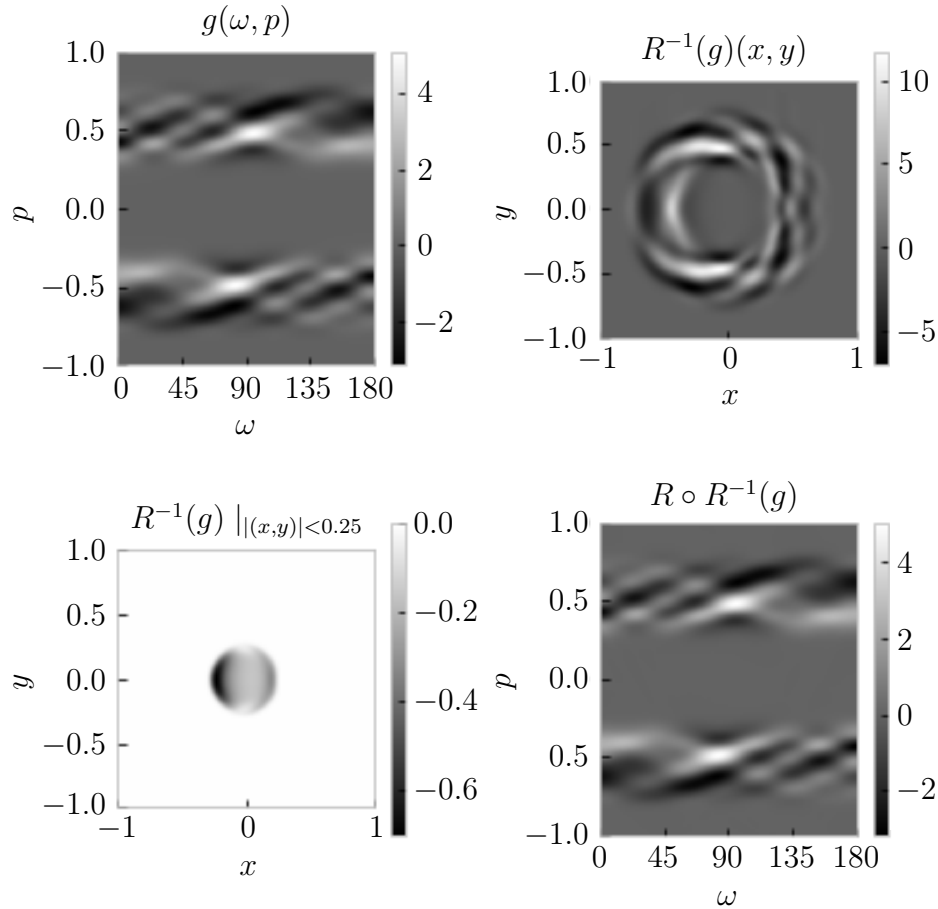


Figure 4.1. (Top left) Function $g(\omega, p) = \sum_{l=0}^{10} a_l g_l(p) e^{il\omega}$ constructed so that $g = Rf$ for some $f \in \mathcal{S}(\mathbb{R}^2)$. This function was constructed so that $\mu_m g_k = 0$ for $0 \leq m < k$ in the Fourier series expansion of g , as is required by Theorem 4.3.1. (Top right) Inverse Radon transform of g . (Bottom left) $R^{-1}(g)$ for $|(x, y)| < 0.3$. Note that $R^{-1}(g)(x, y)$ is not identically 0 here. (Bottom right) $R \circ R^{-1}(g)$, which we can see is the same as in the top left.

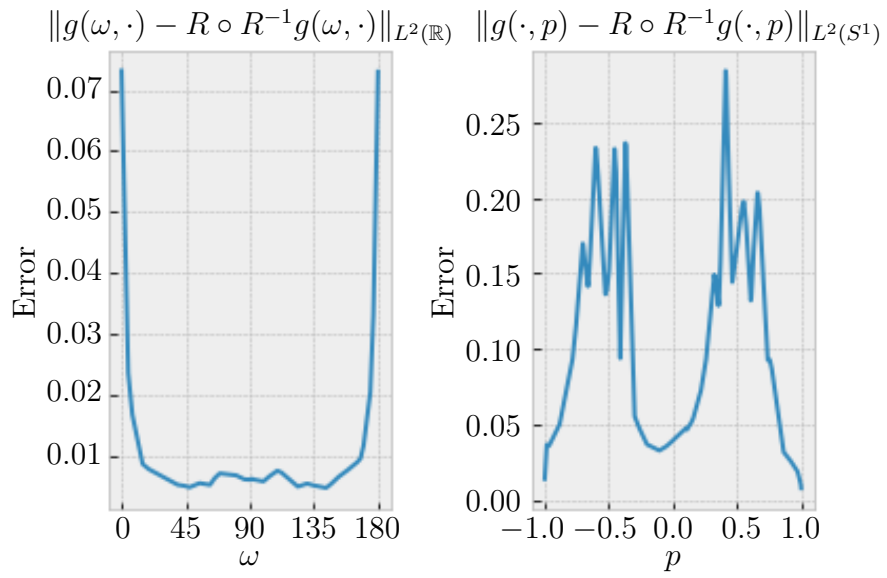


Figure 4.2. Error in $R \circ R^{-1}g$ for the function shown in Figure 4.1

Examples of non-uniqueness for R in ROI problem on \mathbb{R}^2

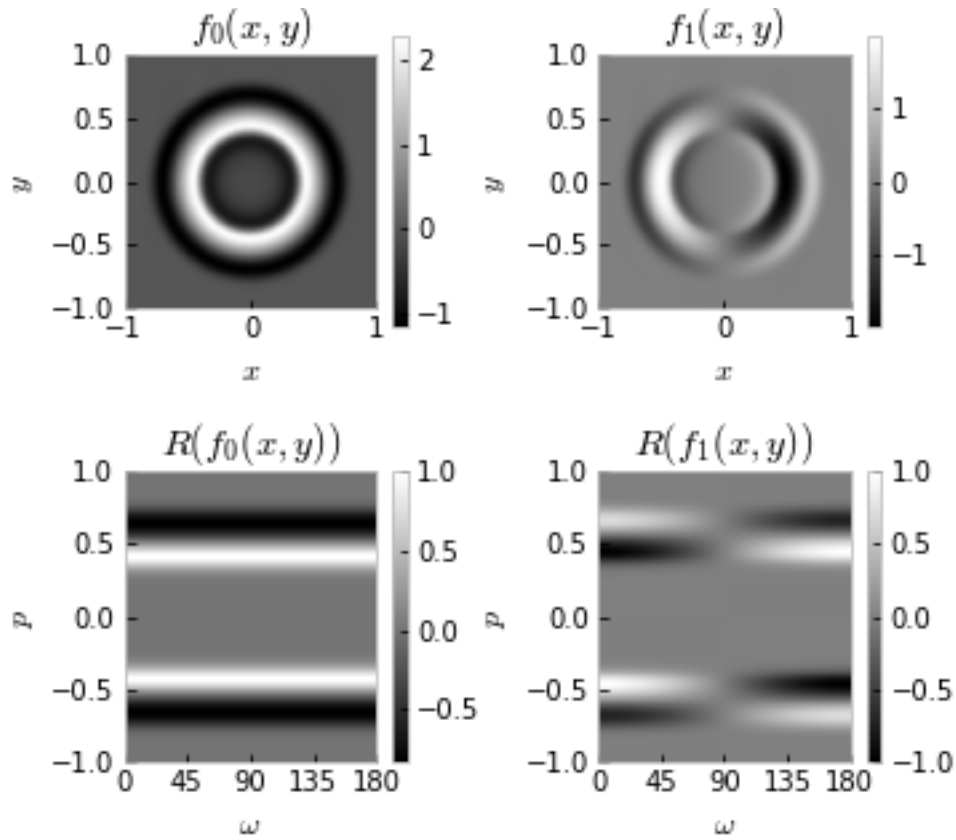


Figure 4.3. Simple examples of non-uniqueness for the region of interest problem. Both f_0 and f_1 are nonzero in the region of interest $|(x, y)| < 0.3$, but Rf_0 and Rf_1 are zero for $|p| < 0.3$.

REFERENCES

- [1] Sören Bartels. *Numerical Approximation of Partial Differential Equations*, volume 64 of *Texts in Applied Mathematics*. Springer International Publishing, Switzerland, 2016.
- [2] A. M. Cormack. Representation of a function by its line integrals, with some radiological applications. *Journal of Applied Physics*, 34(9):2722–2727, 1963.
- [3] A. M. Cormack. Representation of a function by its line integrals, with some radiological applications. ii. *Journal of Applied Physics*, 35(10):2908–2913, 1964.
- [4] R. Courant, K. Friedrichs, and H. Lewy. On the partial difference equations of mathematical physics. *IBM J. Res. Develop.*, 11:215–234, 1967.
- [5] Stanley R. Deans. *The Radon transform and some of its applications*. John Wiley & Sons, New York, NY, 1983.
- [6] *NIST Digital Library of Mathematical Functions*. <http://dlmf.nist.gov/>, Release 1.0.27 of 2020-06-15. F. W. J. Olver, A. B. Olde Daalhuis, D. W. Lozier, B. I. Schneider, R. F. Boisvert, C. W. Clark, B. R. Miller, B. V. Saunders, H. S. Cohl, and M. A. McClain, eds.
- [7] Alain Grigis and Johannes Sjöstrand. *Microlocal Analysis for Differential Operators: An Introduction*. London Mathematical Society Lecture Note Series. Cambridge University Press, 1994.
- [8] Marcus J Grote and Imbo Sim. Efficient pml for the wave equation. *arXiv preprint arXiv:1001.0319*, 2010.
- [9] Victor Guillemin and Shlomo Sternberg. *Semi-classical analysis*. International Press, Boston, MA, 2013.
- [10] Markus Haltmeier. Thermoacoustic computed tomography with large planar receivers. *Inverse Problems*, 20(5):1663–1673, 2004.
- [11] Markus Haltmeier. Sampling conditions for the circular radon transform. *IEEE Transactions on Image Processing*, 25(6):2910–2919, 2016.
- [12] Sigurdur Helgason. *Groups and geometric analysis*. Academic Press, Inc, Orlando, FL, 1984.
- [13] Lars Hörmander. Fourier integral operators. i. *Acta Math.*, 127:79–183, 1971.
- [14] Lars Hörmander. *The analysis of linear partial differential operators IV: Fourier integral operators*. Springer, 2009.
- [15] Fritz John. *Partial differential equations*, volume 1 of *Applied Mathematical Sciences*. Springer-Verlag New York, 1 edition, 1971.

- [16] Hubert Kalf. On the expansion of a function in terms of spherical harmonics in arbitrary dimensions. *Bull. Belg. Math. Soc. Simon Stevin*, 2(4):361–380, 1995.
- [17] Robert A. Kruger, William L. Kiser, Daniel R. Reinecke, and Gabe A. Kruger. Thermoacoustic computed tomography using a conventional linear transducer array. *Medical Physics*, 30(5):856–860, 2003.
- [18] Peter Kuchment and Leonid Kunyansky. Mathematics of thermoacoustic tomography. *European Journal of Applied Mathematics*, 19(2):191–224, 2008.
- [19] Robert J. Marks, II. *Introduction to Shannon sampling and interpolation theory*. Springer Texts in Electrical Engineering. Springer-Verlag, New York, 1991.
- [20] André Martinez. *An introduction to semiclassical and microlocal analysis*. Universitext. Springer, New York, 2002.
- [21] C. Mathison. Thermoacoustic tomography with circular integrating detectors and variable wave speed. *Inverse Problems & Imaging*, 14(1930-8337_2020_4_665):665, 2020.
- [22] Frank Natterer. *The mathematics of computerized tomography*, volume 32 of *Classics in Applied Mathematics*. Society for Industrial and Applied Mathematics (SIAM), Philadelphia, PA, 2001. Reprint of the 1986 original.
- [23] Alexander A Oraevsky, Steven L Jacques, Rinat O Esenaliev, and Frank K Tittel. Laser-based optoacoustic imaging in biological tissues. In *Laser-Tissue Interaction V; and Ultraviolet Radiation Hazards*, volume 2134, pages 122–129. International Society for Optics and Photonics, 1994.
- [24] Daniel P Petersen and David Middleton. Sampling and reconstruction of wave-number-limited functions in n-dimensional euclidean spaces. *Information and Control*, 5:279–323, 1962.
- [25] Eric Quinto. Radon transforms on curves in the plane. *Tomography, impedance imaging, and integral geometry : 1993 AMS-SIAM Summer Seminar on the Mathematics of Tomography, Impedance Imaging, and Integral Geometry, June 7-18, 1993, Mount Holyoke College, Massachusetts*, 1994.
- [26] Johann Radon. On the determination of functions from their integral values along certain manifolds (translation). *IEEE Transactions on Medical Imaging*, 5(4):170–176, 1986.
- [27] Plamen Stefanov. Semiclassical sampling and discretization of certain linear inverse problems, 2018.
- [28] Plamen Stefanov and Gunther Uhlmann. Thermoacoustic tomography with variable sound speed. *Inverse Problems*, 25(7), 2009.
- [29] Plamen Stefanov and Yang Yang. Thermo- and photoacoustic tomography with variable speed and planar detectors. *SIAM Journal on Mathematical Analysis*, 49(1):297–310, 2017.
- [30] Elias Stein and Guido Weiss. *Introduction to Fourier analysis on Euclidean spaces*. Princeton University Press, Princeton, NJ, 1971.

- [31] Gilbert Strang. The wave equation and staggered leapfrog, 2006.
- [32] Michael E. Taylor. *Geometrical optics and Fourier integral operators*, pages 146–191. Princeton University Press, 1981.
- [33] Michael E Taylor. *Partial differential equations I basic theory*. Applied Mathematical Sciences, 115. Springer, 2nd ed. edition, 2011.
- [34] François Trèves. *Introduction to pseudodifferential and Fourier integral operators*, volume 2 of *The University Series in Mathematics*. Plenum Press, 1980.
- [35] Minghua Xu and Lihong V. Wang. Photoacoustic imaging in biomedicine. *Review of Scientific Instruments*, 77(4), 2006.
- [36] Gerhard Zangerl, Otmar Scherzer, and Markus Haltmeier. Circular integrating detectors in photo and thermoacoustic tomography. *Inverse Problems in Science and Engineering*, 17(1):133–142, 2009.
- [37] Gerhard Zangerl, Otmar Scherzer, Markus Haltmeier, et al. Exact series reconstruction in photoacoustic tomography with circular integrating detectors. *Communications in Mathematical Sciences*, 7(3):665–678, 2009.
- [38] Maciej Zworski. *Semiclassical Analysis*, volume 138 of *Graduate studies in mathematics*. American Mathematical Society, Providence, R.I., 2012.

VITA

Chase Mathison was born in Anderson, IN on November 12, 1990. He attended Rose-Hulman Institute of Technology in Terre Haute, IN for his undergraduate education where he received a B.S. in Mathematics with a concentration in Statistics and Operations Research in May 2013, along with a minor in Computational Science. Upon completion of his Ph.D. in Mathematics from Purdue University in August of 2020, he will start as an Assistant Professor of Mathematics in the College of Arts and Sciences at Shenandoah University in Winchester, VA.